Montanuniversität Leoben – University of Leoben
Department Metallurgie – Department of Metallurgy
Nichteisenmetallurgie – Nonferrous Metallurgy

Master thesis

Subject:

Influence of raw materials and manufacturing methods on the microstructure of cemented carbides

Submitted by:
MMag. BSc. Karin Ratschbacher

Supervised by:
Dipl.-Ing. Dr.mont. Stefan Luidold

Leoben, December 2012

This thesis was typeset by the use of KOMA-Script and LaTeX 2$_\varepsilon$.

NICHTEISENMETALLURGIE
MONTANUNIVERSITÄT
A-8700 LEOBEN

Karin Ratschbacher

Dezember 2012

Influence of raw materials and manufacturing methods on the microstructure of cemented carbides

Cemented carbides have a wide variety of application fields. Seemingly almost as extensive is the number of manufacturing methods, sometimes used simultaneously for the same products for the sole reason of production logistics. The goal of this diploma thesis is to systematically investigate the effect on the microstructure of the individual production routes, especially the varying pressure treatments on two submicron powders with different cobalt contents. The powders are moulded by three individual moulding processes, also having an effect on the resulting microstructure.

In order to determine which material, moulding process and temperature-pressure treatment combination leads to the best product quality. Samples will be evaluated particularly with regard to the resulting porosity. Porosity has a significant effect on the mechanical properties of cemented carbide products.

The evaluation of the resulting porosity is currently done metallographically. Finding an alternative way to determine the porosity could enable automatic investigation and the generation of objective data. The porosity is to be investigated by:

I. Metallographic investigation
II. Automatic investigation: The software of an optical microscope is to be set up in order to enable an automatic investigation of porosity, based on different shades of grey of the surface of the sample.
III. SEM-EDX: Inclusions and pores could be determined by identifying different elements.
IV. BET: The determination of the specific surface of a sample could be an indicator for the porosity of the sample
V. CT: The investigation method generated a 3D-model of a sample. Pores should be visible within the generated model.

Leoben, December 2012

Dedicated to the human aspect in my intellectual endeavours.

Es gibt, so hat er einmal gesagt,
kein adeliges und erhöhtes Leben
ohne das Wissen um die Teufel und Dämonen
und ohne den beständigen Kampf gegen sie.

[Hermann Hesse, das Glasperlenspiel]

Affidavit

I declare in lieu of oath, that I wrote this thesis and performed the associated research myself, using only literature cited in this volume.

Karin Ratschbacher
Leoben, December 2012

Acknowledgements

I would like to thank Prof. Antrekowitsch Helmut and Dr. Luidold Stefan for encouraging me to believe in the scientific process and giving me the freedom to experience it.
At Ceratizit Austria I would like to thank Dr. Barbist Roland for initiating this thesis and providing scientific support. Mister Pöll Peter and Mister Glätzle Johannes deserve acknowledgement for taking the time to discuss experimental approaches and interpretation of result, whenever needed. Misses Nagele Anja and Miss Malzner Johanna took me in and taught me metallography as far as I needed it to complete this project - many thanks for that!

On a personal note I would like to thank Philipp Stögner for moral and hands on support and Michael Henzinger for going through it all with me - always.

Abstract

The subjects of investigation were two submicron powders with grain sizes of 0.75 μm and 0.6 μm and a cobalt contents of 10 % and 8.2 % respectively. The powders were compacted using direct, dry-bag and extrusion moulding. Samples were drawn after presintering the materials to represent the raw moulded material, after sintering, after sinter HIP and after treating the sintered samples with HIP. In order to determine which material, moulding process and temperature-pressure treatment combination would lead to the best result, all samples were metallographically investigated, especially evaluating the resulting porosity.

The presintered state showed a clear advantage in microstructure for the samples, made from powder with smaller grainsize and less cobalt content. These samples also show a higher porosity after sintering, manufactured by extrusion and dry-bag moulding. The reason for this is the smaller grainsize of the material, which equals a higher specific surface and narrower grainsize distribution, which results in the grains not packing well together and more small pores between the grains. Due to this, more rearrangement of the material structure and more shrinkage during the sintering process is necessary, in order to fill the voids. This can lead to a higher porosity especially if the structure rearranges itself aiming to reduce the specific surface. Extrusion moulded samples of either material show higher porosity than the the samples of other manufacturing methods. Surprising is the higher amount of B-pores in extrusion moulded HIP samples than sinter HIP samples, even though HIP operates with a much higher pressure.

Dry-bag moulding seems to be the best manufacturing method for both materials, closely followed by direct moulding. Sinter HIP doesn't seem to cause any kind of disadvantage concerning the porosity in either of the tested materials, despite the lower pressure, compared to HIP.

Concerning the automatic investigation of porosity via optical light microscope it is likely that the process of detecting pores is too prone to falsification due to dirt, alcohol staines, dust, etc. and also too complex to be reduced to different shades of grey.

Kurzfassung

Im Rahmen der Arbeit erfolgte die Untersuchung von zwei extrafeinen Hartmetallpulver der Korngrößen 0,75 μm und 0,6 μm mit Kobaltgehalten von jeweils 10 % und 8,2 %. Die Pulver wurden stranggepresst oder mittels "Dry-bag"-, beziehungsweise Direktpressverfahren verdichtet. Proben aus vorgesintertem Material bilden den Zustand des Grünlings ab, während gesintertes einen Übergangs- zustand zum fertigen Produkt, welches noch nachverdichtet wird oder direkt die Sinter-HIP-Route durchläuft. Ziel der vorliegenden Arbeit war es die optimale Kombination aus Material, Pressverfahren und Nachbehandlung hinsichtlich Porosität zur finden. Dazu wurden die gezogenen Proben metallographisch untersucht und ausgewertet.

Das Pulver mit der kleineren Korngröße und dem geringeren Kobaltgehalt zeigte im vorgesinterten Zustand eine vorteilhaftere Mikrostruktur. Wird dieses Material jedoch strang- oder "dry-bag"-gepresst und dann gesintert, so weist es eine höhere Porosität, verglichen mit anderen Material-Pressverfahrenskombinationen, auf. Dies lässt sich durch die kleinere Korngröße des Pulvers erklären, welche mit höherer spezifischen Oberfläche und einer kleineren Korngrößenverteilung einher geht, was zu einer schlechteren Packungsdichte und Hohlräumen zwischen den Partikeln führt. Diese Hohlräume müssen während des Sintervorganges durch Volumensschwund und Umordnung der Struktur geschlossen werden. Dabei können, vor allem wenn Umordnungen zur Verringerung der spezifischen Oberfläche erfolgen, Poren entstehen. Stranggepresste Proben beider Materialen weisen höhere Porositäten als jene auf, die "dry-bag-" oder direkt gepresst wurden. Überraschend ist die höhere Porosität stranggepresster Materialien, welche nachverdichtet wurden, verglichen mit Proben, die Sinter-HIP-Behandlung erfuhren, da beim Nachverdichten mit viel höheren Drücken gearbeitet wird.

Dry-bag-Pressen liefert die besten Ergebnisse bezüglich Porosität bei beiden Materialien, dicht gefolgt vom Direktpressverfahren. Sinter-HIP liefert trotz der erheblich geringeren Drücke, verglichen mit dem Nachverdichten, gleichwertige Ergebnisse hinsichtlich Porosität.

Die automatische Porositätsauswertung mittels softwaregesteuertem Lichtmikroskop stellte sich als sehr fehleranfällig bezüglich Verschmutzungen auf der Probenoberfläche heraus.

Contents

1 Introduction

Cemented carbides have a wide variety of application fields. Seemingly almost as extensive is the number of manufacturing methods, sometimes used simultaneously for the same products for the sole reason of production logistics.
The goal of this diploma thesis was to systematically investigate the effect on the microstructure of the individual production routes, especially the varying pressure treatments on two submicron powders with different cobalt contents. The powders were moulded by three individual moulding processes, also having an effect on the resulting microstructure.
From an economical point of view, this thesis was also initiated due to the varying costs of the different pressure treatments.

To facilitate and enhance the accuracy of the evaluation of microstructure, more specifically the porosity of the products in future quality control, an automatic optical investigation of the porosity is to be implemented. The latter is motivated by the possibility of generating a greater amount of more accurate and comparable data, which can be processed digitally.

The chapter on the theory of cemented carbides gives an introduction to the materials used and the different moulding processes, available and relevant to this thesis. Furthermore, the sintering process and the subsequent or combined pressure treatments are introduced. The chapter closes with a presentation of literature, dealing with the effect on the microstructure, of the introduced manufacturing processes and how cemented carbides are characterized.

In order to assure reproducibility, the experimental setup and the obtained results are presented in chapter 3.

Due to the great number of still unknown reasons for observed effects in the microstructure of investigated samples, the discussion not only refers to literature, but also describes knowledge and experiences of production personnel in order to give a possible starting point for further research on the topic.

2 Theory of cemented carbides

This chapter will give an introduction to various aspects of cemented carbides, relevant to the subject of this thesis. It discusses the required raw materials, as well as the properties of such materials and their production methods. Finally some information on their microstructure is given.

2.1 Raw material

Cemented carbides consist most commonly of tungsten carbide due to it's high wear resistance and a cobalt binder to provide ductility. Table 2.1 displays a selection of material properties for these materials.

Properties	**WC**	**Co**
Crystalline structure	hex.	hex.
Density [kg/m^3]	15700	8900
Hardness [N/mm^2]	2080	
Young's modulus [kN/mm^2]	696	209
Melting point [°C]	2600	1495
Coefficient of thermal expansion [10^{-6}/K]	5.2	13
Electric resistance [Ωm]	$2.2{\cdot}10^{-4}$	$6{\cdot}10^{-8}$

Table 2.1: Properties of tungsten carbide (WC) and cobalt (Co) [1]

The grain size of the WC grains can be classified according to figure 2.1.

2.2 Properties of cemented carbide

In line with quality inspection and research the following parameters are often used to predict material behaviour: [3–5]

- **Density:** Typical value for WC and cobalt composites is around 15,4 g/cm^3.
- **Hardness:** Hardness values are typically measured by making indentations with diamond pins of various shapes. Vickers hardness (HV) is measured with a square-based pyramid, pressed onto the cemented carbide with a defined load. Typical values for hardmetals range from HV 800 to 2400. The hardness of the cemented carbide varies greatly with the Co-content. Higher hardness values relate to lower Co-contents and finer grain sizes.
- **Young's modulus:** The stress per unit of strain is almost linear until fracture for most hardmetals. Typical values range from 400 to 700 MPa.

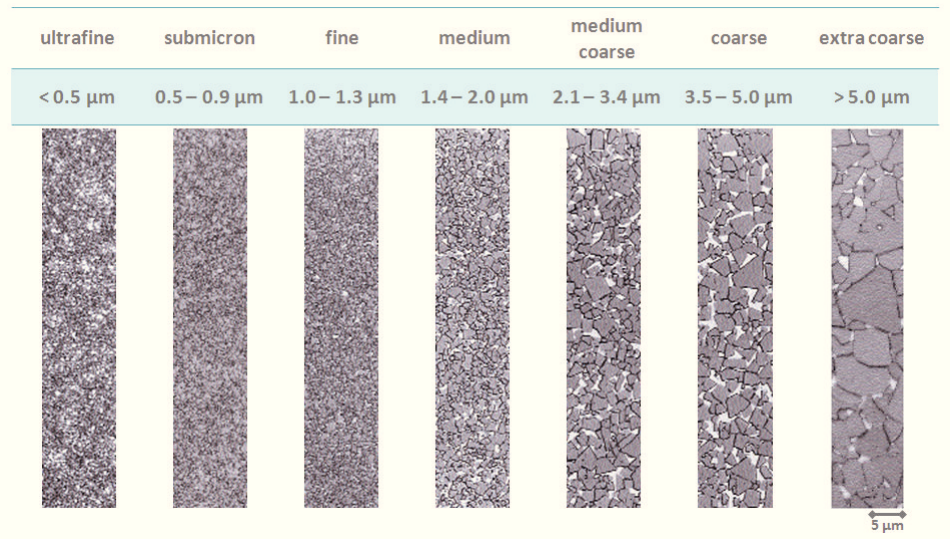

Figure 2.1: Categorization of WC grain size [2]

- **Thermal expansion coefficient:** It measures the mean expansion per unit of length, expressed as an average per kelvin over a defined temperature interval. Typical values range from 4,5 to 8,5 $\cdot$ 10^{-6}/K between 0 and 800 °C.
- **Magnetisation coercive field strength:** In order to completely demagnetise a magnetically saturated sample, a certain coercive field is necessary. Typical values range from 6 to 28 kA/m. High values indicate fine grain size and minimal binder content. The coercive field strength is also influenced by degree of alloying, inclusions, porosity, internal stress and the presence of an eta-phase (Co_3W_3C) that is known to raise the coercive field strength. A carbon deficiency during the sintering process or under-sintering results in a very high value for the coercive field strength due to the finer microstructure, which is higher in internal stress. Over-sintering results in coarser microstructure and low values for the coercive field strength.
- **Magnetic saturation ($4\pi\sigma$):** In order to estimate the amount of binder phase, the degree to which the material is sintered and the carbon balance of the atmosphere, which the material was sintered in, the magnetic fraction of the binder phase is determined. Components (W, C, Ti, etc.), which are dissolved within the binder phase and the presents of an η-phase (Co_3W_3C) lower the $4\pi\sigma$ value. Sintering with a carbon deficiency (for example material with low carbon content) also results in low $4\pi\sigma$ values. A high $4\pi\sigma$ value can indicate the presents of free carbon in the material. High $4\pi\sigma$ values result in low values for the coercive field strength and vice versa.

All of the properties described above show a dependency on cobalt content, as illustrated in figure 2.2. [3, 6]

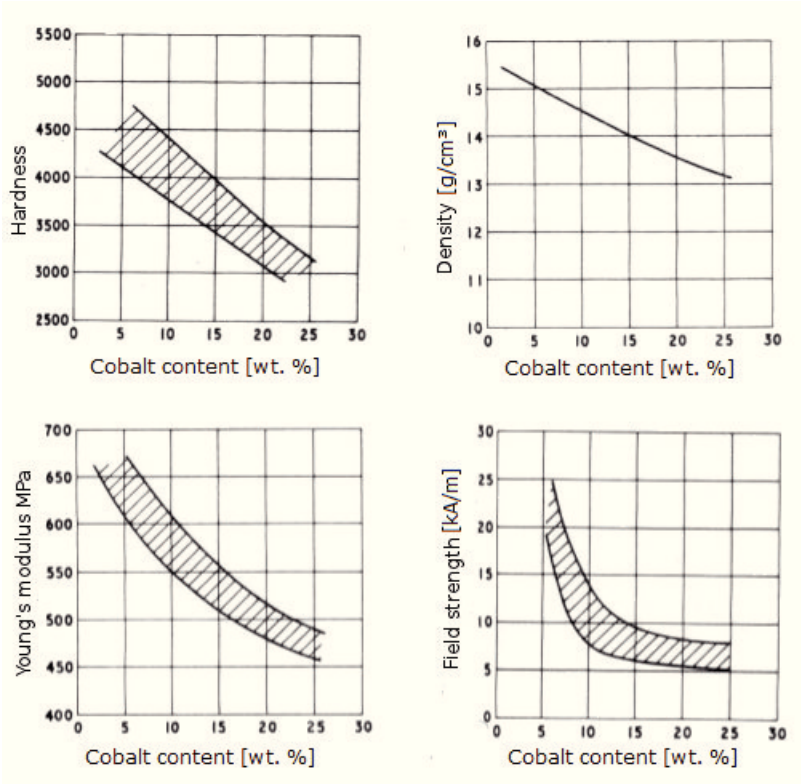

Figure 2.2: Influence of cobalt content on density, hardness, elastic modulus and coercive field strength [3]

2.3 Manufacturing methods

The manufacturing process is summarized in figure 2.3. Tungsten oxide is reduced, using H_2 as a reducing agent and then carburized. The tungsten carbide is thereafter mixed with the binder phase (Co).

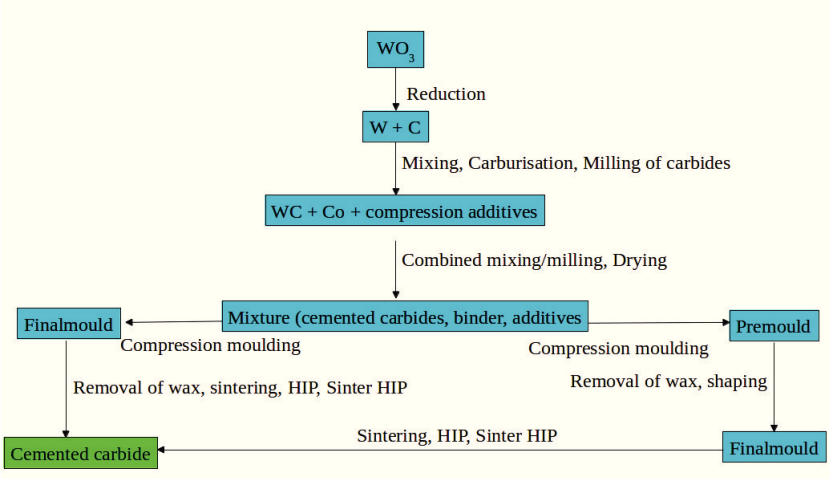

Figure 2.3: Manufacturing process of cemented carbides [7]

2.3.1 Compression moulding and extrusion moulding

The compression moulding process operates with pressures around 100-300 MPa. The compression of the powder is limited to the spacial direction of the heading tool, with no hydrostatical flow being involved. Due to the friction of the powder against the wall of the mould, the pressure and consequently the density decrease with increasing distance from the heading tool (figure 2.4). It is also possible to simulate the density distribution within the moulded product, as displayed in figure 2.5. After the pressing itself, the plunger(s) is/are removed and the material reverses the elastic deformation. If the applied pressure was too high, the relaxation process can cause damage in the product as displayed in figure 2.6. Dry-bag and direct moulding machines are displayed in figure 2.7 and figure 2.8 respectively. [1, 8]

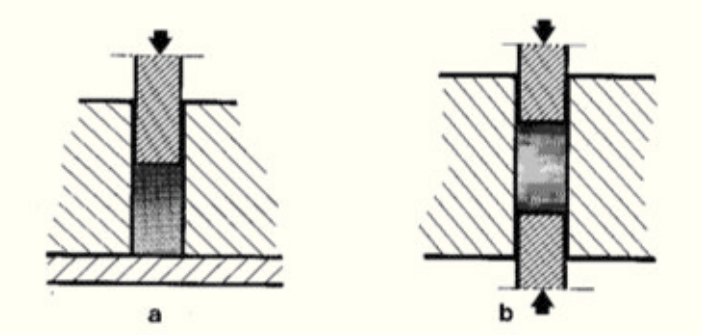

Figure 2.4: Distribution of density in a sample [1]

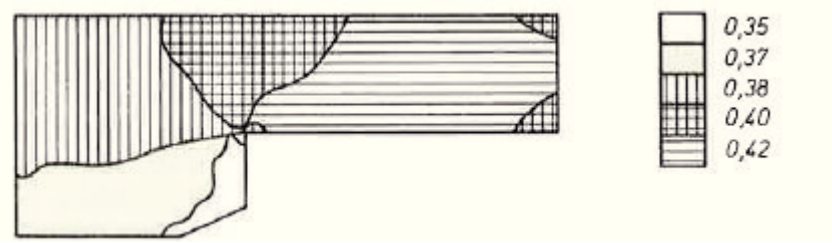

Figure 2.5: Simulation of density distribution $[g/cm^3]$ in a moulded product [8]

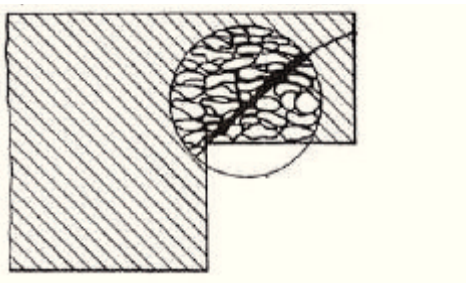

Figure 2.6: Crack due to too high moulding pressure [8]

Zones of smaller density shrink more extensively during sintering, which leads to irregular shapes. Newer compression machines use moulds, that compensate the higher shrinking of less dense zones by having pressure adjustable heading tools. The

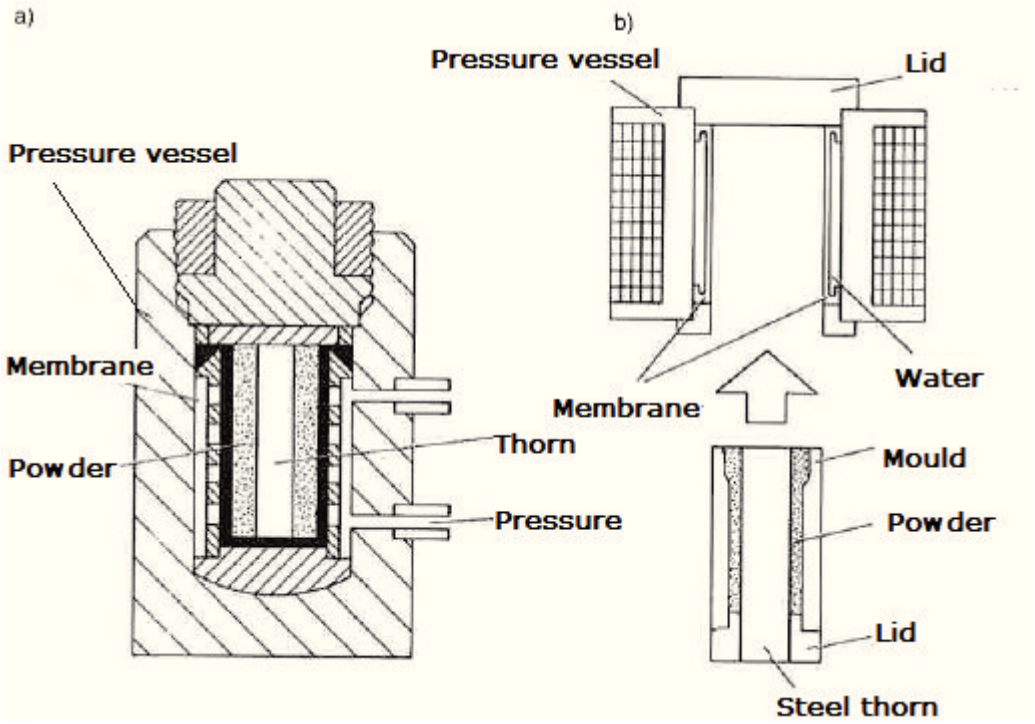

Figure 2.7: Dry-bag moulding machine [8]

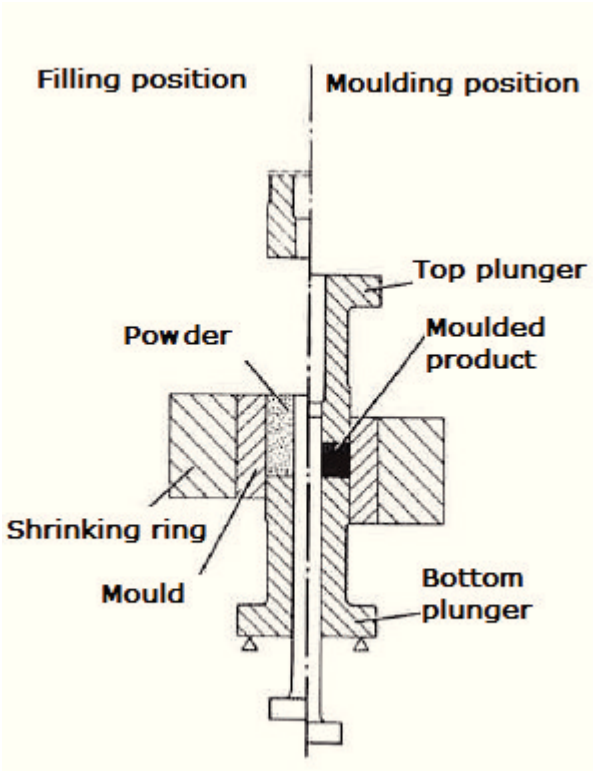

Figure 2.8: Direct moulding machine [8]

volume of the powder mix is reduced by 60-65 % during the compression moulding. During the sintering process, the sample shrinks another 15-20 % in each direction, which equals a 40-50 % loss of volume, that goes into porosity and the loss of compression moulding additives. [1]

In order to manufacture very long, round or profiled parts, the technology of extrusion moulding is used. Figure 2.9 displays two different extrusion moulding machines. Paraffin and petroleum jelly are added to the powder mixture, to enhance plastification. The mixed components are extruded through a cone with an optional core in the middle in order to extrude pipes. Due to the friction against the wall of the mould, areas close to the surface are more dense than areas closer to the center. [1]
Plastifier is used to reduce the pressure, necessary to extrude the material. It en-

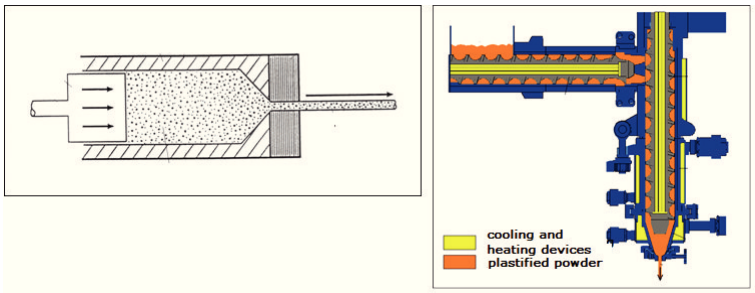

Figure 2.9: Extrusion moulding through two different processes [9]

hances the relative movement of the particles and reduces the friction between mass and mould. After extrusion, the pieces are dewaxed to eliminate the plastifier. As a result of the drying process, the extrudant becomes more rigid and also shrinkage occurs until the particles touch and an array of pores is formed between the particles. [1]

If solids are added to a plastifier a higher shear stress is required in order to maintain a set shear rate. Further addition of solids result in an absence of strain in the material, while a small pressure is applied. The pressure necessary to initiate strain in the material is referred to as initial bulk stress. It increases with the amount of solids added to the plastifier. If the plastifier to solid ratio becomes too small, the amount of voids increases and it ultimately becomes too hard to extrude the resulting wet powder. A lack or deficiency of solids in the plastifier leads to an extrudant, that is too soft to retain its shape. Consequently there is only a narrow range of plastifier content with which extrusion is possible. [1]

The amount of plastifier used in the mix is strongly dependent on the particle size distribution within the powder, which affects extrusion in two ways. A proper particle size distribution can allow the powder to pack tightly, which reduces the amount of plastifier necessary to fill the spaces, that consequently leads to a denser product. The higher the amount of plastifier, exceeding the amount necessary in order to fill the voids between the grains, the easier the material is to extrude. Figures 2.10, 2.11 and 2.12 show the decrease of the parameters initial bulk stress and initial wall stress due to an increase of space between the particles. The amount

of plastifier needed is greatest for distribution A. The narrow grain size distribution prevents the particles from packing well and a relatively large amount of plastifier is needed in order to fill the spaces. Also the small grains have a high specific surface, which causes plastifier consumption. Smaller amounts of plastifier lead to less drying time and denser products. [10]

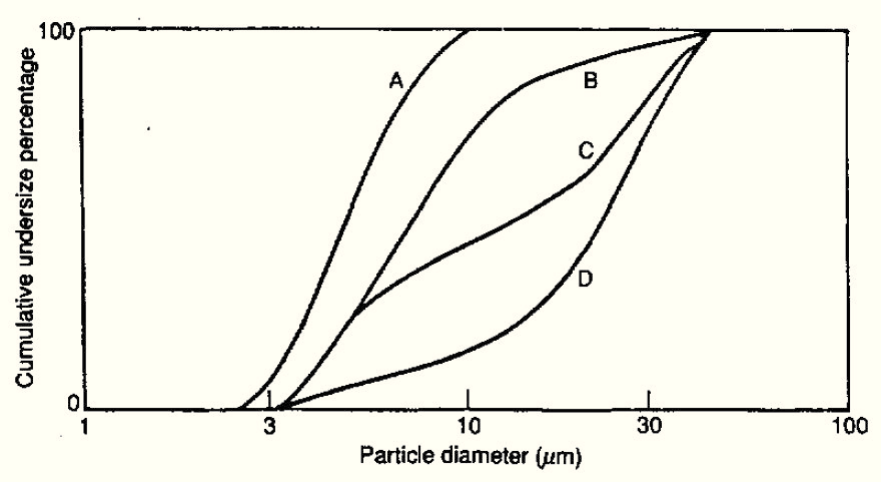

Figure 2.10: Particle size distribution of various powders [10]

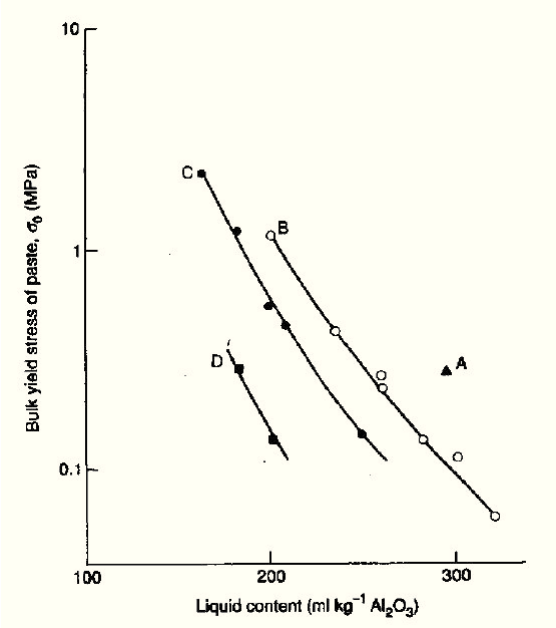

Figure 2.11: Initial bulk stress of paste versus plastifier content for pastes made with particle size distributions given in figure 2.10 [10]

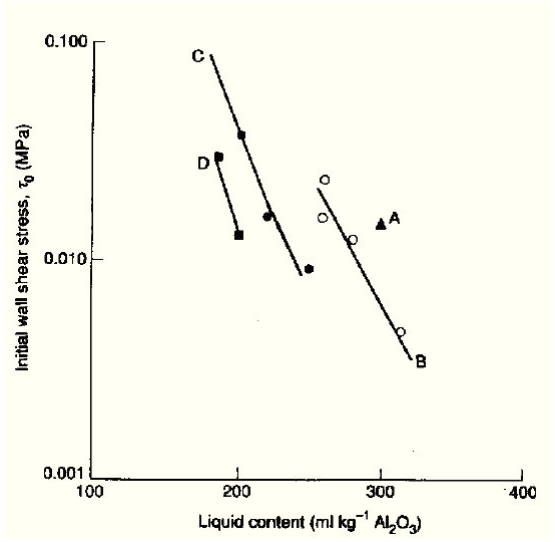

Figure 2.12: Initial wall stress of paste versus plastifier content for pastes made with particle size distributions given in figure 2.10 [10]

2.3.2 Sintering, HIP and Sinter HIP

Sintering fuses the various components of the hardmetal. WC-Co based hard metals can be sintered, using a hydrogen atmosphere within the oven. Sintering furnaces can either use a vacuum-induction technology (a), be designed to work continuously using a graphite heating element (b) or conduct the sintering process horizontally, discretely also using graphite heating elements and graphite insulation (c). The various options are displayed in figure 2.13. Multiple graphite heating elements ensure a homogeneous temperature distribution in the oven. In order to skip the presintering process it is necessary to separate the wax and vaporize the additives. Carburization of the hard metal during the sintering process can be controlled through gas injection into the oven. High vacuum diminishes cobalt loss. The cooling process is accelerated by gas injection, using gas with a high heat conductivity coefficient and ventilators to enhance convection. [1]

During the sintering process the following parameters can be adjusted [1]:

- Heating rate
- Time at set temperature
- Maximum temperature
- Atmosphere: Sintering can take place in H_2- or Ar-atmosphere and vacuum.
- Pressure
- Gas flow rate
- Cooling rate

An example of a sintering process is given in figure 2.14. The evaporation of the wax is typically conducted within an H_2 atmosphere at temperatures around 650 °C. For

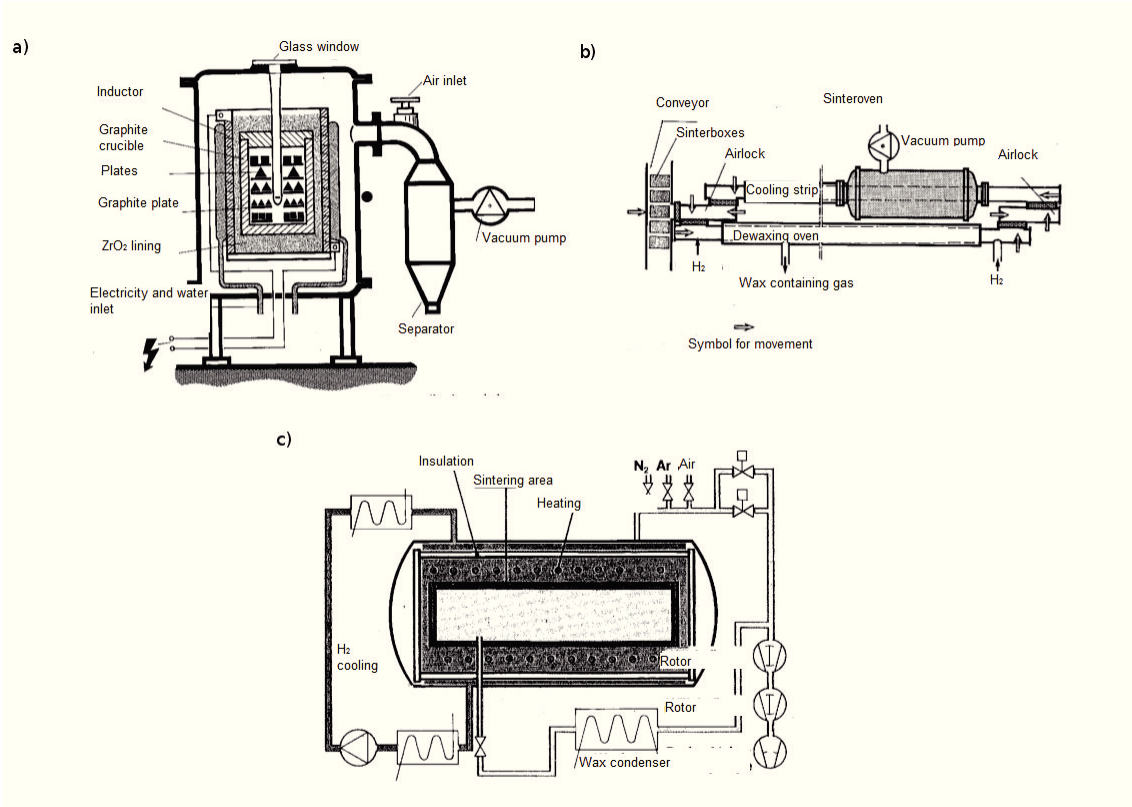

Figure 2.13: Different oven models for sintering hardmetall powders [1]

presintering the temperature is raised to about 900 °C. Pressures range between 0.1 mbar for vacuum sintering and 100 bar for sinter HIP. The maximum temperature is around 1400 °C. [1]

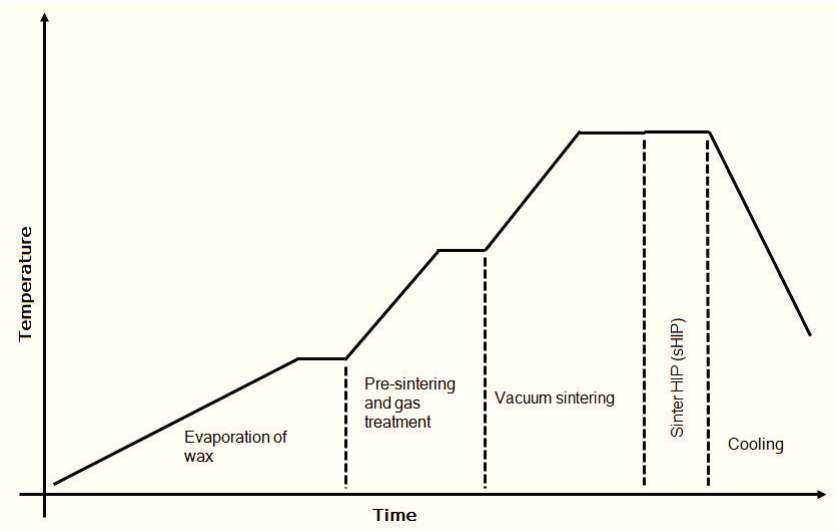

Figure 2.14: Temperature characteristics of a sintering process [2]

Using mass spectrometry and differential scanning calorimetry, the sintering process

can be monitored as displayed in figure 2.15. Between 20 °C and 200 °C the moisture and the wax evaporate. Further evaporation of the wax and the reduction of Co takes place between 200 °C and 600 °C. CO and CO_2 is produced due to the reduction process. At temperatures ranging from 600 °C to 1100 °C, WC is reduced, more CO and CO_2 is produced and shrinkage sets in. The shrinkage maximum is reached at 1250 °C. Due to the eutectic, a liquid phase coexists with the solid phase at temperatures ranging from 1100 °C to 1450 °C. The eutectic temperature is 1320 °C (see figure 2.16). [1]

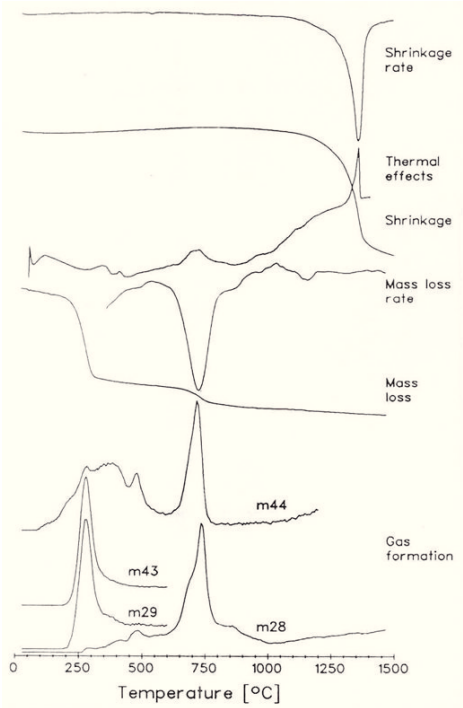

Figure 2.15: Sintering process [2]

The properties of the binder phase are greatly influenced by the amount of carbon involved in the process. Following parameters influence the total carbon amount [1]:

- Amount of carbon in the powder mixture
- Cracking of the compression moulding additives during the vaporization process
- The oxygen content in the cobalt binder and the carbides influences the sintering process and can lead to high or low carbon losses within the material, depending on the oven atmosphere

The vaporization of volatile substances should ideally be over before the formation of the liquid phase begins, in order to avoid big pores. [1]

HIP is a technology which allows a reduction of pores within the material, after the sintering process, through applying hot isostatic pressure (figure 2.17). The cemented carbide is exposed to pressures around 1000 bar, at temperatures comparable to the ones occurring during the sintering process. The goal is to plastically

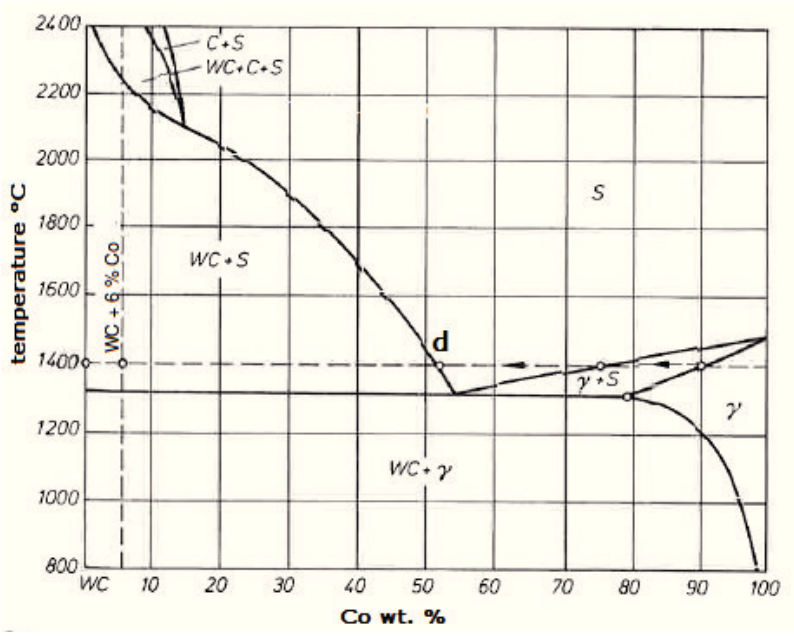

Figure 2.16: WC-Co phase diagram [8]

deform the hard metal into the pore, in order to eliminate it. A prerequisite for the success of this process is, that the pore in question has no connection to the surface of the hard metal. If this doesn't apply, the pore can't be closed through HIP. Also gaseous pores can't be closed. Most likely it is binder phase which is pushed into the pore, which states a disadvantage. The more WC is dissolved within the liquid binder phase, the more homogeneously the microstructure within the filled pore will be, when the WC precipitates during cooling. A further limitation of the process is, that pores often evolve around inclusions. HIP can eliminate the pores around the inclusion at best, but not eliminate the inclusion itself. The temperature and pressure profile of a HIP treatment is displayed in figure 2.18. [1, 8]

Sinter HIP is a combined technology, that sinters under vacuum and applies around 100 bar of pressure directly afterwards. [8]

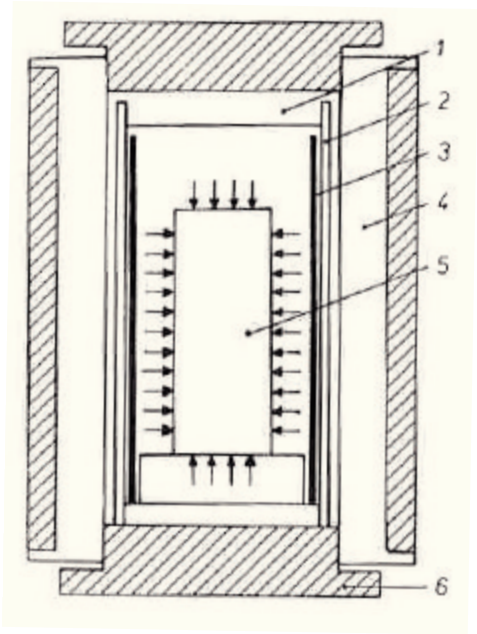

Figure 2.17: Sinter HIP oven, 1) insulating lid 2) insulating layer 3) oven 4) pressure vessel 5) sample [8]

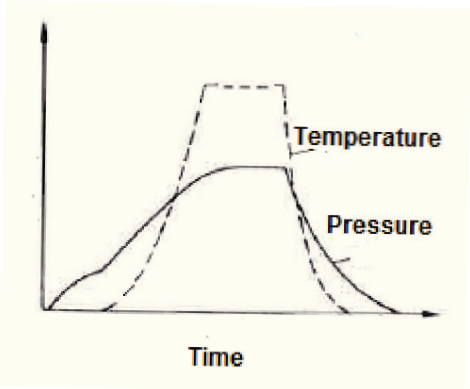

Figure 2.18: Temperature and pressure profile of a HIP treatment [8]

2.4 Microstructure

Cemented carbides consist of carbides and a binderphase. The microstructure of cemented carbides can either be seen as carbides in a binderphase matrix, separated only by a next to nothing amount of binder phase at the contact points, or it can be seen as a skeleton of carbides filled with the binder phase. Following factors determine the microstructure: [1]

- **Binderphase/carbide ratio:** The higher the binderphase content is, the thicker the layers between the carbides present themselves, the more ductile the cemented carbide is.
- **Formation of new phases:** The formation of new phases, through a combination of binderphase and carbide is generally unwanted. Under special circumstances, the formation of new phases can lead to favourable material properties.
- **Wettability of carbides:** Wettability of the carbides through the binderphase influences the strength of the boundary layer and the degree to which a "carbide skeleton" is formed. The higher the wettability is, the lower the tendency to form a skeleton and consequently the strength of the material increases.
- **Solubility of carbides in the binder phase:** The temperature dependency of the solubility influences the sintering processes as well as the material properties of the binderphase.
- **Strength of the binder phase:** The strength of the binderphase is influenced by the strength of the material itself and the thickness of the layer.
- **Thermal expansion coefficients:** Differing values for the individual phases can lead to stress within the material.
- **Grain size and grain size distribution:** The smaller the grain size is, the more surface there is for the binderphase to cover, which results in a thinner binderphase layer between the carbide particles.
- **Grain shape of the carbide particles:** The shape of the carbide particles also influences the amount of surface the binderphase has to cover.
- **Contiguity:** The contiguity describes the degree to which the carbides form a "skeleton". The contiguity depends on the amount of binderphase, the wettability and the sintering conditions.
- **Amount of porosity and defects**

Due to the powder technology, there is no cleansing the liquid phases through slag, which inevitably leads to defects, inclusions and porosity within the material. Varying densities within the material due to suboptimal compression moulding, can lead to porosity and other defects. The sinter HIP technology gives an opportunity to close some of the pores, with the disadvantage of replacing the pores with mostly binderphase, graphite or other inclusions.

2.4.1 Microstructural changes due to the sintering process

The carbon-tungsten phase diagram 2.19 shows that WC is unstable above 2600 °C and decomposes into W_2C and C at temperatures exceeding 2600 °C. This instability is the reason for the necessity of a sintering process in order to produce cemented carbides consisting of tungsten monocarbides and cobalt.

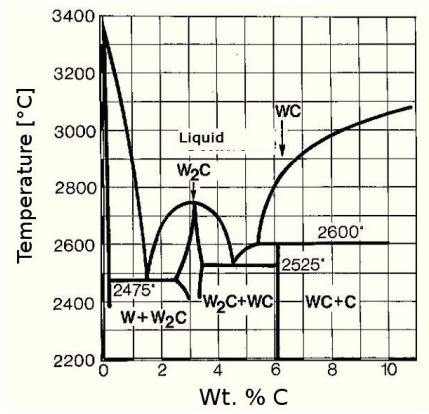

Figure 2.19: W-C phase diagram [1]

The formation of the WC-Co cemented carbide crystal structure is greatly influenced by the interaction of the two components at sintering temperature. Figure 2.20 presents three phase diagrams of different authors displaying the phases found at 1400 °C. The differences are due to difficulties conducting the experiments.

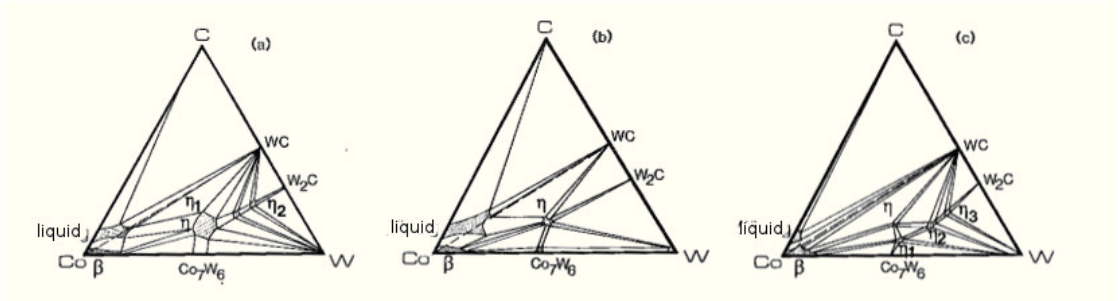

Figure 2.20: W-C-Co phase diagram at 1400 °C [1]

A newer study states a WC-Co system containing two η-phases. An η-phase occurs at hypostoichiometric conditions concerning the presence of carbon. Its chemical composition is Co_3W_3C. It is a very brittle phase and generally unwanted. Figure 2.21 shows the ternary phase diagrams at 1260 °C, with only a small amount of liquid phase. The second diagram in figure 2.21 displays the eutectic depressions, that would be visible in an 3D ternary phase diagram. The arrows indicate that the eutectic depressions would go towards lower temperatures. The dotted lines indicate the borders of the liquid phase at 1400 °C and 1500 °C.

The area within the phase diagram, that does not lead to the exsolution of WC is very small ($W : C \approx 1$). If $W : C < 1$, the carbon exsolutes as graphite. If

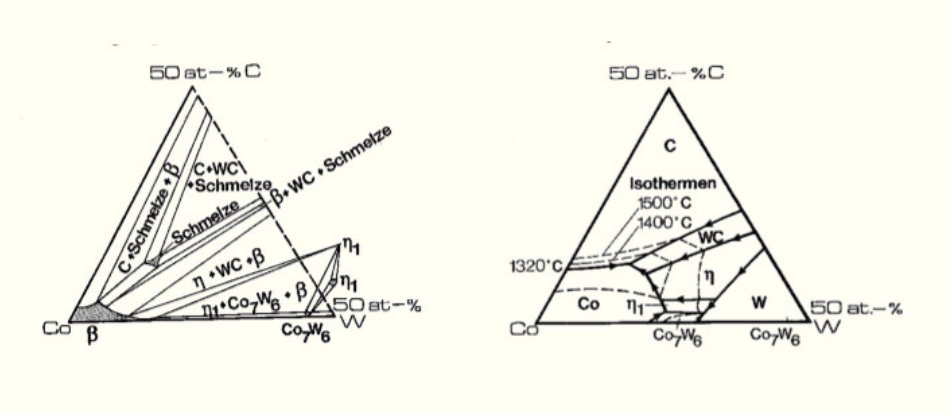

Figure 2.21: W-C-Co phase diagram at 1260 °C [1]

$W : C > 1$, the formation of the η-phase sets in.

During the moulding process the WC and Co particles come in very close contact with each other. Once the temperature begins to rise in the course of the sintering process, diffusion processes gain weight. The Tamman temperature is a method to describe the different stages of the sintering process, taking the melting point of the components into account. The Tamman temperature is the fracture of the current temperature by the melting temperature of the material. At temperatures, exceeding 0,25 Tamman temperature the atoms can diffuse from one particle surface onto another. Temperatures exceeding 0,5 Tamman lead to diffusion through the whole crystal lattice. The fluctuation of material through the lattice leads to grain growth, which is generally not desired.

Figure 2.16 displays the relevant phases of a 94WC6Co hardmetal during the sintering process and the subsequent cooling. With rising temperatures during the heating process more and more tungsten carbide and free floating carbon dissolve into the cobalt matrix. The volume reduces itself at temperatures, exceeding 700 °C due to solid phase sintering. The composition of the binderphase during the heating process follows the borderline of phase γ in figure 2.16. The W-C-Co eutectic melts at temperatures exceeding 1280 °C. Even more WC dissolves into the now liquid phase. At temperatures typically for sintering (1400 °C), the composition equals point d in figure 2.16. The volume fracture of the liquid phase at point d equals 15.6 vol. %, which is more than enough for the liquid phase to wet the WC particles like a brazing alloy, which causes the particles to move closer together due to the surface tension. This explains why the sintering process causes a considerable volume contraction by elimination of pores. In order to reduce the surface area, the WC grains grow during the sintering process. During cooling the WC precipitates until the temperature is too low for diffusion to happen. The remaining WC within the cobalt binder stabilises the fcc microstructure, which would otherwise change to hex at 417 °C. Due to the different thermal expansion coefficients, the cooling process causes tensile stress in the cobalt phase and compression stress within the WC-phase, which delays the destruction of the brittle phase under mechanical stress. [1, 8]

2.4.2 Carbon balance

The carbon balance during the sintering process has a great influence on the microstructure and consequently the mechanical properties of the sintered product. Figure 2.22 displays the targeted area regarding the degree of carburization, in order to achieve an optimum of hardness and ductility. Less carburization allows a higher solubility of WC in Co. Figure 2.23 shows the results of a carbon deficiency (a) and carbon excess (b) during the sintering process. The influence of the carburization degree on the mechanical properties is displayed in figure 2.24. In order to achieve a carbon balance within the desired range the carbon and oxygen contents of all the components present (atmosphere, hard metal, oven insulation) during the sintering process must be regarded.

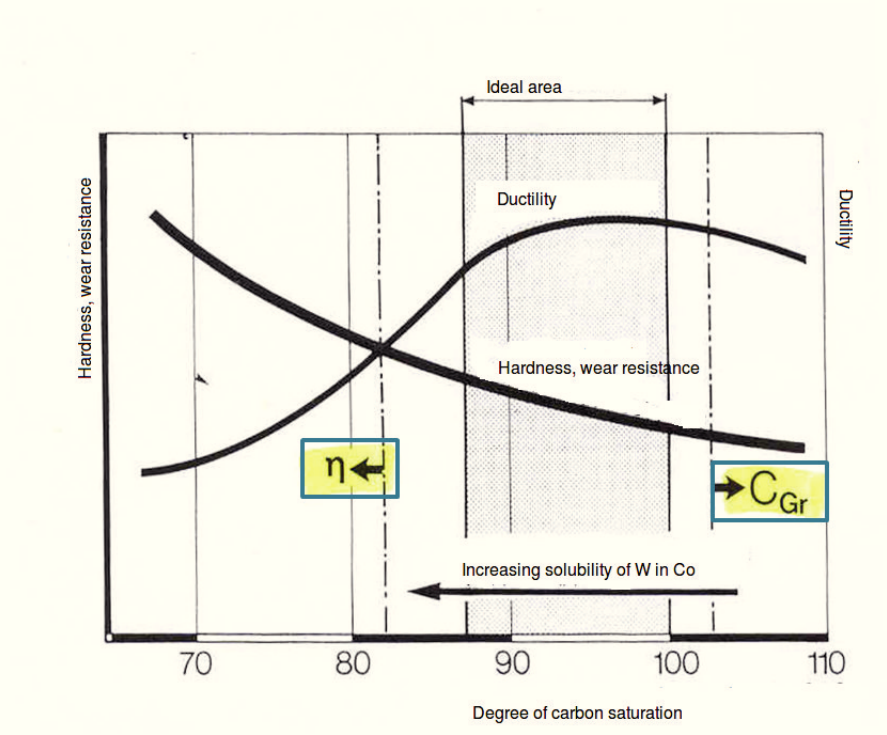

Figure 2.22: Carbon balance and mechanical properties of cemented carbides [1]

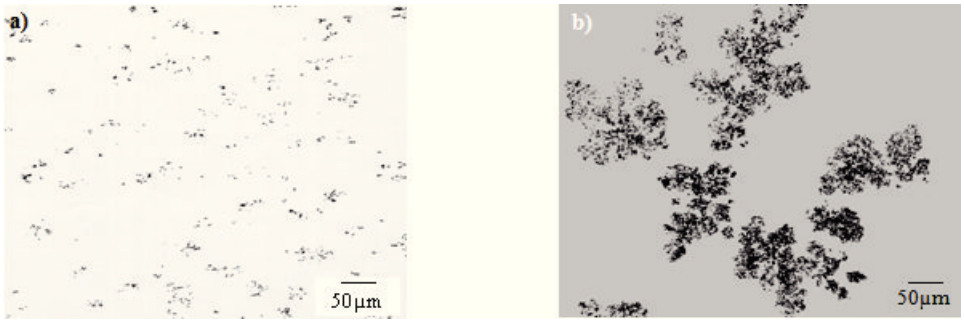

Figure 2.23: M
icrostructure with a) η-phase b) Free carbon [2]

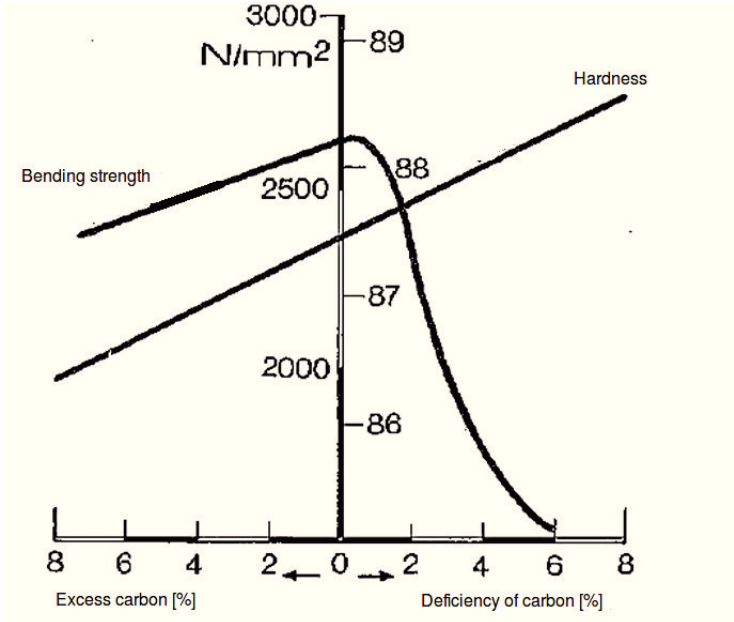

Figure 2.24: Carbon balance and mechanical properties of cemented carbides [1]

3 Experiments and Results

Experiments were conducted on two different hard metals varying in cobalt content, grain size of the WC grains and grain size of the sintered material in order to determine the resulting microstructure. Table 3.1 shows the material properties mentioned. The two different materials were moulded, using either dry-bag, direct or extrusion moulding. The moulded material was thereafter treated either through pre-sintering, sintering, sinter HIP or sintering and HIP. The presintering was conducted at 1150 °C, in order to preserve the original structure of the raw material, preventing the occurrence of a liquid phase. The flowsheet in figure 3.1 displays an overview of the investigated samples. The following code was used to label the samples:

- **Material:** The first letter of the code describes the material. It is either **X** or **Y**.
- **Manufacturing method:** The second sequence specifies the manufacturing method.
  - **S:** extrusion moulding
  - **DB:** dry-bag moulding
  - **D:** direct moulding
- **Pressure treatments:** The last part of the code describes the applied pressure treatment.
  - **VS:** presinted
  - **S:** sintered
  - **SH:** sinter HIP
  - **NV:** HIP

Properties	**X**	**Y**
Co content	10	8.2
Grain size of WC	0.75	0.6
Grain size of sintered material [μm]	≤ 0.5	0.5-0.8

Table 3.1: Material properties of samples

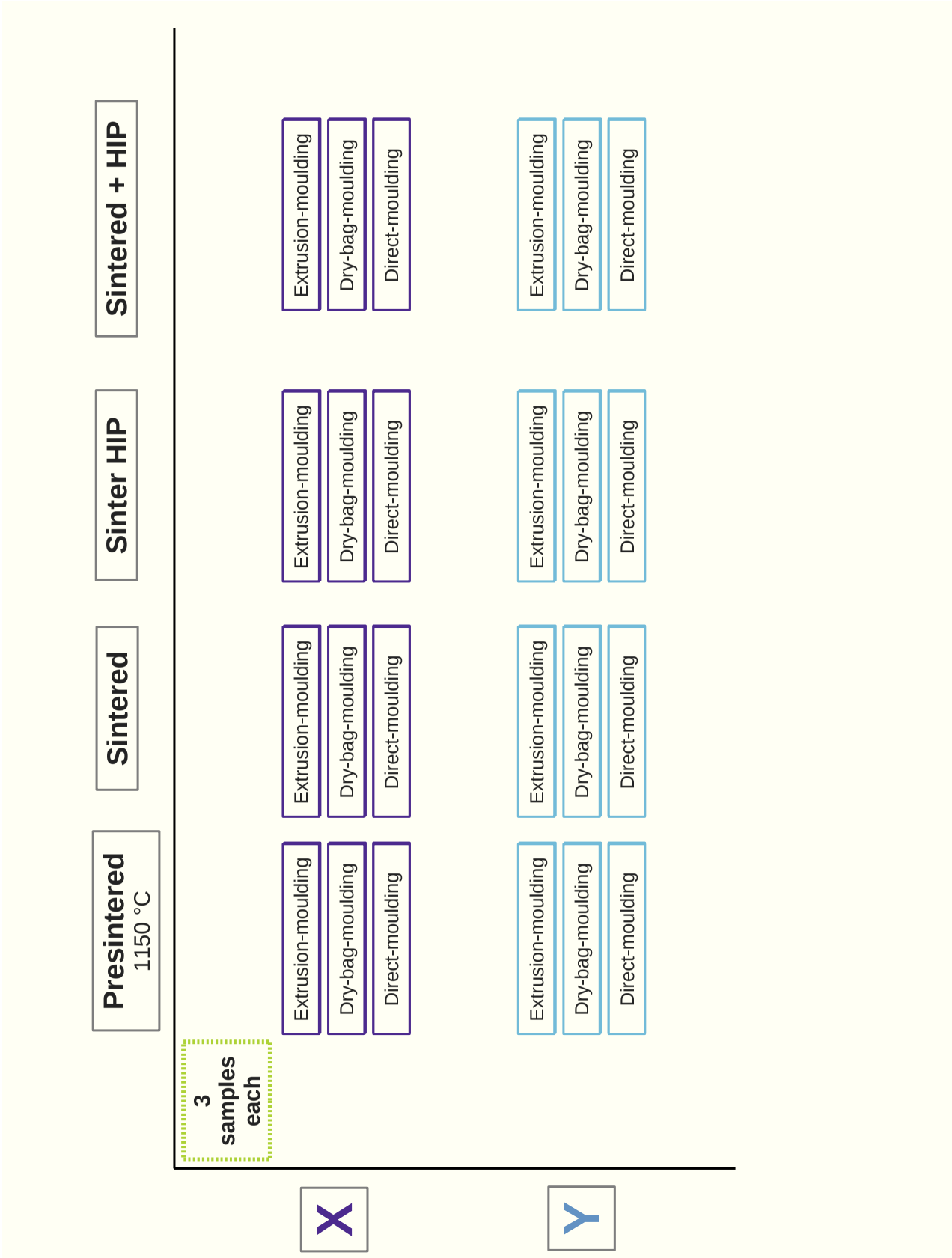

Figure 3.1: Flowsheet, displaying experimental matrix of materials and their treatments

3.1 Metallographic investigation

The metallographic investigation was conducted through a Nikon Eclipse MA 200 microscope operated by NIS-Elements 4.10 software. Samples were cut from moulded products in a radial direction (Struers DiscoTom-2), embedded (Struers ProntoPress 20, Struers CitoPress 20), abraded, polished (Struers Rotopol-22) and cleaned prior to the investigation.

3.1.1 Porosity

The porosity was determined, according to the ISO 4505 standard displayed in figure 3.2.

A-porosity are pores with a diameter < 10 μm. Depending on the frequency of their occurrence, the A-pores are classified as A02 (none or few pores), A04, A06 and A08 by comparing the surface of the sample to the standard, displayed in figure 3.2. It is also possible to rate the porosity between the set classes (f.e. A02-A04).

B-porosity are pores with a diameter ranging from 10 μm to 25 μm. According to ISO 4505 they can be classified as B02, B04, B06 and B08. For a more detailed classification, B-pores are classified according to table 3.2. In order to assess the number of B-pores, the whole surface of the sample must be investigated and the pores counted. To determine the B-porosity the number of B-pores is divided by the surface area of the sample to obtain the number of pores per cm^2. B-porosities exceeding >B04 are determined via comparison with the standard displayed in figure 3.2.

	Number of pores 10-25 μm per cm^2
<B02	1-28
B02	29-140
<B04	141-226
B04	227-430
<B06	431-690
B06	691-1300
<B08	1301-2100
B08	2101-4000

Table 3.2: Classification of B-porosity

Macro-porosity is class divided into pores with diameters from 25-75 μm, 75-125 μm and >125 μm. Pores, visible on the surface of the sample are counted and divided by the sample surface area in order to obtain the number of pores per cm^2.

In order to conduct the following metallographic investigations, the samples had to be etched electrical with a Muracami solution (150 ml dest. water, 6 g KOH, 4 g

potassiumferricyanide $K_3[Fe(CN)_6]$) at 2.1 V.

The α-phase (WC) was described by means of finding and measuring the biggest WC-grain on the surface of the sample. Once found, two perpendicular lines were drawn, attempting to cover the maximum diameter of the WC-grain. Then the mean average value of the line lenghts was calculated and estimated as the maximum WC-grain size.

The β-phase (Co, binderphase) was described by counting every Co filled area >10 μm and dividing it by the surface area of the sample. Also Co-accumulations, in samples treated with HIP and sinter HIP, which would have appeared as a pore in a sintered sample, were counted and divided by the surface area.

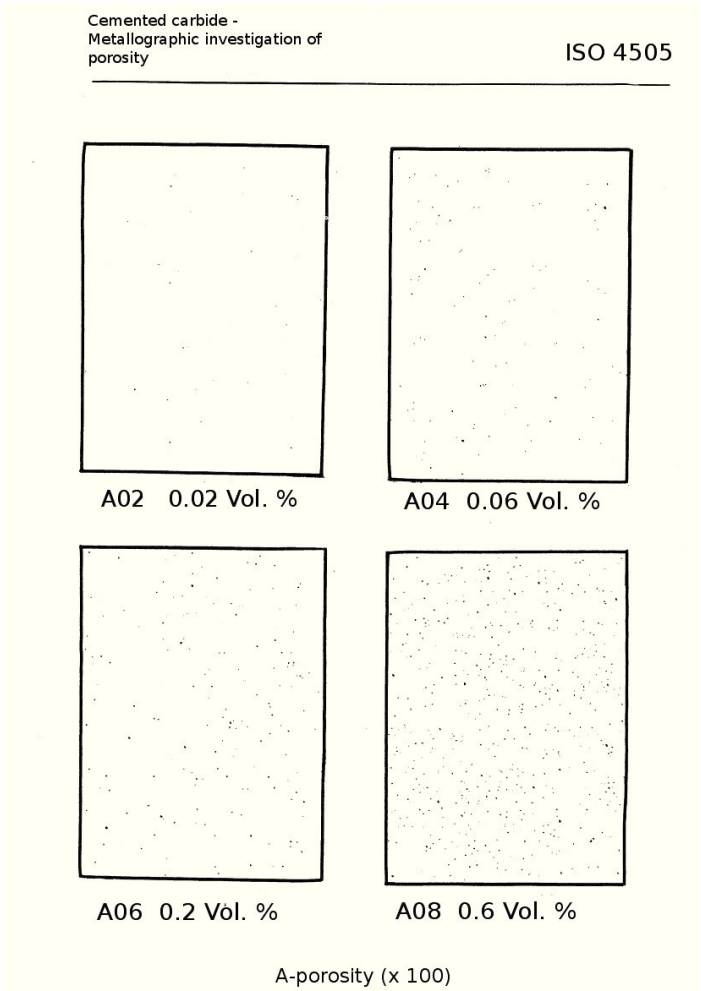

(a) Classification of A-pores

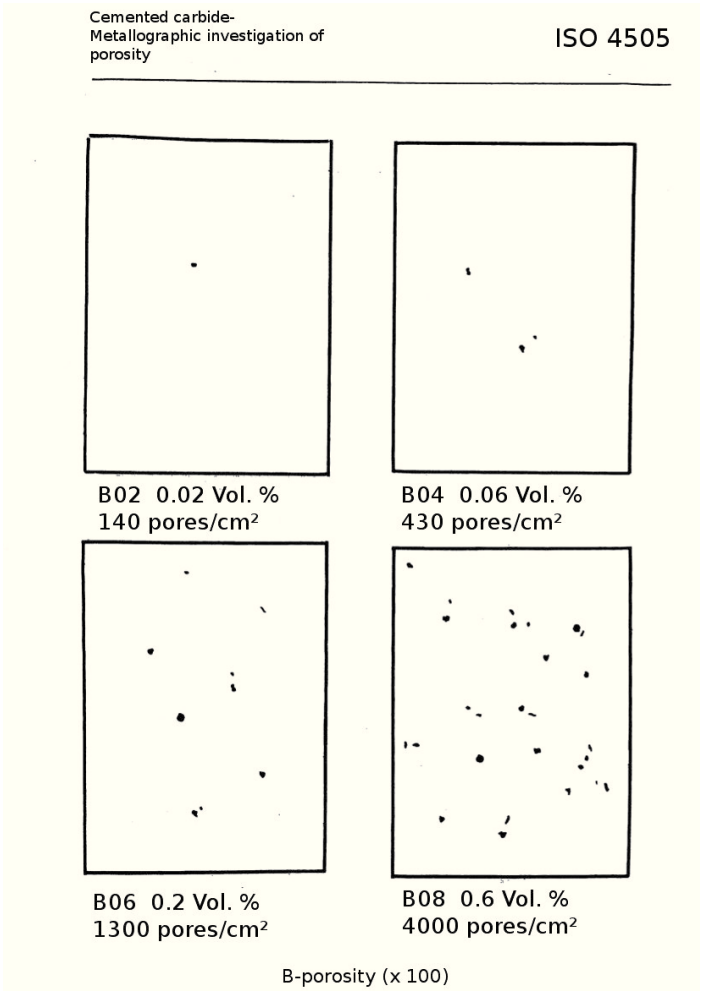

(b) Classification of B-pores

Figure 3.2: ISO 4505 standard for classifacation of pores in cemented carbides

Figures 3.3, 3.4 and 3.5 give an overview of the investigated samples and the results. Pores occurring in samples, treated with pressure (HIP or sinter HIP) are marked yellow. These pores could cause the material to fail during operation (figure 3.10d). Pores marked light green are likely to turn into Co-accumulations that are marked dark green (figures 3.9d, 3.9e and 3.9f). Pores marked blue are replaced perfectly by homogeneous microstructure due to the pressure treatment. Co-phases, connected to pores, are marked light and dark pink respectively (figure 3.9d). Areas referred to as "granu" in the table are agglomerates of powder, that were not smashed by milling or moulding (figures 3.11d, 3.11e and 3.11f). Diagrams, displaying the results found within the figuress 3.3, 3.4 and 3.5 can be found in the appendix.

	A-porosity	B-porosity	No of B-pores/cm²	25-75 µm	75-125 µm	> 125 µm	WC max.	Co-Phase	Co-acc.
X S S									
sample 1	A04	<B02	10	8	2	0	6	lots < 110 µm	
sample 2	A02	<B02	12	2	0	0	11	71	
sample 3	A02	<B02	42	2	0	0	9	51	
sample 4	A02	<B02	23	0	0	0	6	24	
sample longitudinal	A02	<B02	19	12	1	0	8	51	
X S SH									
sample 1	A02	B00	0	0	0	0	5		
sample 2	A02	B00	0	0	0	0	5	0	32
sample 3	A02	B00		0	0	0	4	0	23
sample 4	A02	<B02	1	0	0	0	4	0	42
sample longitudinal	A02	B00		0	0	0	9	0	15
X S NV									
sample 1	A02	B00	0	0	0	0	7	0	
sample 2	A02	B00	0	0	0	0	6	0	25
sample 3	A02	<B02	5	1	0	0	7	0	26
sample 4	A02	B00	0	0	0	0	9	0	23
sample longitudinal	A02	B00	0	0	0	0			27
Y S S									
sample 1	A02	<B02	17	26	6	6	4		
sample 2	A02	B02	76	1	0	0	4	6	
sample 3	A02	B02	75	1	0	0	4	18	
sample 4	A02	B02	111	0	0	0	4	14	
sample longitudinal	A02	B02	34	11	1	2	4	10	
Y S SH									
sample 1									
sample 2	A02	<B02	23	0	0	0	4	0	25
sample 3	A02	B00	0	0	0	0	4	0	70
sample 4	A02	B00		0	0	0	4	0	57
sample longitudinal	A02	B00	0	0	0	0	4	0	16
Y S NV									
sample 1									
sample 2	A02	B00	0	0	0	0	4	0	
sample 3	A02	B02	32	0	0	0	4	0	
sample 4	A02	B00	0	0	0	0	4	0	
sample longitudinal	A02	B00	0	0	0	0	4	0	

Figure 3.3: Results of metallographic investigation of extrusion moulded samples

	A-porosity	B-porosity	No of B-pores/cm²	25-75 µm	75-125 µm	> 125 µm	WC max.	Co-Phase	Co-acc.
X DB S									
sample 1	A02	B00	0	0	0	0	7	0	
sample 2	A04	<B02	2	0	0	0	6	15	48
sample 3	A04	<B02	3	0	0	0	8	18	53
sample 4	A04	<B02	3	1	0	0	10	14	60
X DB SH									
sample 1	A02	B00	0	0	0	0	11	0	
sample 2	A02	B00	0	0	0		11	1	
sample 3	A02	B00	0	0	0		13	0	
sample 4	A02	B00	0	0	0		10	0	
X DB NV									
sample 1									
sample 2	A02	B00	0	0	0	0	9	1	
sample 3	A02	B00	0	0	0	0	10	0	
sample 4	A02	B00	0	0	0	0	8	0	
Y DB S									
sample 1	A08	B02	47	13	0	0	4	some	
sample 2	A06	<B02	20	2	0	0	4	50	
sample 3		B02	44	0	0	0	4	28	
sample 4		<B02	21	0	0	0	4	17	
Y DB SH									
sample 1	A02	B00	0	0	0	0	4	0	
sample 2	A02	B00	0	0	0	0	8	granu	
sample 3	A02	B00	0	0	0	0	5	granu	
sample 4	A02	B00	0	0	0	0	4	granu	
Y DB NV									
sample 1									
sample 2	A02	B00	0	0	0	0	4	granu 5	
sample 3	A02	B00	0	0	0	0	4	granu 4	
sample 4	A02	B00	0	0	0	0	4	granu 3	

Figure 3.4: Results of metallographic investigation of dry-bag moulded samples

	A-porosity	B-porosity	No of B-pores/cm²	25-75 µm	75-125 µm	> 125 µm	WC max.	Co-Phase	Co-acc.
X D S									
sample 1	A06	B02		lots	0	0	7		
sample 2	A06	B02	71	0	0	0	7	5	
sample 3	A06	B02	58	0	0	0	9	3	
sample 4	A06	B02	46	0	0	0	9	6	
X D SH									
sample 1	A02	B00	0	0	0	0	9		
sample 2	A02	B00	0	0	0	0	10	granu	
sample 3	A02	B00	0	0	0	0	5	granu	
sample 4	A02	<B02	2	0	0	1	5	granu	
X D NV									
sample 1									
sample 2	A02	B00	0	0	0	0	6	0	
sample 3	A02	B00	0	0	0	0	12	0	
sample 4	A02	B00	0	0	0	0	6	0	
Y D S									
sample 1	A04	<B02	18	8	0	0	4	some	
sample 2	A06	<B02	15	5	0	1	4	16	
sample 3	A06	<B02	25	1	0	2	4	11	
sample 4	A04	<B02	18	0	0	0	4	21	
Y D SH									
sample 1	A02	B00	0	0	0	0	4		
sample 2	A02	<B02	3	0	0	1	5	1	
sample 3	A02	B00	0	0	0	1	5	1	
sample 4	A02	B00	0	0	0	1	5	1	
Y D NV									
sample 1									
sample 2	A02	B00	0	0	0	2	5	2	
sample 3	A02	B00	0	0	0	2	5	1	
sample 4	A02	B00	0	0	0	2	5	0	

Figure 3.5: Results of metallographic investigation of direct moulded samples

Presintered samples were sintered at 1150 °C, this being the highest temperature possible without any liquid phases occuring. Preventing liquid phases in the presintering process is important, because the presintered material was investigated in order to get an idea of what the raw moulded material looks like. The raw material itself is too soft to undergo a standard metallographic investigation. Figures 3.6, 3.7 and 3.8 display presintered samples. In order to get some quantitative results, the hardness (HV10) of the presintered samples was measured. The mean average values of the results are displayed in table 3.3.

	X_S_VS	**Y_S_VS**	**X_DB_VS**	**Y_DB_VS**	**X_D_VS**	**Y_D_VS**
HV 10	91	256	91	262	75	195

Table 3.3: Values of measured vickers hardness in presintered samples X and Y cemented carbides

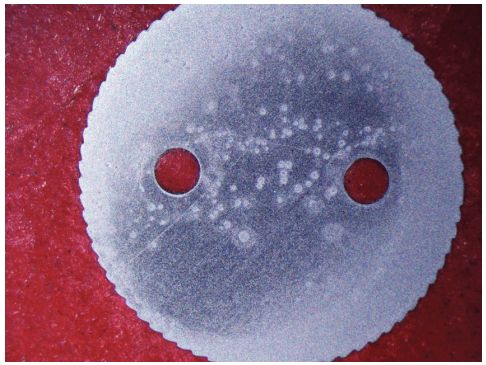

(a) Overview

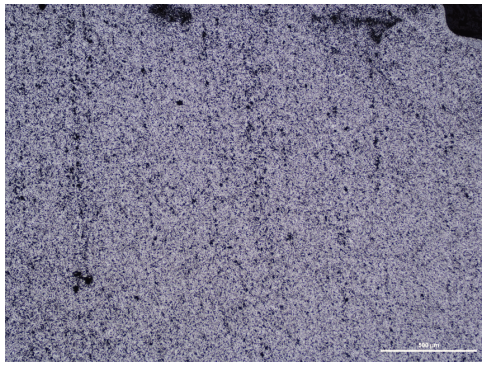

(b) Length of bar is 500 μm

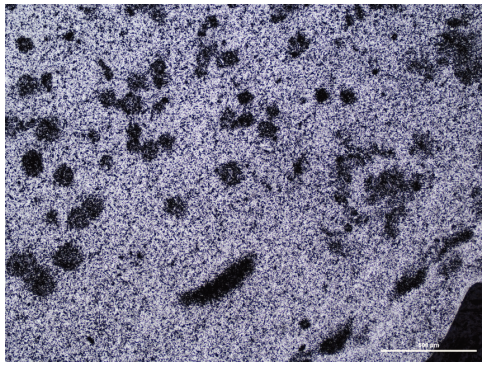

(c) Length of bar is 500 μm

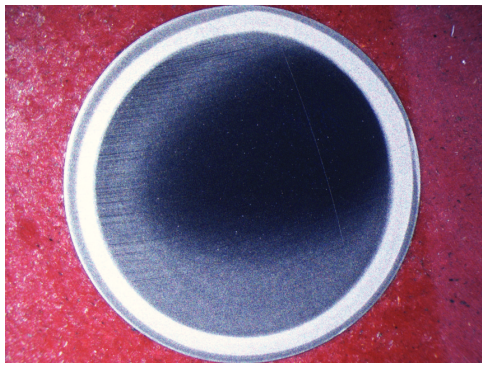

(d) overview

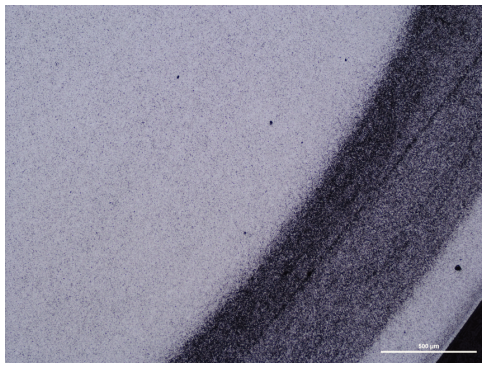

(e) Length of bar is 500 μm

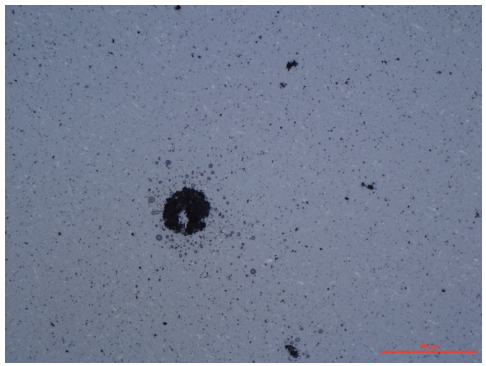

(f) Length of bar is 50 μm

Figure 3.6: Characteristics of presintered extrusion moulded X (top) and Y (bottom) samples

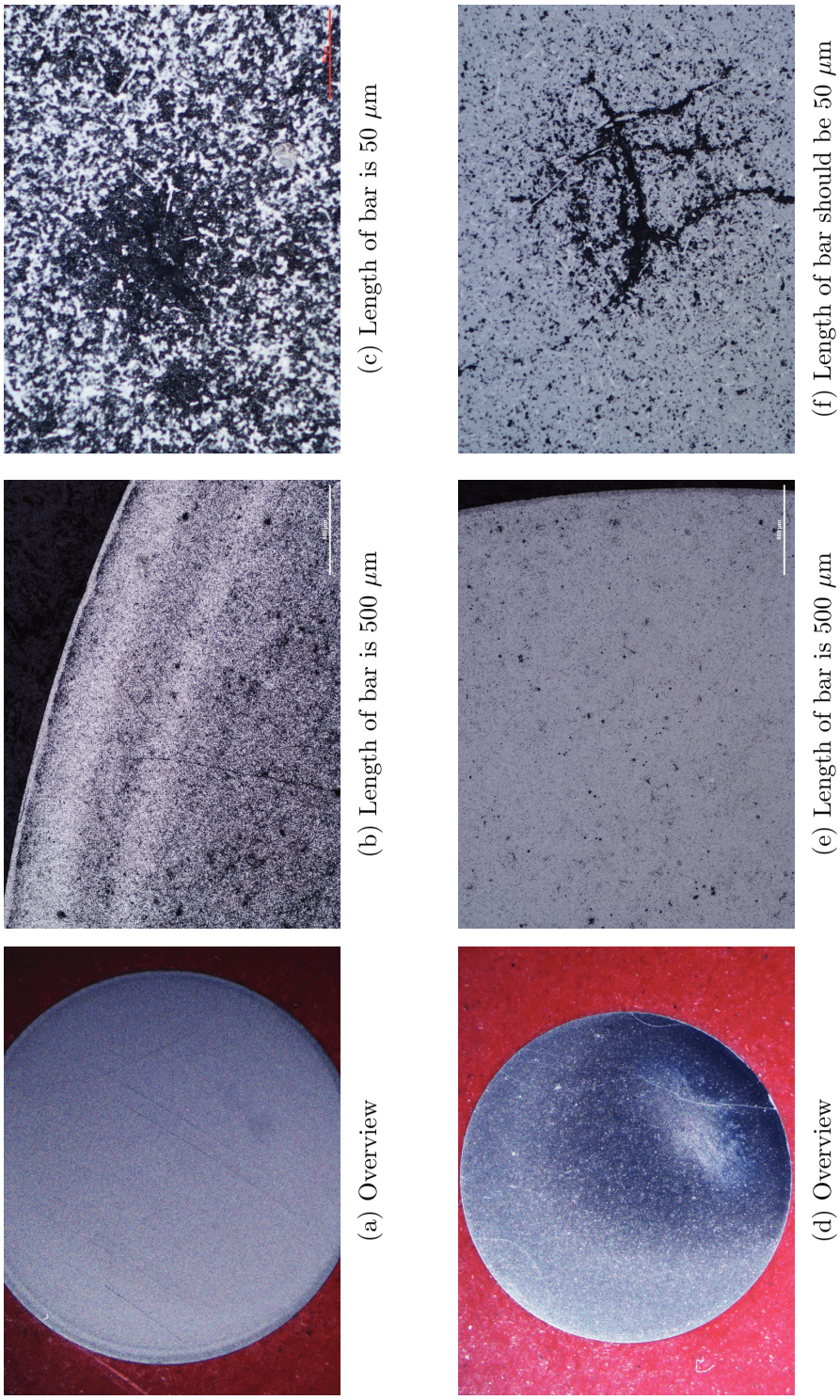

(a) Overview (b) Length of bar is 500 μm (c) Length of bar is 50 μm

(d) Overview (e) Length of bar is 500 μm (f) Length of bar should be 50 μm

Figure 3.7: Characteristics of presintered dry-bag moulded X (top) and Y (bottom) samples

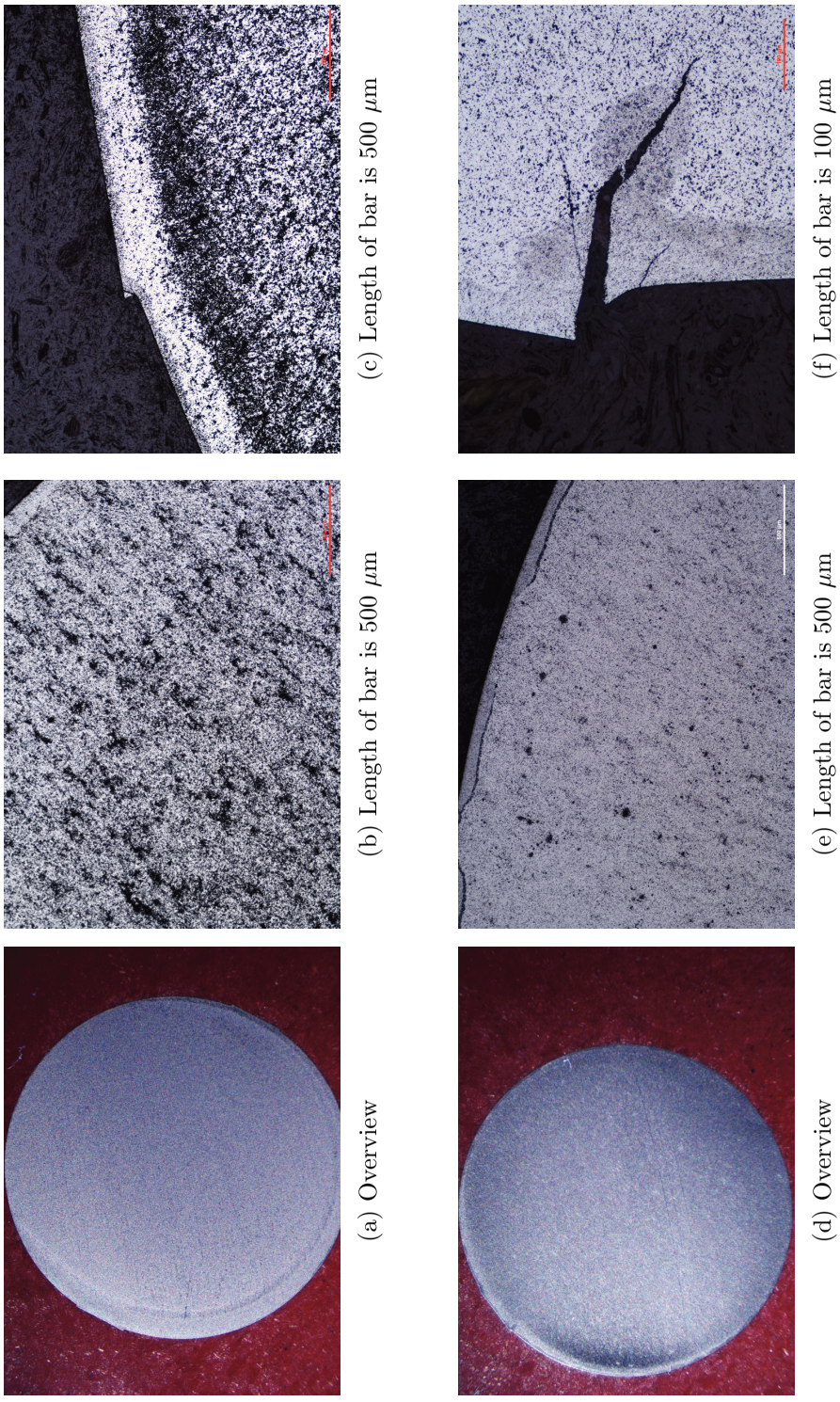

(a) Overview (b) Length of bar is 500 μm (c) Length of bar is 500 μm

(d) Overview (e) Length of bar is 500 μm (f) Length of bar is 100 μm

Figure 3.8: Characteristics of presintered direct moulded X (top) and Y (bottom) samples

The transformation of the microstructure due to the pressure treatment is documented in figures 3.9, 3.10, 3.11 and 3.12. Figures 3.13b and 3.13a show defects due to wrongly adjusted direct moulding tools. Figures 3.13c and 3.13d are pictures of samples taken from an extruded product in axial direction.

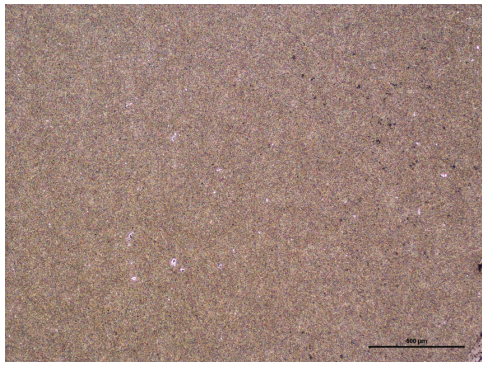

(a) X, extrusion moulded, sintered, length of bar is 500 μm

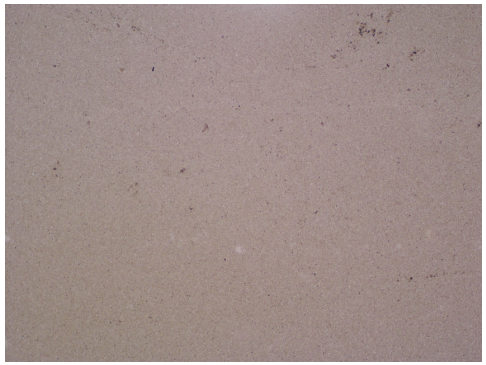

(b) X, extrusion moulded, sHIP, length of bar should be 500 μm

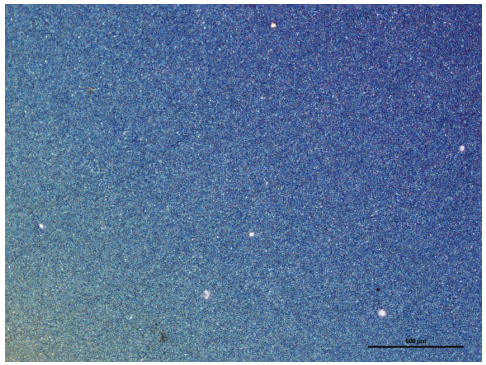

(c) X, extrusion moulded, HIP, length of bar is 500 μm

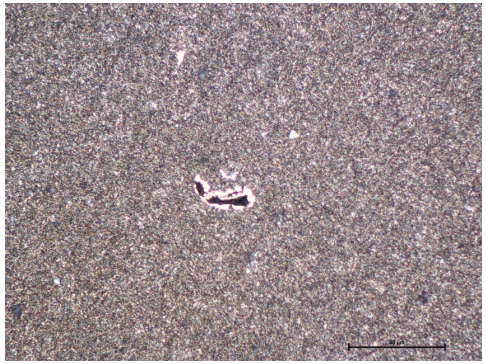

(d) X, extrusion moulded, sintered, pore, length of bar is 50 μm

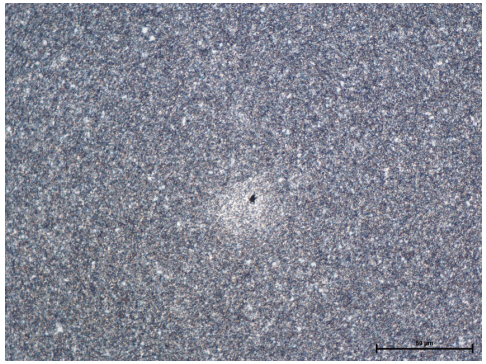

(e) X, extrusion moulded, sinter HIP, pore, length of bar is 50 μm

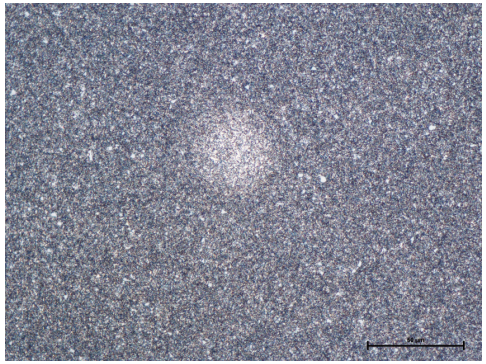

(f) X, extrusion moulded, HIP, pore, length of bar is 50 μm

Figure 3.9: Characteristics of extrusion moulded X

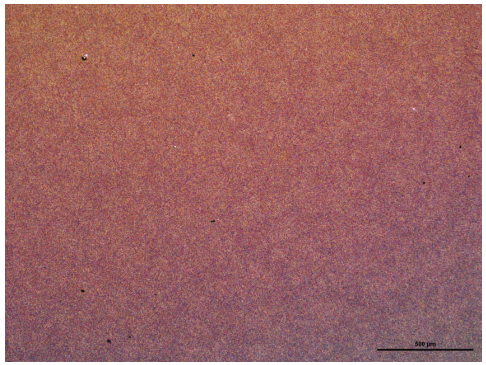

(a) Y, extrusion moulded, sintered, length of bar is 500 μm

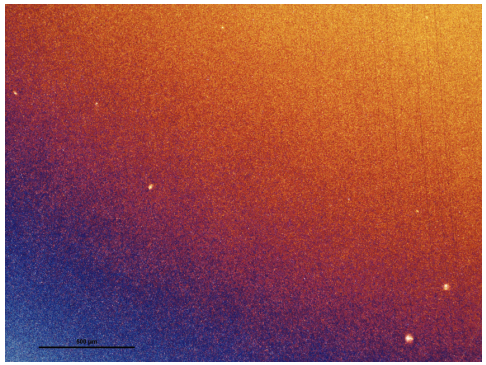

(b) Y, extrusion moulded, sHIP, length of bar is 500 μm

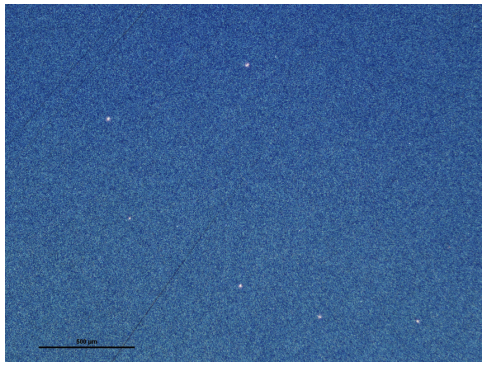

(c) Y, extrusion moulded, HIP, length of bar is 500 μm

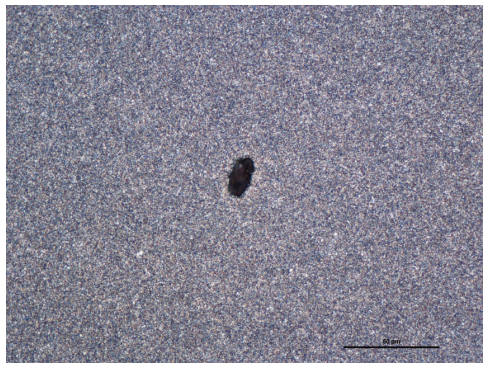

(d) Y, extrusion moulded, HIP, pore, length of bar is 50 μm

Figure 3.10: Characteristics of extrusion moulded Y

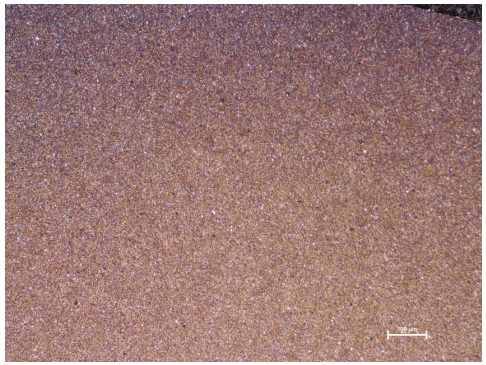

(a) X, dry-bag moulded, sintered, length of bar is 100 μm

(b) X, dry-bag moulded, sHIP, length of bar is 100 μm

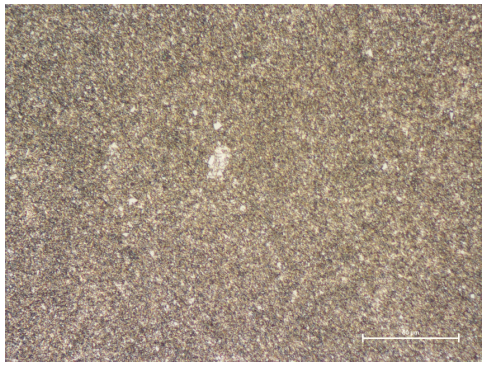

(c) X, dry-bag moulded, HIP, length of bar is 50 μm

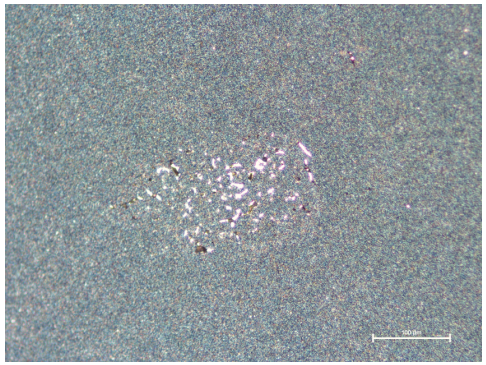

(d) Y, dry-bag moulded, sintered, length of bar is 100 μm

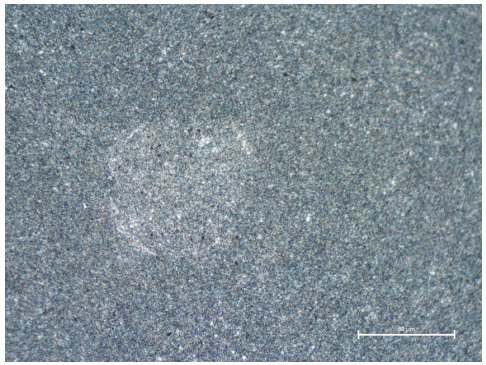

(e) Y, dry-bag moulded, sHIP, length of bar is 50 μm

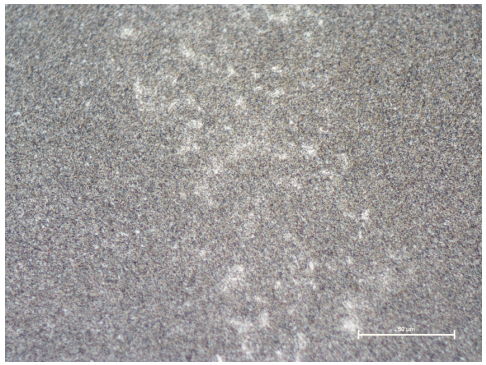

(f) Y, dry-bag moulded, HIP, length of bar is 50 μm

Figure 3.11: Characteristics of dry-bag moulded X and Y

(a) X, direct moulded, sintered, length of bar is 500 μm

(b) X, direct moulded, sHIP, length of bar is 50 μm

(c) X, direct moulded, HIP, length of bar is 500 μm

(d) Y, dry-bag moulded, sintered, length of bar is 500 μm

(e) Y, dry-bag moulded, sHIP, length of bar is 500 μm

(f) Y, dry-bag moulded, HIP, length of bar is 500 μm

Figure 3.12: Characteristics of direct moulded X and Y

The production thresholds for the physical properties are displayed in table 3.4. The physical properties of the investigated samples are displayed in table 3.5.

	HC	**Dichte ρ**	**$4\pi\sigma$**	**HV**
X	240 ± 25	14.5 ± 0.05	175 ± 10	1590 ± 50
Y	420 ± 30	14.55 ± 0.05	130 ± 15	1930 ± 25

Table 3.4: Thresholds for physical properties

	HC	**Dichte ρ**	**$4\pi\sigma$**	**HV**
X S S	**267**	**14,44**	181	1587
X S SH	**291**	14,48	**151**	1608
Y S S	**378**	14,56	**146**	**1833**
Y S SH	435	**14,61**	119	
Y S NV	**379**	14,58	145	
X DB S	**285**	**14,43**	171	1604
X DB SH	252	14,46	177	1579
Y DB S	415	14,58	138	1923
Y DB SH	427	14,56	138	**1892**
X D S	**283**	**14,4**	**168**	1600
X D SH	242	14,5	174	1572
Y D S	397	14,51	**146**	**1878**
Y D SH	426	14,59	135	1883

Table 3.5: Physical properties of investigated samples

The mean average values of the porosity of the investigated materials, classified according to manufacturing method are displayed in table 3.6 and figure 3.14.

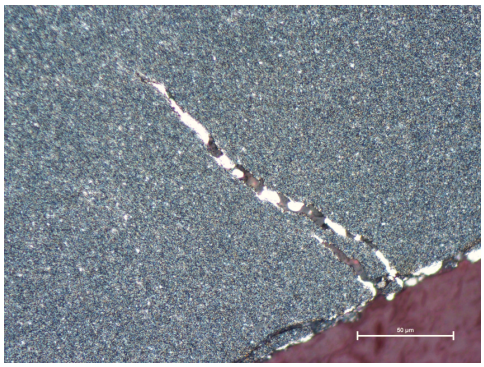

(a) X, direct moulded, sHIP, defect, length of bar is 50 μm

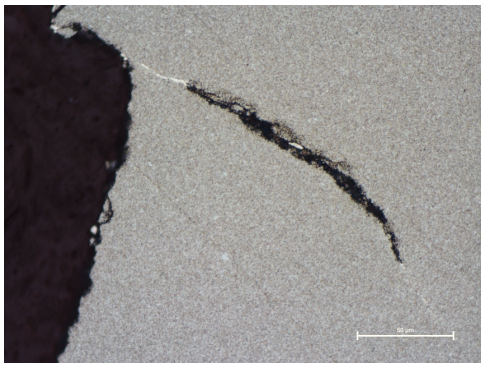

(b) Y, direct moulded, HIP, defect, length of bar is 50 μm

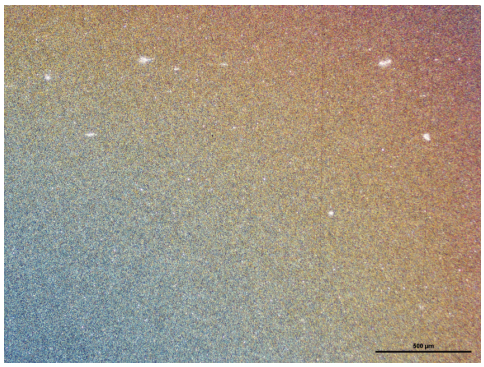

(c) X, extrusion moulded, HIP, longitudinal sample, length of bar is 500 μm

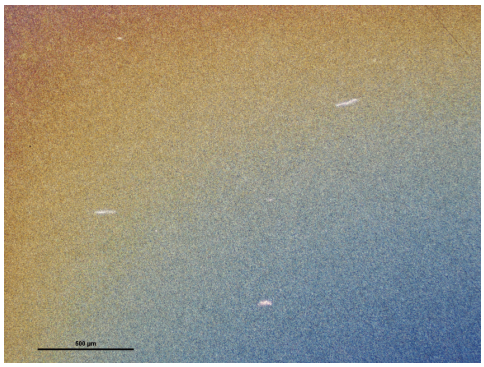

(d) Y, extrusion moulded, sHIP, longitudinal sample, length of bar is 500 μm

Figure 3.13: Various samples

	B-porosity	**25-75 μm**	**75-125 μm**	**>125 μm**
X S S	22	3	1	0
X S SH	0	0	0	0
X S NV	1	0	0	0
Y S S	70	7	2	2
Y S SH	8		0	0
Y S NV	11	0	0	0
X DB S	2	0	0	0
X DB SH	0	0	0	0
X DB NV	0	0	0	0
Y DB S	33	4	0	0
Y DB SH	0	0	0	0
Y DB NV	0	0	0	0
X D S	58	5	0	0
X D SH	1	0	0	0
X D NV	0	0	0	0
Y D S	19	4	0	1
Y D SH	1	0	0	1
Y D NV	0	0	0	2

Table 3.6: Values of porosity classified by raw material and manufacturing method for investigated samples

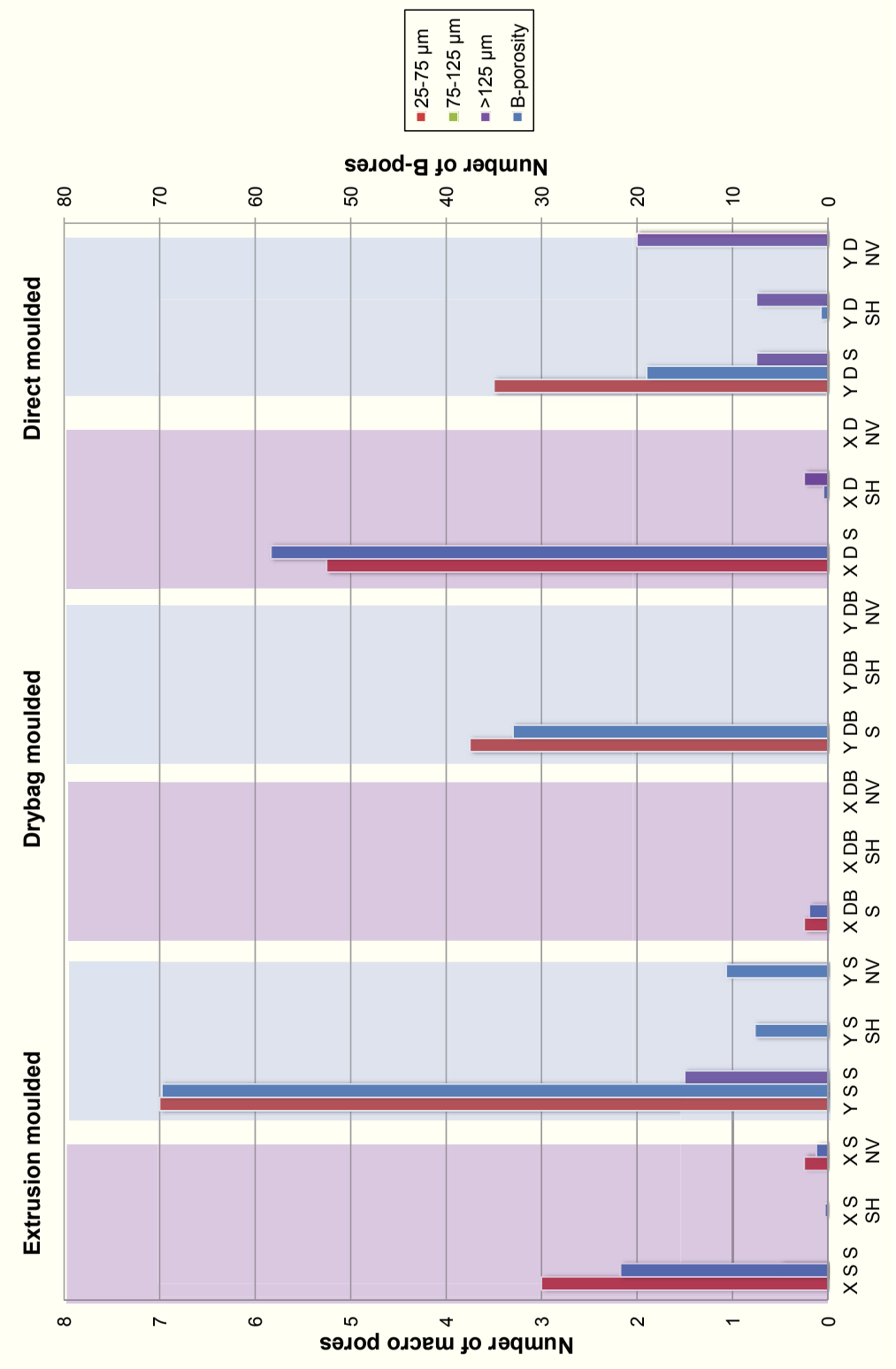

Figure 3.14: Mean average values of porosity classified by raw material and manufacturing method

3.2 Automatic light optical microscope based investigation of porosity

In order to detect pores automatically on a sample surface, based on different shades of grey, a Carl Zeiss M1 microscope with an Axio vision 4 software was set up.
Prior to the actual investigation a panorama-shot, with a magnification of 20, of a representative area of the sample surface was taken (figures 3.15a and 3.15b). The shots were taken monochrome in order to save time during the analytical process. The scale was set to μm in order to obtain the size of the pores also in μm after the analytical process. The starting point of the panorama shot was set, so that the top of the sample would match the center of the first picture taken. The exact knowledge of how the sample was positioned within the panorama shot is important in order to determine the position of the pores later on. The panorama shots were saved as zvi-files in order to enable the automatic analysis.
Due to the different manufacturing methods, different sample areas were chosen, to be representative. For extrusion moulding and dry-bag moulding a thin area along the radius of the sample was analysed, because a change in porosity could only be assumed to occur in a radial direction. In case of direct moulding a change of direction of the applied pressure along the perimeter of the sample was assumed and consequently a quarter of the cross section area was analysed (figure 3.16).

(a) Panorama shot of X extrusion moulded sintered sample

(b) Part of panorama shot of X direct moulded sintered sample

Figure 3.15: Analyzed areas

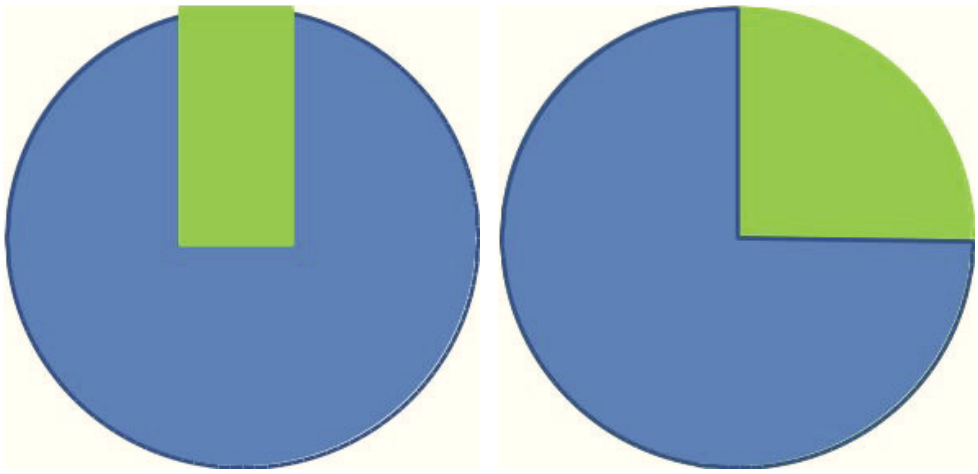

(a) Representative area of extrusion and dry-bag moulded products

(b) Representative area of direct moulded products

Figure 3.16: Analyzed area according to manufacturing method

3.2.1 Configuration of the measuring software

The Axio vision software offers an assistant to configure the measuring routine. Before starting the configuration a new program needed to be created.
In order to optimize the output, the picture properties brightness, contrast and gamma-correction were set to emphasize the dark spots (pores).
The sigma value describes the amount of random noise. High values blur the picture. Accordingly the sigma-filter was set to zero in order to receive sharp, unblured structures.
The shading correction evens out differences in brightness within the picture by creating a subtle colour gradient throughout the picture. This gets in the way of the program recognizing different shades of grey at the edge of a pore and needs to be turned off.
For the edges to be recognized ideally the minimum grey shade difference was set to 235. A lower difference in grey value would not be recognized as an edge between matrix and pore. The area within which this minimum grey shade difference needs to occur was set to 4 pixel. These values were determined empirically.
To define the area, that is to be recognized as pore, one pixel with distinctive grey value was chosen. Due to varying grey shades within a pore, the tolerance for the grey value was set to 1, which proved to be selective enough, to prevent the whole sample surface to be marked as pore. If not all of the dark area was marked, a different pixel, with a different grey shade was selected. To limit the amount of pixel, that need to be selected in order to cover all the grey shades present within all the pores on the sample surface, the size of the area, to be considered around the pixel was set to 2. This describes the the edge length of the matrix around the selected pixel, within which, the grey values are considered. The set tolerance is then added to all the grey shades present in the matrix.
To edit the automatically marked areas, the following options were used to achieve an optimal output. The size of the pores, included in the final report, was set to 10 to 32000 pixels. This equates to areas from 5 μm to 17204 μm. 32000 pixels is the maximum value, that can be configured. Objects which were marked as pores, but were clearly artefacts such as scratches on the surface, dirt, dust, alcohol stains, hair, etc. that would also appear dark in the picture, were deleted one by one. Areas, not marked as pore within an area marked as pore, were filled by using the option to fill areas. This option fills areas, surrounded by an area, that fulfils the grey-shade criteria to be marked as a pore.
Touching objects can be united manually if they actually represent one pore. By using the option to separate touching objects according to the water divide principal, where objects are separated due to edges in the background, longer objects are likely to be divided into smaller ones.
In order to quantify the porosity the parameters, described below, were chosen to be displayed in the output file: Name of analysed picture, area of marked object, maximal diameter of marked object, perimeter of marked object, x-position of marked object and y-position of marked object (figure 3.17).

3.2.2 Analysis of output

The pores were sorted according to their area and pores $< 10\ \mu m^2$ were discarded. In order to display the distribution of the remaining pores graphically, their position

(a) Area

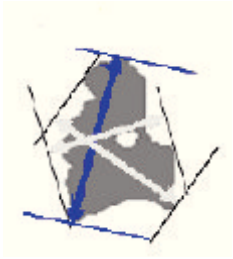

(b) Diameter

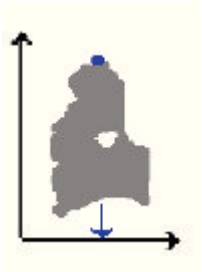

(c) X-position of pore

(d) Y-position of pore

Figure 3.17: Parameters of marked objects [11]

was to be determined. The AcpX and AcpY values were converted into μm using the factor 0.537632466, put out by the microscope. Since the origin of the sample was placed in the center of the first picture taken, the converted y-position was subtracted by 260.215 μm, which equals half the height of an individual picture. The origin of the x-y coordinate system is now precisely at the top of the sample.

Figure 3.18 and 3.19 display the distribution of the pores on the surface of X extrusion moulded and a Y dry-bag moulded sample respectively. Both figures show accumulations of marked areas, close to the edge of the sample. Figure 3.18 displays marked areas aligned straightly, whereas figure 3.19 indicates two accumulations of tagged areas. These observations will be discussed in chapter 4. Further results can be found in the appendix.

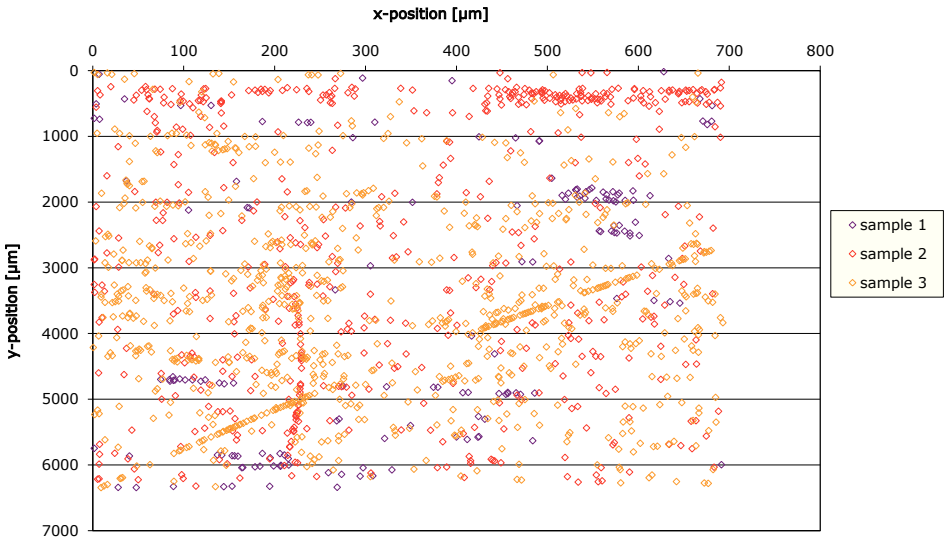

Figure 3.18: Positions of detected pores in X extrusion moulded, sintered samples

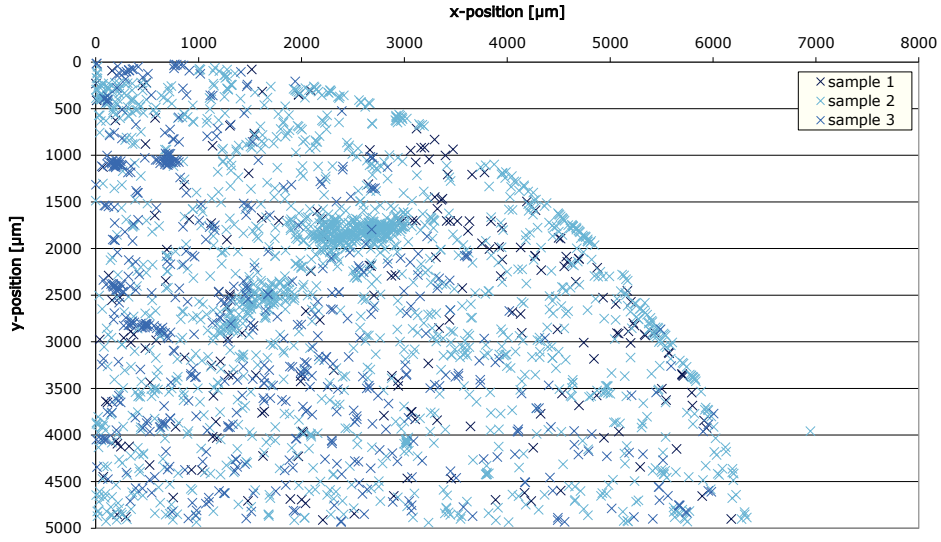

Figure 3.19: Positions of detected pores in Y direct moulded, sintered samples

3.2.3 Validation of results

In order to validate the results found via automatic investigation, samples were prepared at Ceratizit Austria and metallographically investigated by two different people. Those exact samples were then analysed using the automatic investigation. The result of the automatic investigation is displayed in figures 3.20 and 3.21. The comparison between the number of pores found by the two different people and the automatic investigation is displayed in figure 3.22.

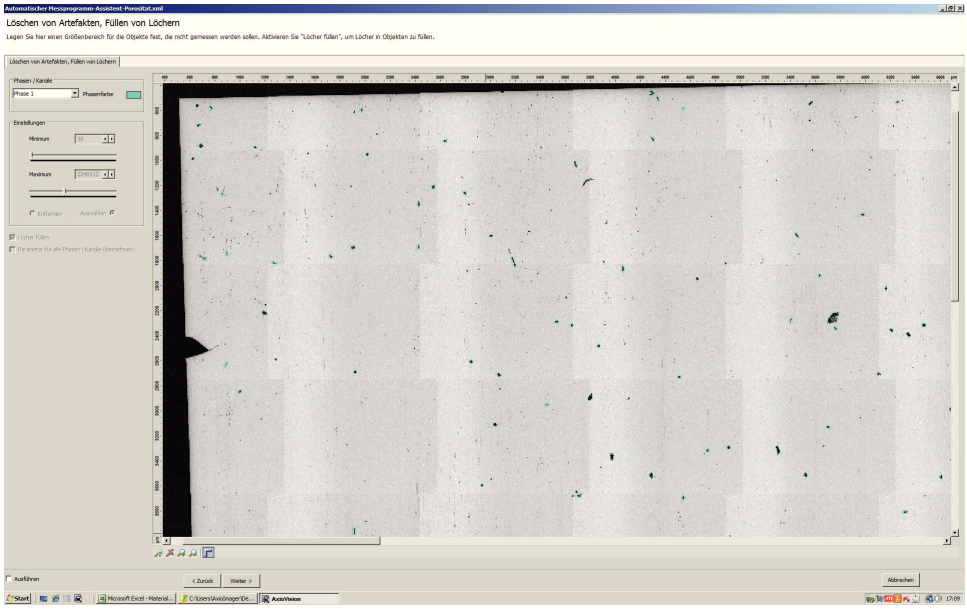

Figure 3.20: Results of the automatic investigation of sample 1

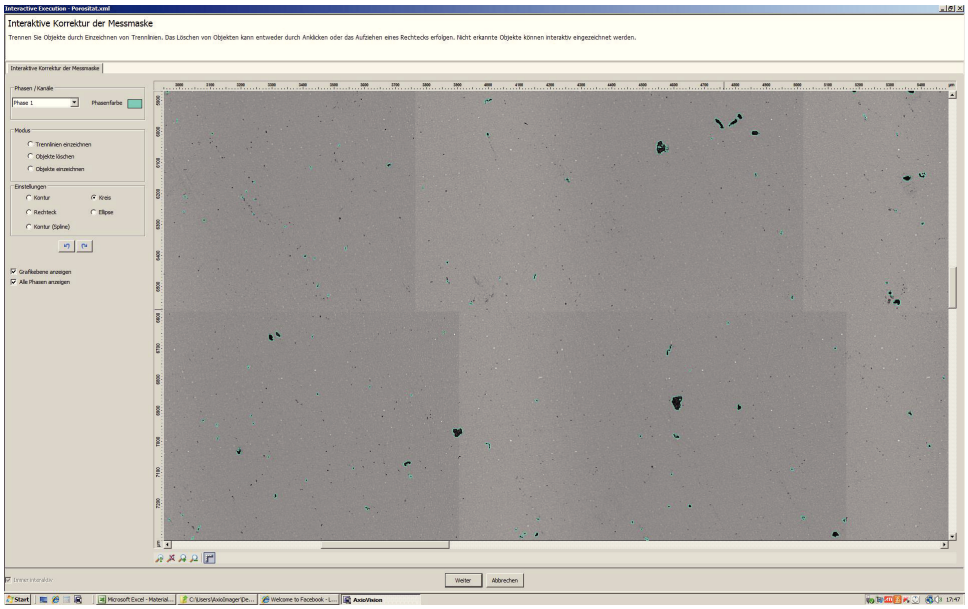

Figure 3.21: Results of the automatic investigation of sample 2

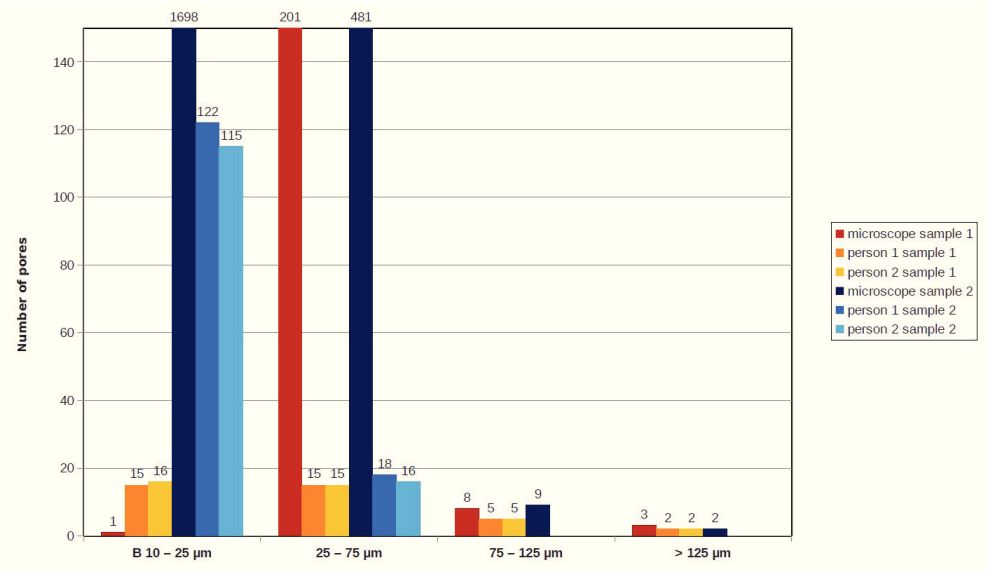

Figure 3.22: Comparision between metallographic and automatic investigation

3.3 SEM and SEM-EDX investigations

SEM was tried out to detect pores with diameters larger than 20 μm. The magnification needed, however resulted in a very small display window. It would take a very long time to scan the sample surface and is therefore not a suitable method for the quality assurance of the production.

Three of the extrusion moulded samples, investigated through metallography showed pores, even after being treated with sHIP or HIP. Three pores per sample were investigated via SEM-EDX. Pictures of the pores analysed, as well as the resulting spectrum can be found in the appendix. Al_2O_3, MgO and SiO_2 was found in one of the pores in a X HIP sample.

3.4 Computed tomography investigation

This is a method, that uses x-ray to collect two dimensional data by rotating the x-ray source and detector. The generated data is then merged into a three dimensional model, using software. The two dimensional x-ray pictures result from a reduction of the X-ray beams either due to absorption by the x-rayed material or due to extinction by a higher material thickness. [12]

The described non destructive investigation technology was used to analyse a presintered X sample, that was shaped into a cylinder with a 3 mm diameter. The result was a three dimensional model of the sample. Figure 3.23 displays a few cuts along the axis of the cylinder. The samples appear homogeneous and seemingly pore-free. However a presintered sample is highly unlikely to be pore-free. The resolution of the method is not high enough, to detect pores, filled with air, homogeneously distributed throughout the sample.

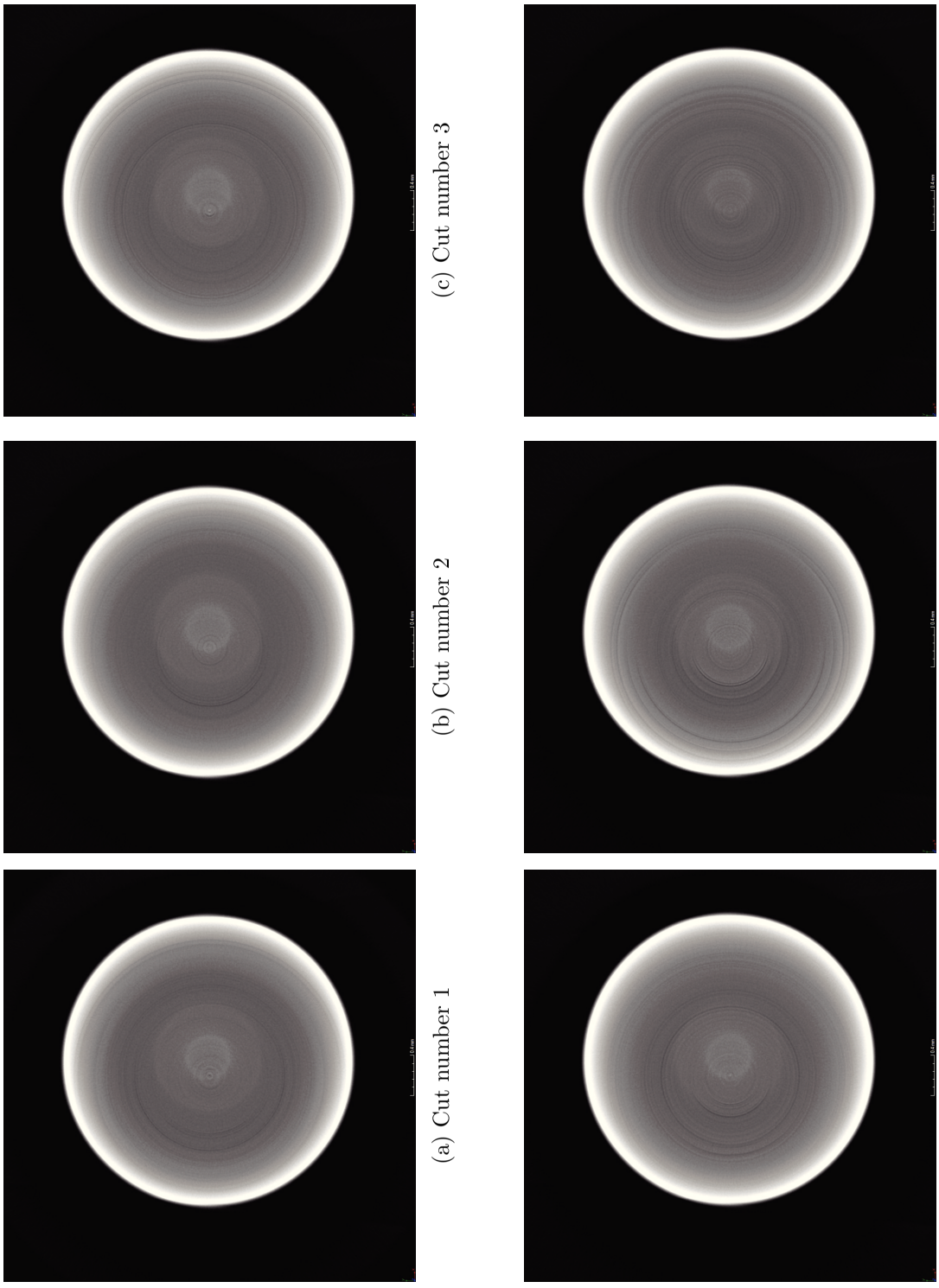

(a) Cut number 1 (b) Cut number 2 (c) Cut number 3

(d) Cut number 4 (e) Cut number 5 (f) Cut number 6

Figure 3.23: Cuts through a 3D model of a X presintered sample

3.5 BET analysis

There are different adsorption isotherms, that describe the equilibrium of adsorption and desorption at a certain temperature. They postulate the amount of matter adsorbed to a surface, as a function of the amount of matter dissolved in the gas-phase. The Langmuir-isotherm is an adsorption model, that only takes a monomolecular layer into account. In order to determine the specific surface of a substance, the BET-model was developed, which takes into account the adsorption of multimolecular layers. [13]

Our samples were exposed to nitrogen. The amount of gas adsorbed depends on the exposed surface, the temperature, the gas pressure and the strength of the interaction between gas and solid. Higher specific surface indicates higher porosity. However the method only detects pores, connected to the surface. [13]

The detected pores were in the nano size range, which means that the method measures the specific surface. However it seems unsuitable for the measurement of pores exceeding 20 μm in diameter. Results are displayed in the appendix.

4 Discussion and Summary

4.1 Metallographic investigation

The metallographic investigation of the extrusion moulded X and Y samples showed, that the porosity declines from pre-sintered to sintered state and tends to go towards zero after the pressure treatments.

4.1.1 Extrusion moulding

Starting with the presintered samples, representing the raw material after the moulding process the most noticeable difference between X and Y is the much coarser structure of the surface in X samples (figure 3.6). Interesting seems to be the localized porosity visible in figures 3.6a and 3.6c, which could be due to an inhomogeneous distribution of the plastifier, possibly combined with a demixing of the mass because of the formation of the holes in the middle of the sample. A higher compression zone along the perimeter of the X samples is due to the friction between the material and the mould during the moulding process, causing the material to strongly deform locally. These compressed zones appear to even out during the sintering and pressure treatment process. In Y samples a clearly visible zone close to the edge can be seen (figure 3.6d). The bright zone is most likely oxidized material, which can cause flaking during the sintering process. During the presintering process under reducing atmosphere, the sample was probably partly recarbonized, which is why the oxidized area does not touch the edge of the sample. The pores displayed in figures 3.6c and 3.6f are the biggest, that were found in all three extrusion moulded samples investigated.
According to theory, powders with smaller grain size, also have a smaller grain size distribution and because of that do not pack well together. As a consequence an excess of plastifier is needed to fill the extra voids. During the sintering process, the plastifier evaporates, leaving pores. This is the case for the tested material Y. It shows a higher porosity than the X material after sintering, due to the smaller grain size of the Y material (figure 3.3). The B-pores in two Y samples, after different pressure treatments (sHIP and HIP) could have arisen out of an inhomogeneous plastifier-distribution within the material.

Most of the detected B-pores within the sintered, extrusion moulded material, were converted into Co-accumulations with fine, embedded WC grains during the pressure treatment. The sintered X samples demonstrate rather big Co-phased areas, accompanying the pores. Those are transformed into homogeneous material during the pressure treatment. Looking at figure 3.9 it can be seen, that in at least one case, the pressure applied by the sinter HIP method wasn't enough to close the pore completely, leaving an Co-accumulation and an A-pore in the center of it. One HIP

treated sample showed B-porosity as well as macro-porosity. It was investigated with SEM-EDX and one pore containing Al_2O_3, MgO and SiO_2 was found. These materials could come from recycling coated material, or the refractory lining of the carbonizing oven or from the Al_2O_3 mats in the recycling process, used to seal the container. The other pores, investigated showed no foreign materials.

An inhomogeneous plastifier distribution during the moulding process can create big pores, which cannot be filled during HIP treatment. Samples taken in an longitudinal direction show stretched pores, which signify a bigger hazard to the mechanical properties (figures 3.13c and 3.13d). It needs to be kept in mind, that samples taken in a radial direction show round and smaller pores, but due to the manufacturing process, those pores appear longer and bigger, when looking at samples taken from the axial direction.

Both materials show pores, in individual samples after both pressure treatments, so it appears the common factor is the manufacturing method. Extrusion moulded material contains a higher amount of plastifier, than dry-bag or direct moulded material. It is furthermore necessary to plastify the material again, right before moulding, which represents an additional source of inhomogeneous distribution of the plastifier, whereas dry-bag and direct powder are ready to press, so there is no need for an additional plastification step. Also extrusion moulding requires 8 % of plastifier, whereas with dry-bag and direct moulding only 2 % of plastifier is used.

4.1.2 Dry-bag moulding

The presintered samples show a coarser surface in the X samples. The porosity in Y samples has a more crack like structure which is possibly due to the fact, that the granulates were not pressed properly. If one would draw a circle around the crack in figure 3.7f in would be around 150 μm, which equals the size of the granulates. Dry bag moulding shows perfect results for both X and Y, displaying zero pores after sinter HIP and HIP pressure treatment. X samples show rather big WC grains up to 13 μm, which can be considered the biggest defect of the otherwise very homogeneous material. The higher A-porosity in Y sintered samples is due to the finer grain size and the smaller grain size distribution of the Y material, as explained above. Noticeable are the granulates, which were not smashed during the milling or moulding process and are still visible in the sintered and pressure treated samples. These granulates are filled with Co after the sintering process. The Co-phases are replaced by a homogeneous structure during both sinter HIP and HIP pressure treatment. The remaining Co-phases after the pressure treatments between the WC-grains are not big enough to be classified or to cause any type problem with the mechanical properties.

4.1.3 Direct moulding

The surface of the Y presintered samples is much smoother compared to the X samples. The bright zone in figure 3.8c might be oxidized material, from when the door of the sintering oven is opened. Freshly sintered samples tend to heat up due to oxidation, when the door of the reducing sintering oven is opened. Products are frequently tested for oxygen content and the distribution is homogeneous (0.2 - 0.25 %

oxygen) within the material, so this theory is unlikely. Alternatively the zone could be an effect of the heat during the embedding of the sample. This seems quite likely because the zone follows the outline of a crack, connected to the surface. The big crack in figure 3.8f can be attributed, due to it's position, right on the edge between the pressing bar and the actual sample, to the usage of the wrong pressing tools. After applying the pressure, the tool needs to be removed with a certain speed, in order to not damage the product while it decompresses. This is a well known fact to the production and rarely a problem. Most likely the same tools were mistakenly used for making the X and the Y samples. Also one of the X sample shows one of the described cracks, which can also be attributed to problems during the moulding process. 30 μm of the material are cut away on each side, not including the excess material due to the manufacturing process. In the case of the cracks described, this would not be enough to eliminate them.

The most noticeable pores are the macro-pores > 125 μm also presenting in the Y sHIP and HIP samples. The described Co-phases are to be found within the cracks. Apart from the cracks described, the material is very homogeneous. The effect of the lower grain size and grain size distribution of the Y on the porosity in sintered material appears to be reversed in the case of direct moulded material, as the B-porosity is lower in the Y samples. One of the X sintered samples show a HC-value, that is out of range. HC- values can only be interpreted together with $4\pi\sigma$-values and the density. Figure 4.1 shows that HC alone can be low due to under-, and over-sintering. In the case of our X sample the $4\pi\sigma$-value as well as the density is low, so that under-sintering seems likely.

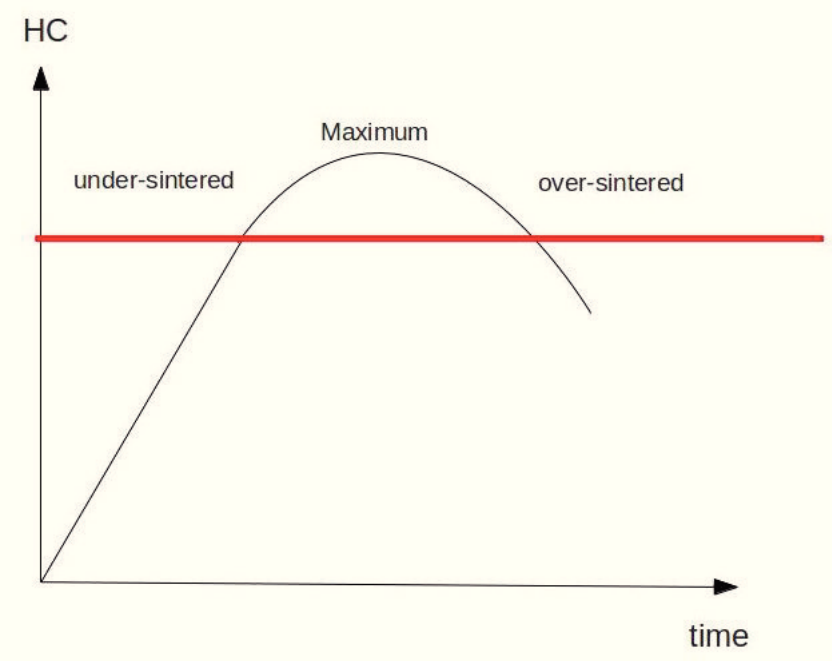

Figure 4.1: Developement of HC during the sintering time

Summing up, it can be said, that the porosity is higher in Y samples after sintering manufactured by extrusion and dry-bag moulding, even though the porosity is

higher in X presintered samples, than in Y presintered samples throughout the manufacturing methods. The reason for this is the smaller grain size of the Y material, which equals a higher specific surface. Smaller WC grain size means smaller grain size distribution, which results in the grains not packing well together and more small pores between the grains. Due to this, more rearrangement of the material structure and more shrinkage during the sintering process is necessary, in order to fill the voids. This can lead to a higher porosity especially if the structure rearranges itself aiming to reduce the specific surface. Shrinkage in X is 22 % and 25 % in Y. The hardness values of the presintered samples show significantly higher values for Y samples, which matches the subjective impression of the Y samples having a denser surface. A differentiation between the manufacturing methods based on hardness values doesn't seem feasible, due to the similar values for each of them.
Extrusion moulded samples show higher porosity than the the samples of other manufacturing methods. Y extrusion moulded samples show higher porosity than X extrusion moulded samples in every investigated state. Surprising is the higher amount of B-pores in Y and X extrusion moulded HIP samples than in Y and X sHIP samples, even though HIP operates with a much higher pressure.

Dry-bag moulding seems to be the best manufacturing method for both materials.

Discarding the pores due to wrongly used moulding tools, direct moulding with sHIP or HIP treatment seems to be working almost flawlessly.

Sinter HIP doesn't seem to cause any kind of disadvantage concerning the porosity in either of the tested materials, despite the lower pressure, compared to HIP.

4.2 Automatic investigation

When looking at figures 5.21, 5.22, 5.26-5.28, 5.33-5.35, 5.40-5.42 and 5.47-5.49 the statistical spread of objects identified is rather high throughout the samples of one material, manufactured a certain way. This is probably due to the fact, that the microscope cannot take the shape of an area with a certain grey shade into account in order to identify it correctly. When doing metallography manually, it is often necessary to change the magnification to a higher one in order to identify an object as pore. Also the presence of a Co-phase close to a dark object is usually an indicator for a dark spot being a pore. To take the panorama shot with a higher magnification in the first place, so that dust and other foreign objects on the sample surface would appear in a lighter shade of grey, doesn't seem to be feasible due to the time that wouldbe required to take the shot and to analyse it thereafter. The time factor is certainly a disadvantage of the method. Depending on the size of the panorama shot each sample takes several hours to analyse.
Figures 5.19, 5.20, 5.23-5.25, 5.30-5.32, 5.37-5.39 and 5.44-5.46 show the distribution of objects detected throughout the fotographed sample surface. Noticeable are a higher density of objects near the edges of the samples as well as a higher density of objects, aligned rather straightly, found in different places on the sample surfaces. The former is probably due to difficulties exposing the edges correctly, with the out of focus area bordering them. The latter are scratches on the surface sample.

Despite the seemingly good accordance of the detected objects with what seems to be a pore (figure 3.20 and 3.21 the validation of the method did not succeed as displayed in figure 3.22. The number of pores counted by two different persons are well compliant, whereas the number of objects detected by the automatic investigation differs.

Summing up it is likely that the process of detecting pores is too prone to falsification due to dirt, alcohol staines, dust, etc. and also too complex to be reduced to different shades of grey.

5 Conclusion and Outlook

The subject of this thesis was initially approached through extensive research of existing literature and patents within the field of cemented carbides. Results specifically dealing with manufacturing methods, material properties and microstructure of the product were chosen to build the theoretical foundation for the conducted experiments.

Two different approaches were taken to determine the influence of raw materials and manufacturing methods on the microstructure of cemented carbide.

The metallographic investigation resulted in clear manufacturing method and pressure treatment preferences in order to minimize porosity for each individual raw material. Future process logistic can consider these results in order to optimize product quality and minimize product rejections due to defects. Investments for new equipment with the highest product quality can be planned specifically according to the demand for a certain raw materials.

The investigation with a software-controlled optic microscope represents an innovative approach to determine the porosity in cemented carbide samples automatically. However due to software limitations the metallographical process is still too complex to enable an automatic approach. The main limitation include analysis-time and the ability to change the magnification automatically during the investigation. These shortcomings are to be overcome by future research in order to make automatic porosity investigation possible.

Bibliography

[1] W. Schedler. *Hartmetall für den Praktiker: Aufbau, Herstellung, Eigenschaften und industrielle Anwendung einer modernen Werkstoffgruppe*. VDI-Verlag, 1988.

[2] T.Klünsner E. Eidenberger, editor. *VO Hartmetalle, Universität Leoben*, 2012.

[3] K. J. Brookes. *Hardmetals and other hardmaterials*. International Carbide Data, East Bartnet, Hertfordshire, 1992.

[4] R. Kiefer. *Hartmetalle*. Springer Verlag, Wien, New York, 1965.

[5] B. Roebuck. Terminology, testing, properties, imaging and models for fine grained hardmetals. *International Journal of Refractory Metals and Hard Materials*, 13:265–279, 1995.

[6] Sandvik. `http://www2.sandvik.com/sandvik/0130/HI/SE03411.nsf/7a5364adb7735b05412568c70034ea1b/4c7827530abfa4e1c1256b0a0034cc36/$FILE/ATTGAHWR/9100%20ger.pdf`. Accessed: 20-march-2012.

[7] B. Animesh. A perspective on the earliest commercial pm metal-ceramic composite: cemented tungsten carbide. *International Journal of Powder Metallurgy*, Volume 47:31–49, 2011.

[8] Wieters K.P. Schatt, W. *Pulvermetallurgie, Technologien und Werkstoffe*. Springer, Berlin, Heidelberg, New York, 2007.

[9] Simma H.P. Schmid L. Barbist, R. Präsentation vom Verfahren zum Produkt.

[10] Bridgwater J. Benbow, J. *Paste Flow and Extrusion*. Oxford series on advanced manufacturing. Clarendon Press, Oxford, 1993.

[11] *Axio imager Helptext, chapter automatic analysing*.

[12] Non destructiver technology research center. `http://www.ndted.org/EducationResources/CommunityCollege/Radiography/AdvancedTechniques/computedtomography.htm`. Accessed: 20-march-2012.

[13] P. Atkins and J. de Paula. Atkins' physical chemistry, 2006.

Abbreviations

BET	Brunauer Emmett Teller
HIP	hot isostatic pressing
NV	hot isostatic pressing
SH	sinter HIP
sHIP	sinter HIP

List of Figures

List of Tables

Appendix

The appendix contains additional results of the investigations conducted:

- **Metallographic investigation**
- **Automatic investigation**
- **SEM and SEM-EDX investigation**
- **BET analysis**

Metallographic investigation

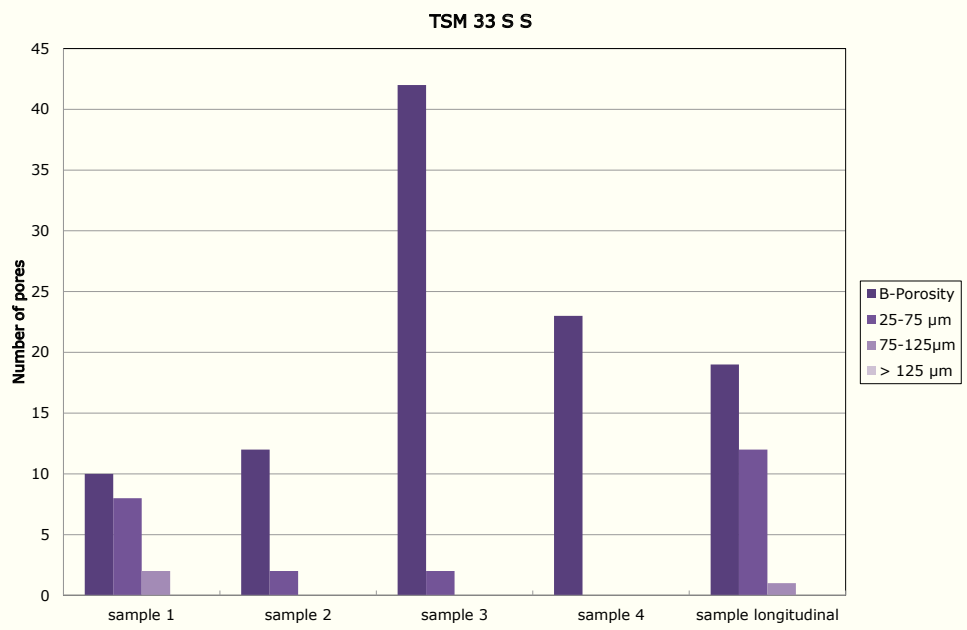

Figure 5.1: TSM 33 S S distribution of pores throughout the samples

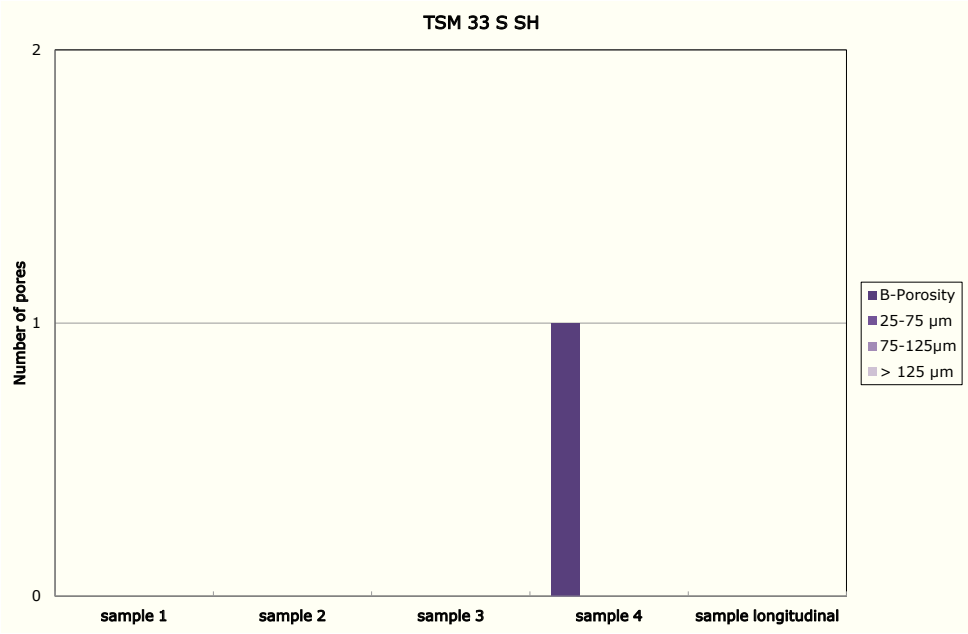

Figure 5.2: TSM 33 S SH distribution of pores throughout the samples

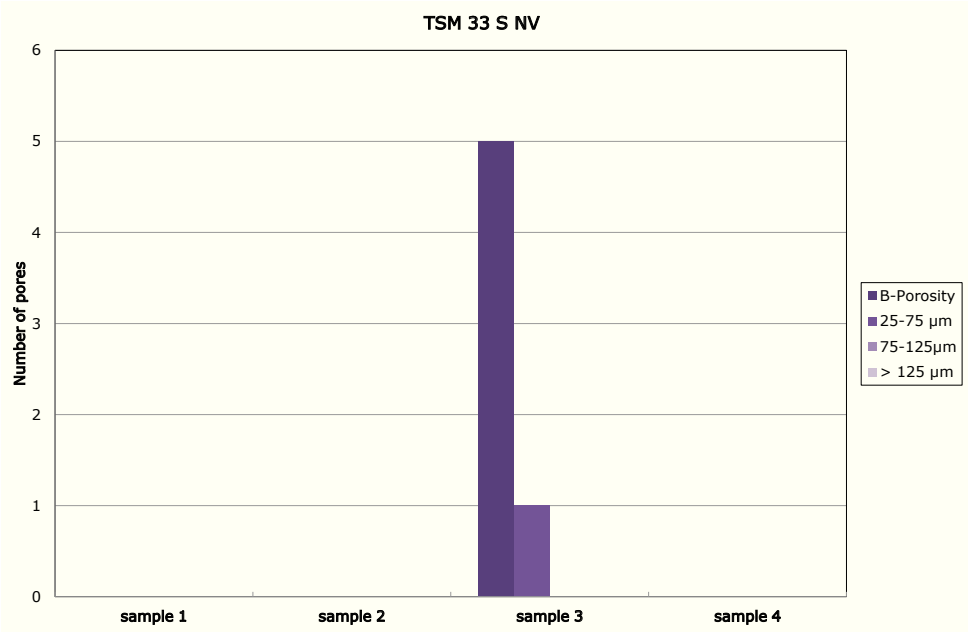

Figure 5.3: TSM 33 S NV distribution of pores throughout the samples

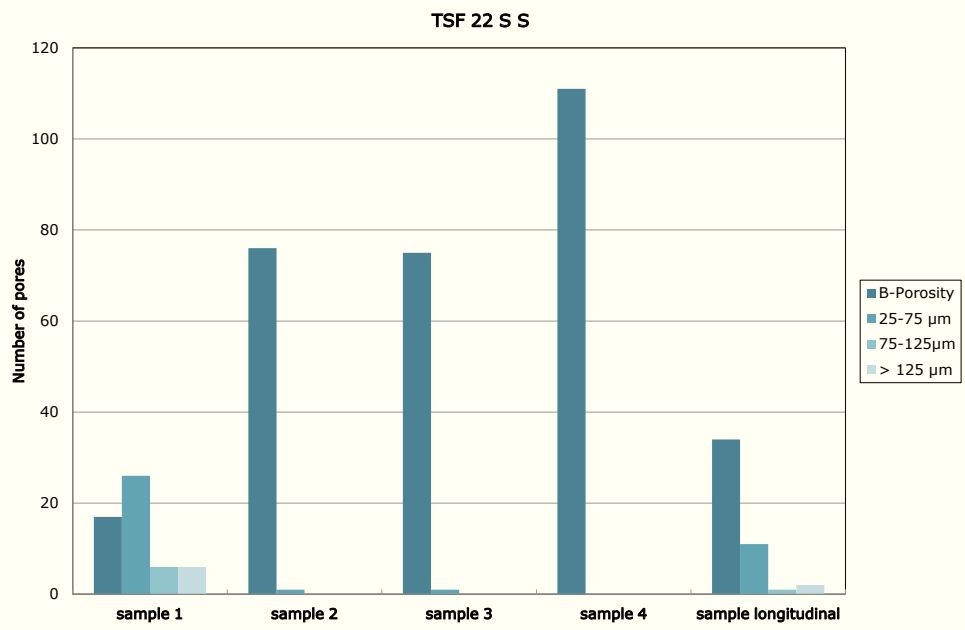

Figure 5.4: TSF 22 S S distribution of pores throughout the samples

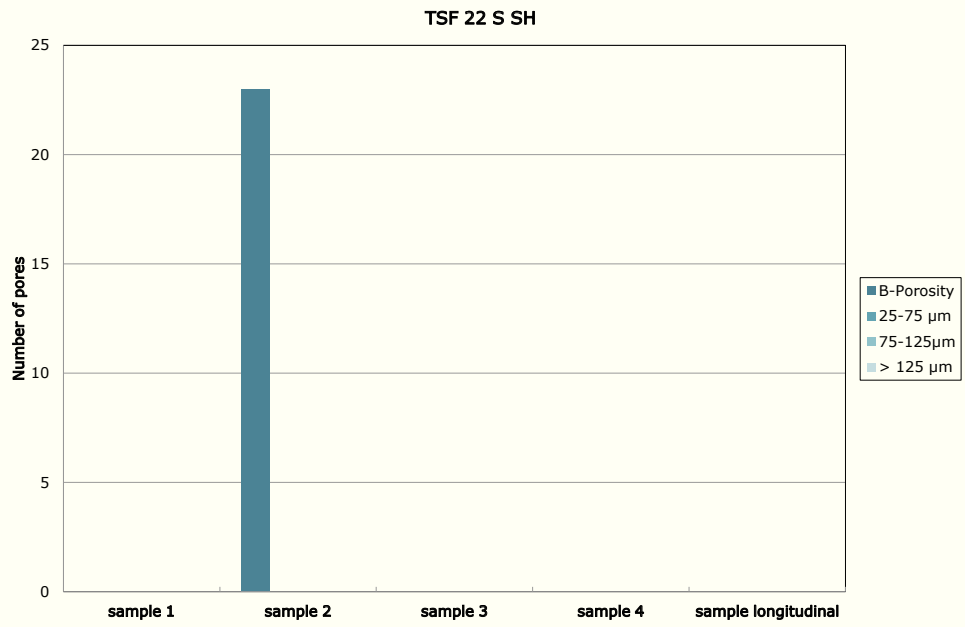

Figure 5.5: TSF 22 S SH distribution of pores throughout the samples

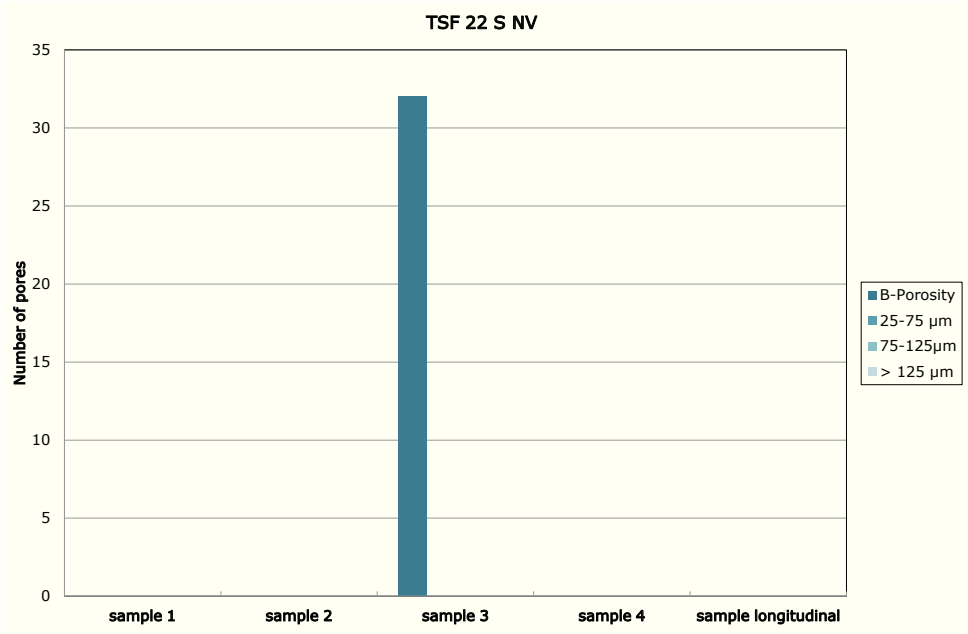

Figure 5.6: TSF 22 S NV distribution of pores throughout the samples

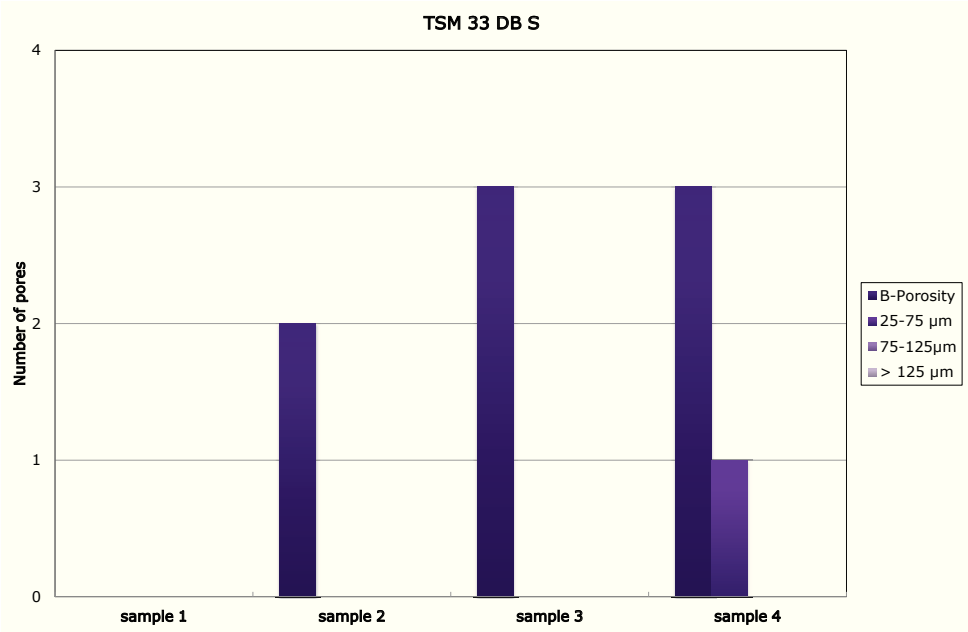

Figure 5.7: TSM 33 DB S distribution of pores throughout the samples

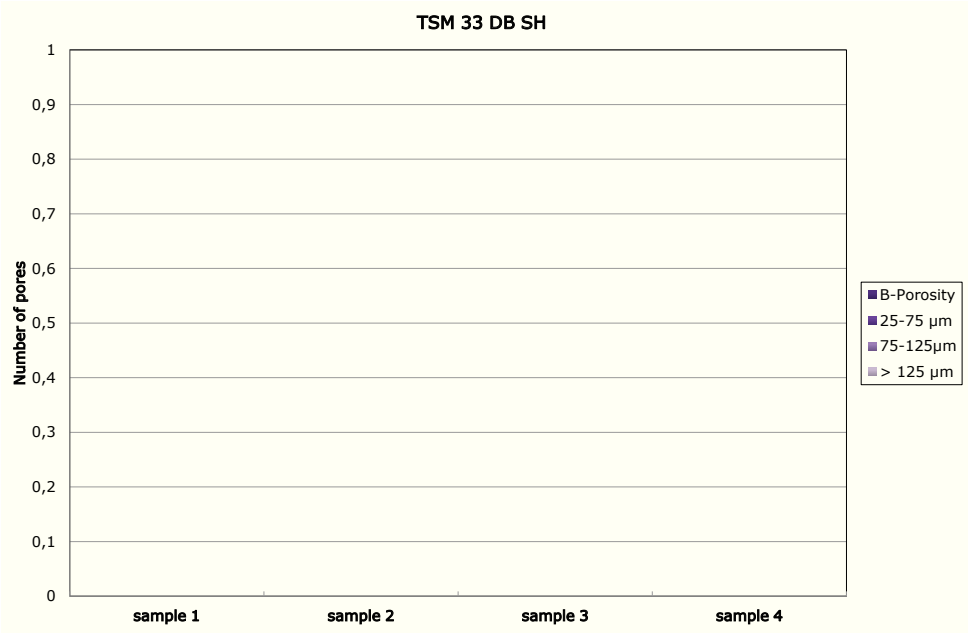

Figure 5.8: TSM 33 DB SH distribution of pores throughout the samples

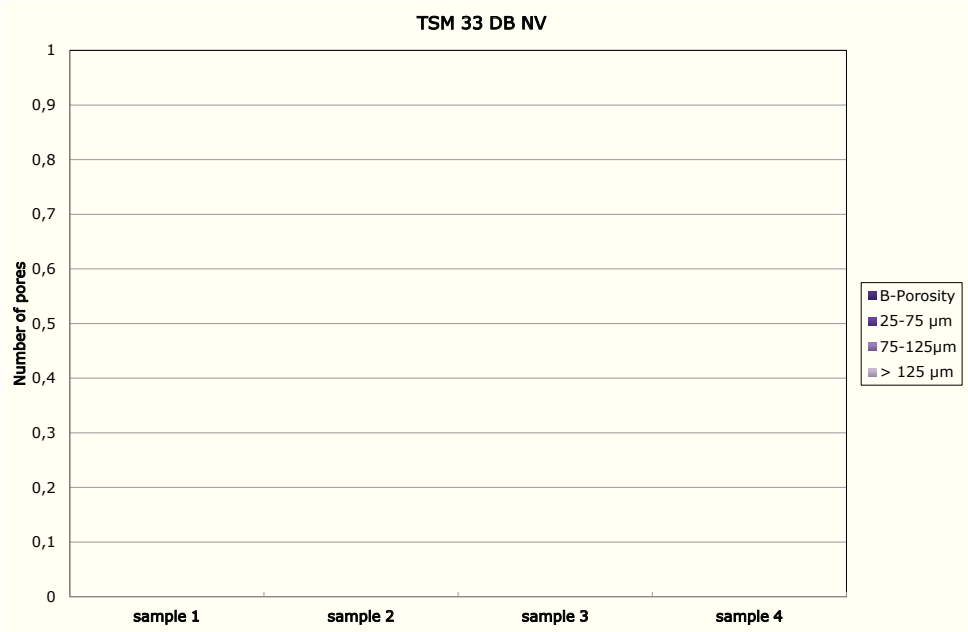

Figure 5.9: TSM 33 DB NV distribution of pores throughout the samples

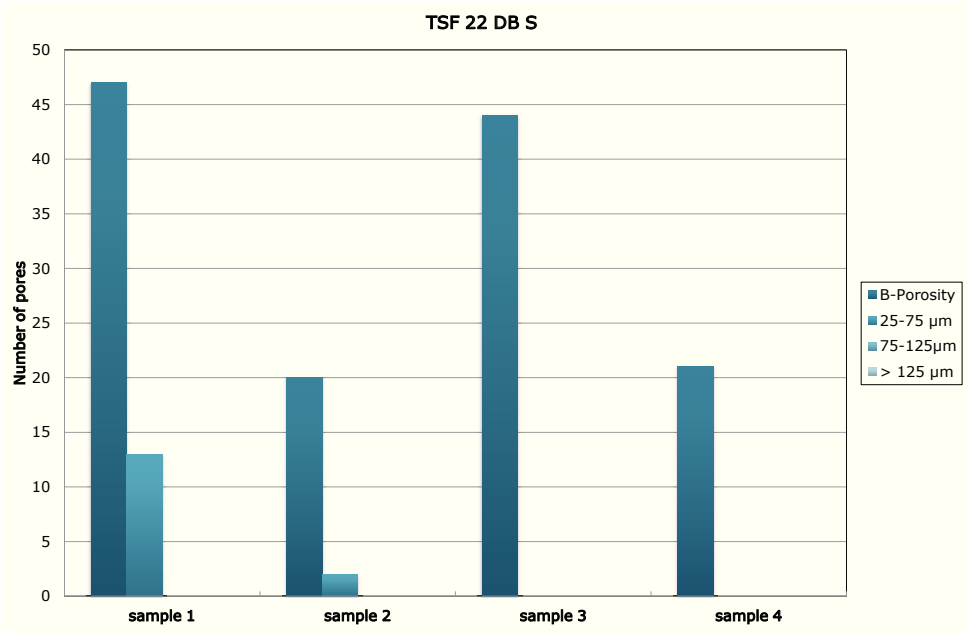

Figure 5.10: TSF 22 DB S distribution of pores throughout the samples

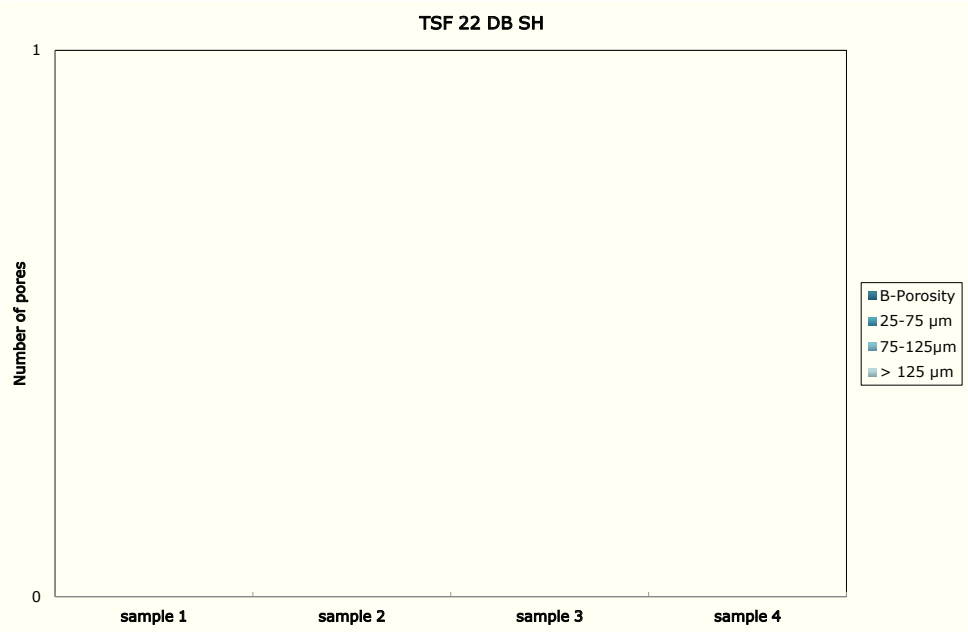

Figure 5.11: TSF 22 DB SH distribution of pores throughout the samples

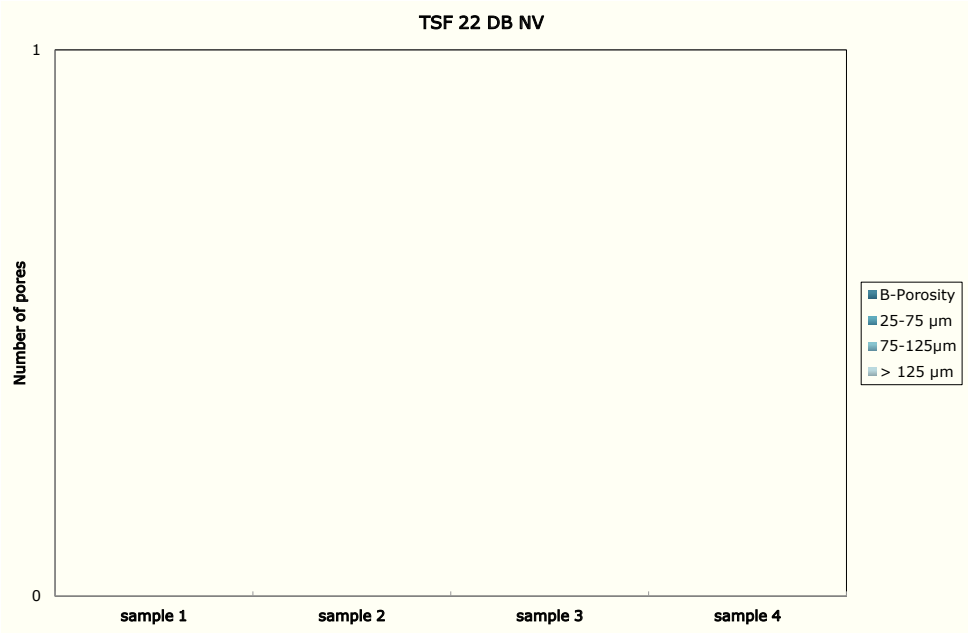

Figure 5.12: TSF 22 DB NV distribution of pores throughout the samples

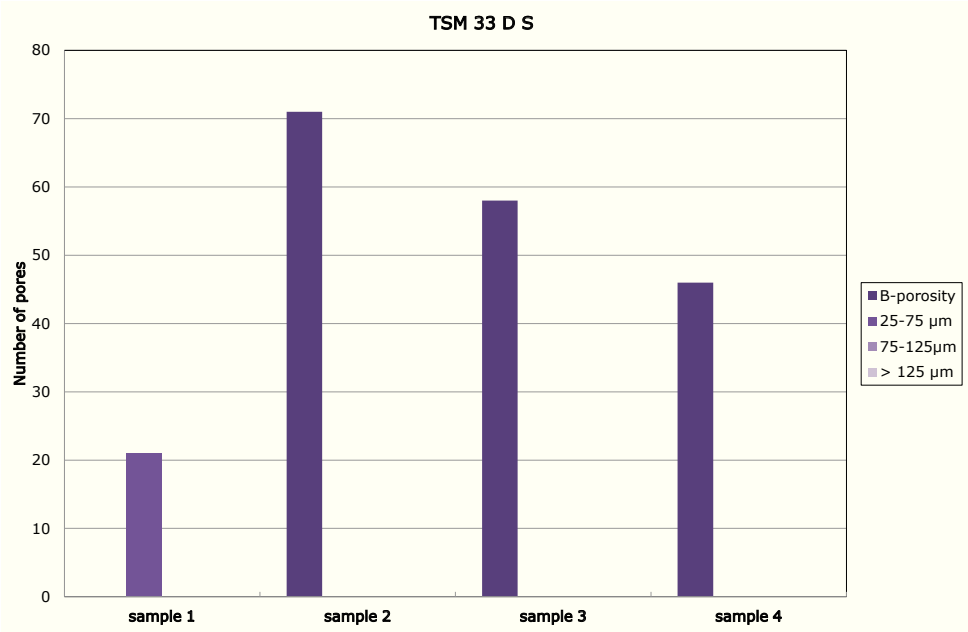

Figure 5.13: TSM 33 D S distribution of pores throughout the samples

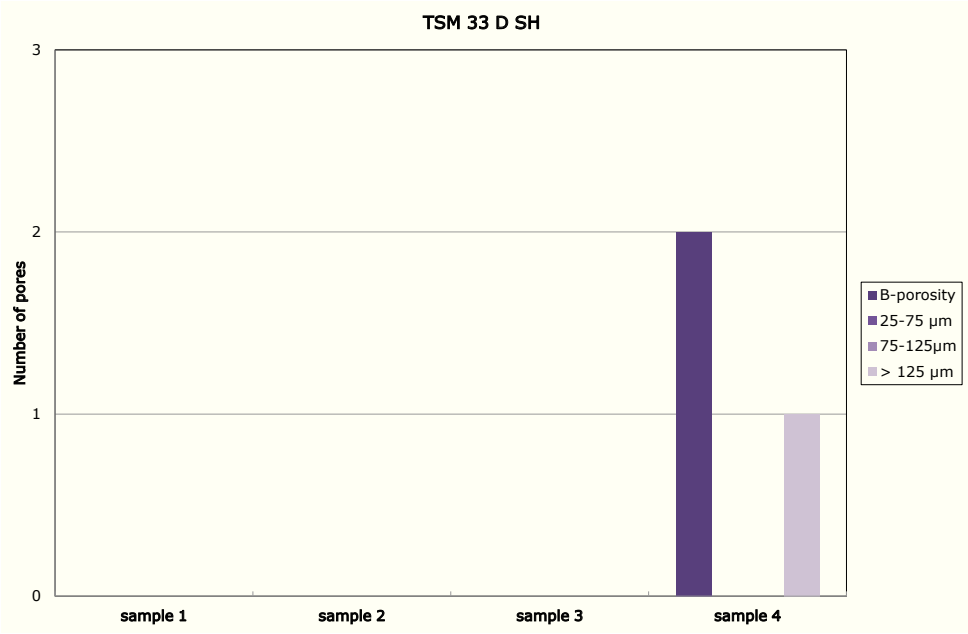

Figure 5.14: TSM 33 D SH distribution of pores throughout the samples

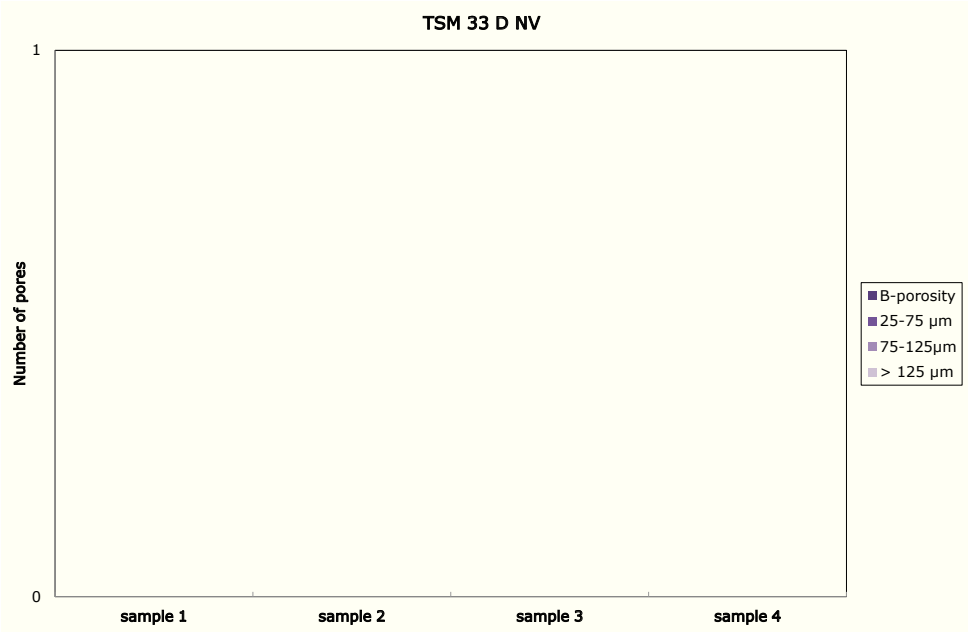

Figure 5.15: TSM 33 D NV distribution of pores throughout the samples

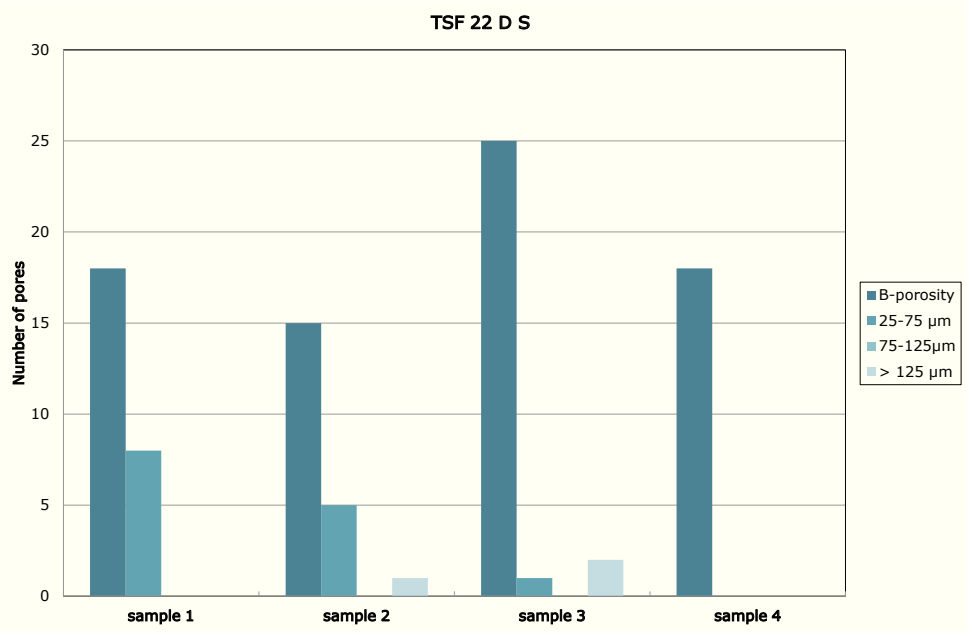

Figure 5.16: TSF 22 D S distribution of pores throughout the samples

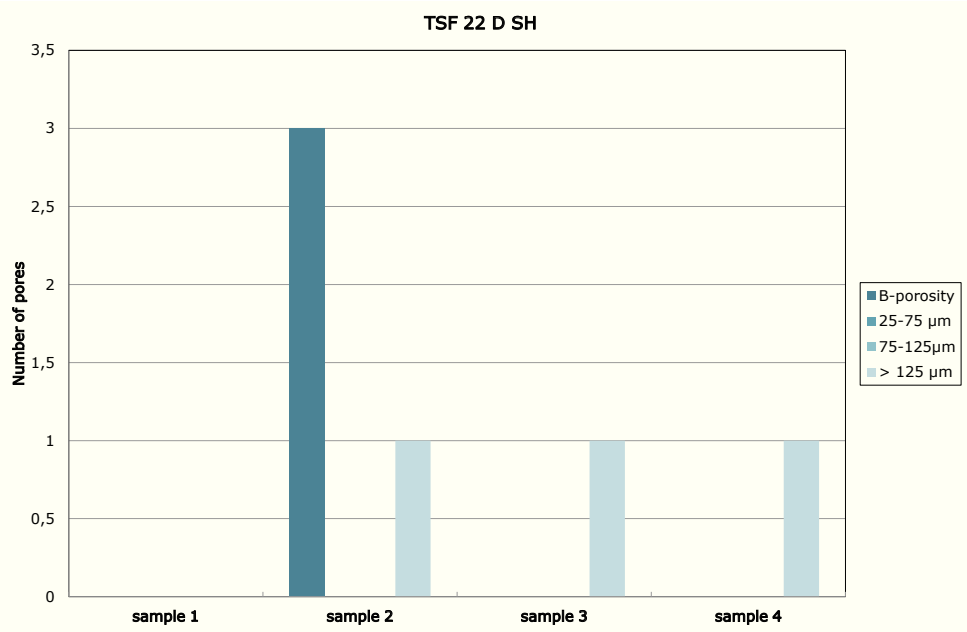

Figure 5.17: TSF 22 D SH distribution of pores throughout the samples

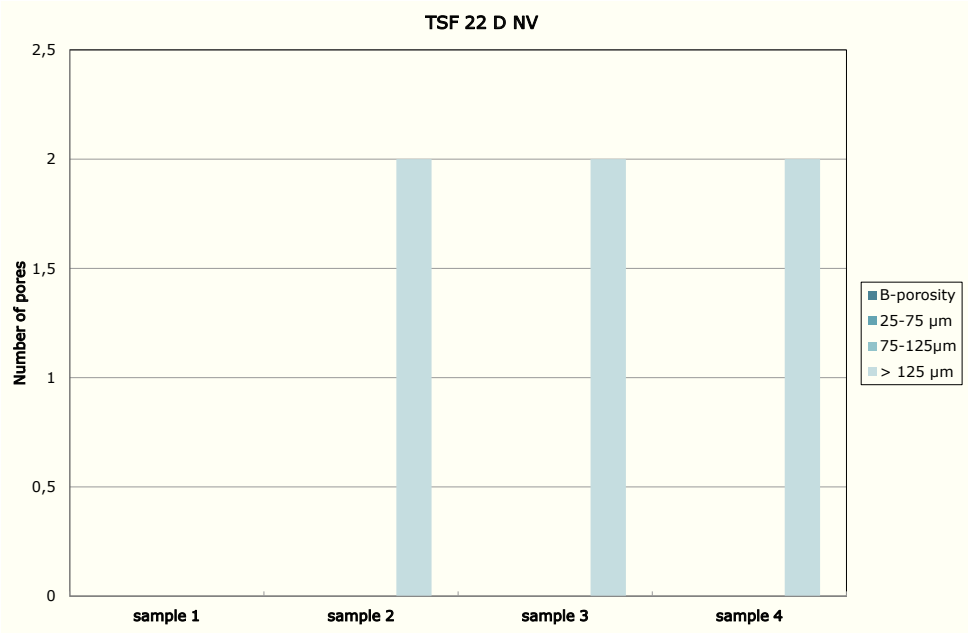

Figure 5.18: TSF 22 D NV distribution of pores throughout the samples

Automatic investigation

Figure 5.19 and 5.20 display the distribution of the pores on the surface of X extrusion moulded samples.

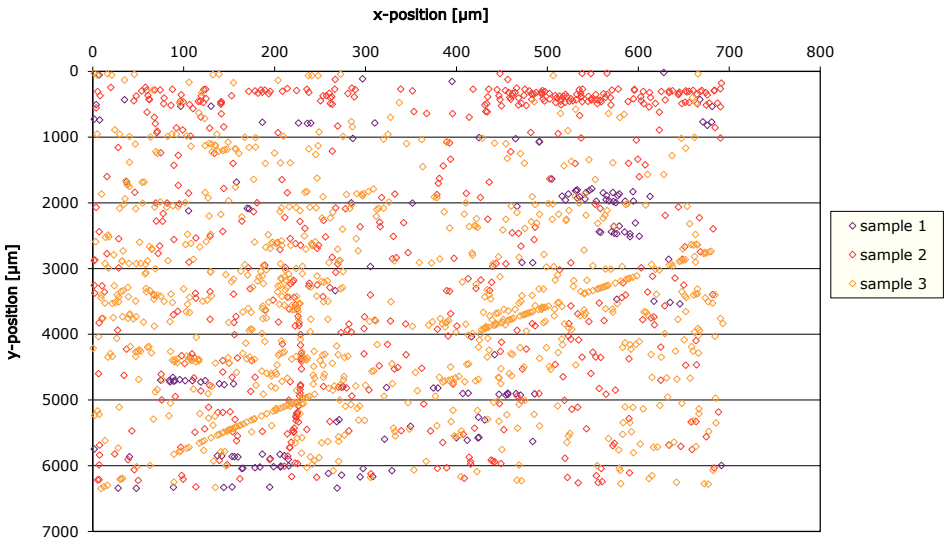

Figure 5.19: Positions of detected pores in X extrusion moulded, sintered

Figures 5.21 and 5.22 exhibit the number of pores on the surface of X extrusion moulded samples.
Figures 5.23, 5.24 and 5.25 indicate the distribution of the pores on the surface of X dry-bag moulded samples.
Figures 5.26, 5.27 and 5.28 display the number of pores on the surface of X dry-bag moulded samples. Figure 5.29 show the average number of pores, occurring after each processing step, classified by pore area in X dry-bag moulded samples.
Figures 5.30, 5.31 and 5.32 exhibit the distribution of the pores on the surface of Y dry-bag moulded samples.

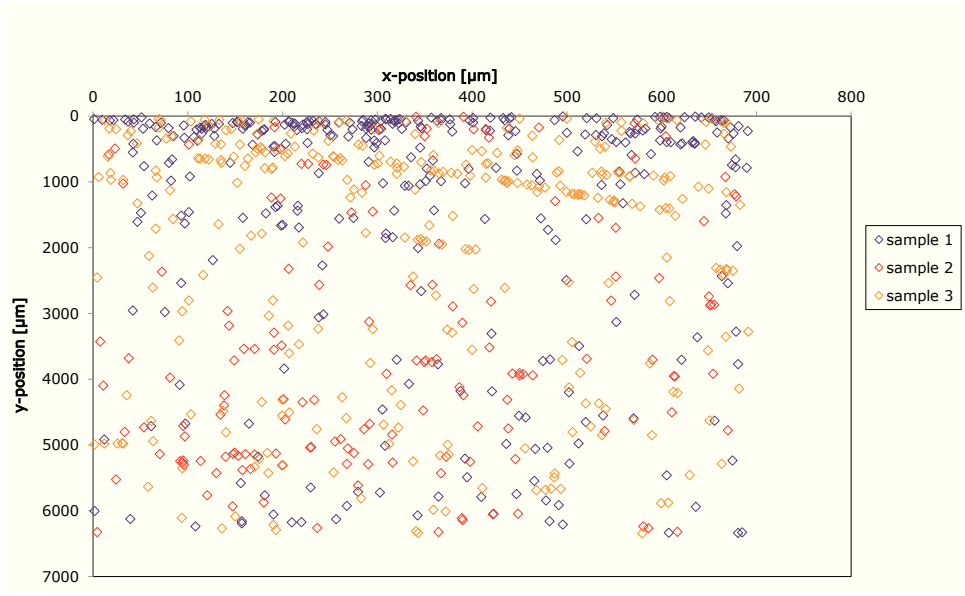

Figure 5.20: Positions of detected pores in X extrusion moulded sHIP

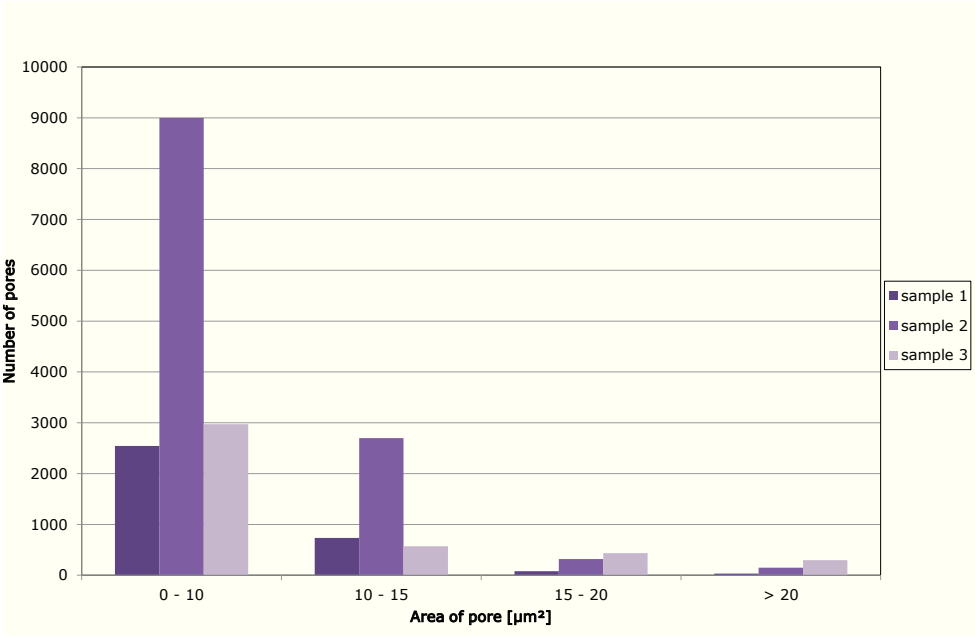

Figure 5.21: Number of pores in samples X extrusion moulded, sintered

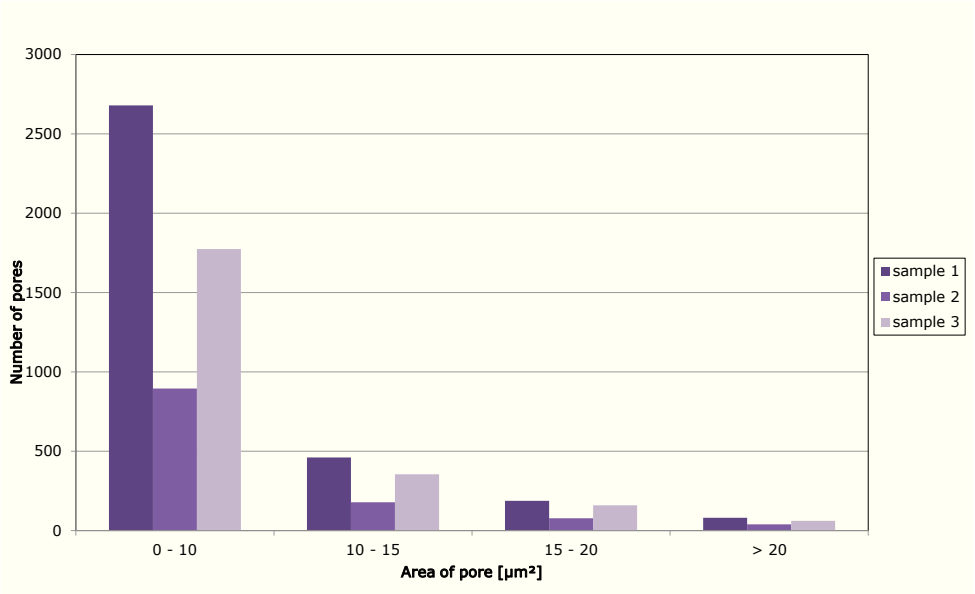

Figure 5.22: Number of pores in samples X extrusion moulded sHIP

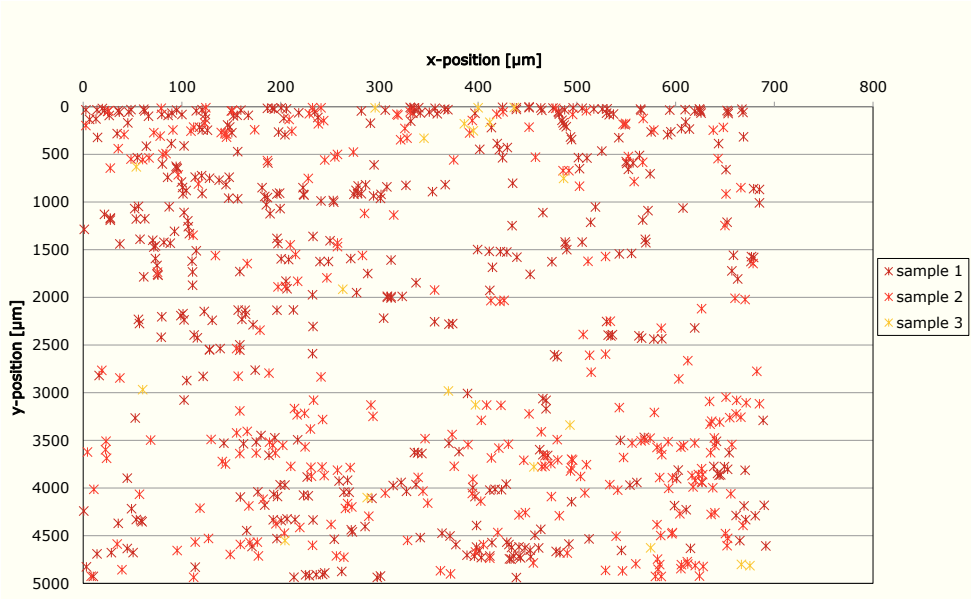

Figure 5.23: Positions of detected pores in X dry-bag moulded, sintered

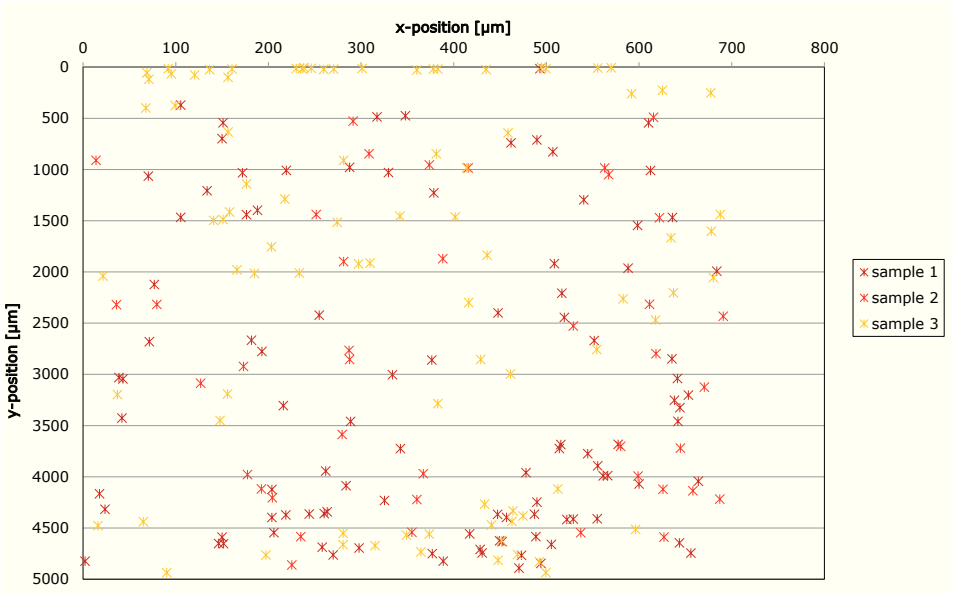

Figure 5.24: Positions of detected pores in X dry-bag moulded sHIP

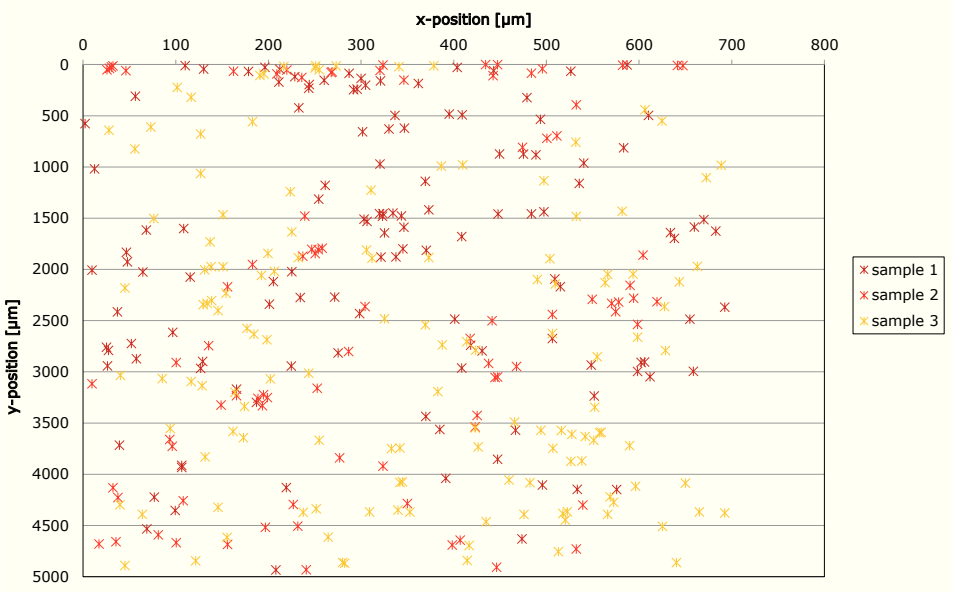

Figure 5.25: Positions of detected pores in X dry-bag moulded HIP

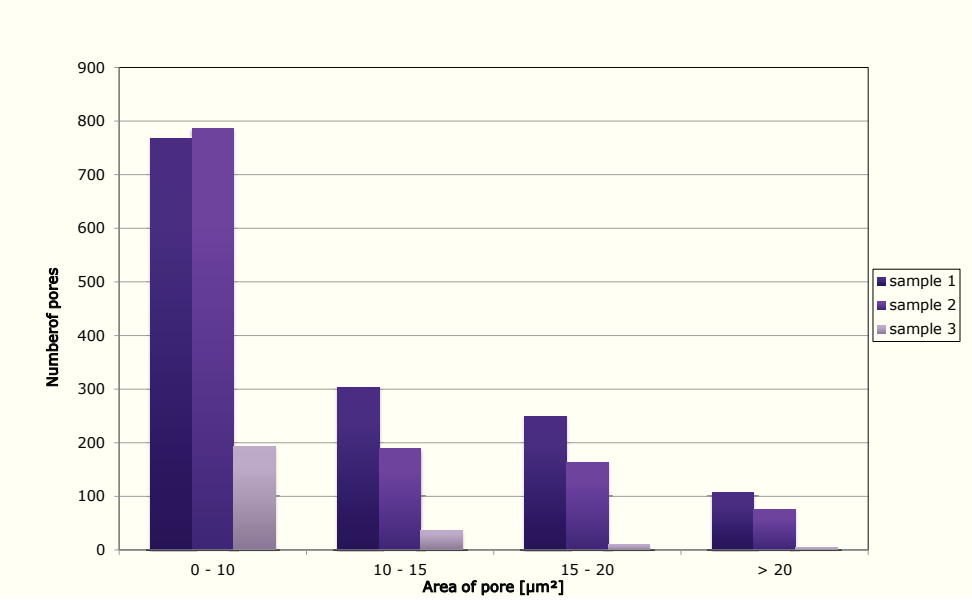

Figure 5.26: Number of pores in samples X dry-bag moulded, sintered

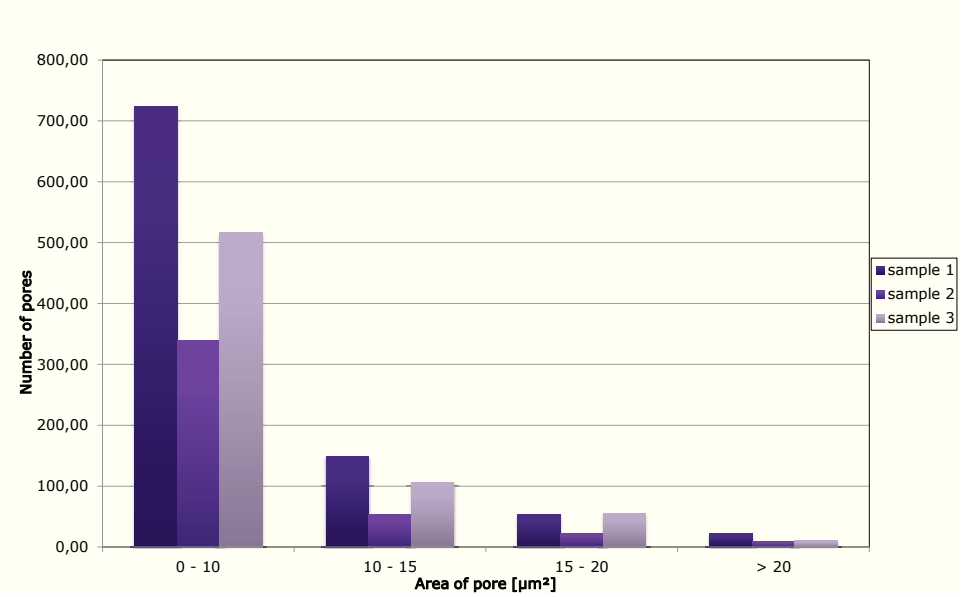

Figure 5.27: Number of pores in samples X dry-bag moulded sHIP

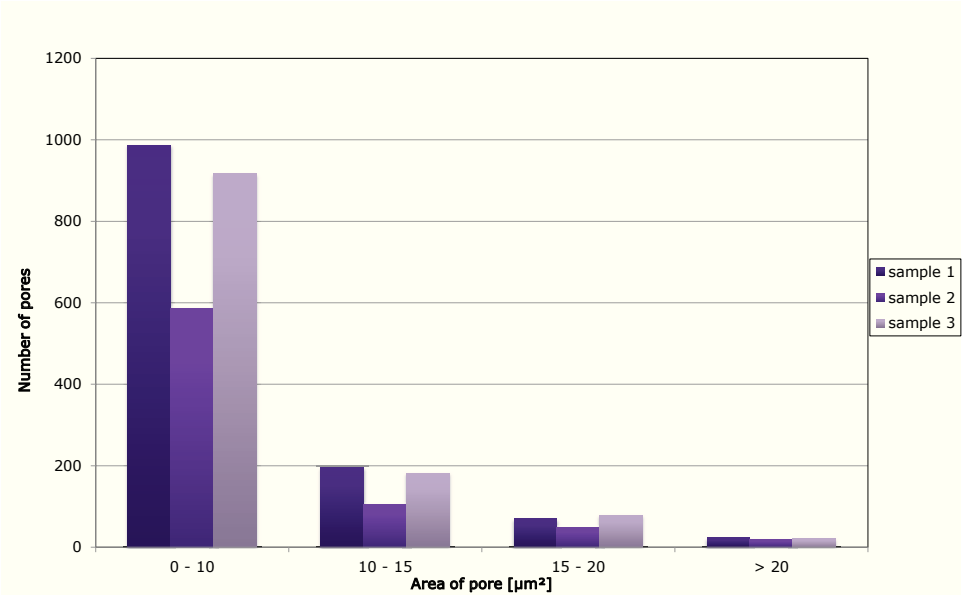

Figure 5.28: Number of pores in samples X dry-bag moulded HIP

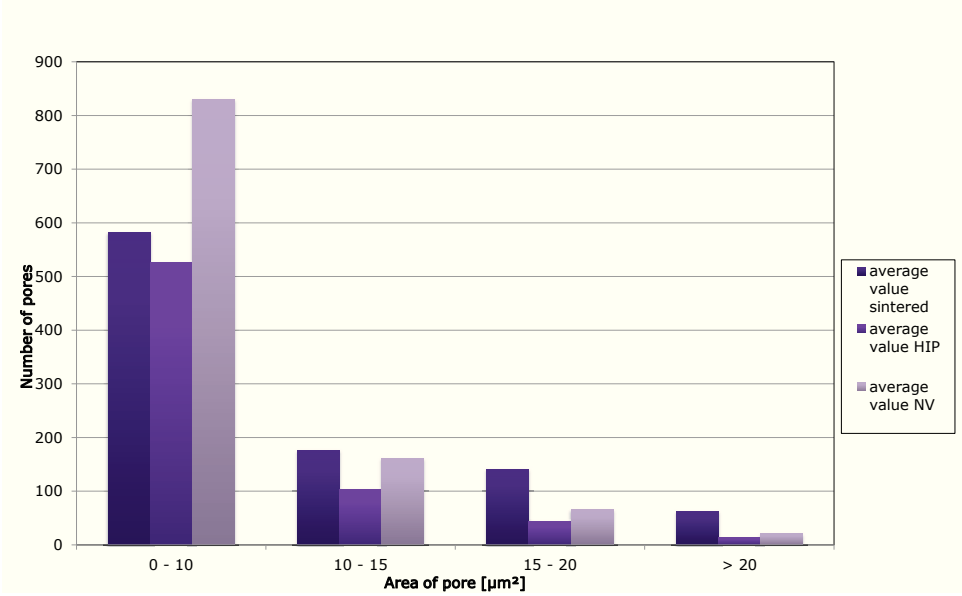

Figure 5.29: Number of pores in samples X dry-bag moulded dependent on the manufacturing method

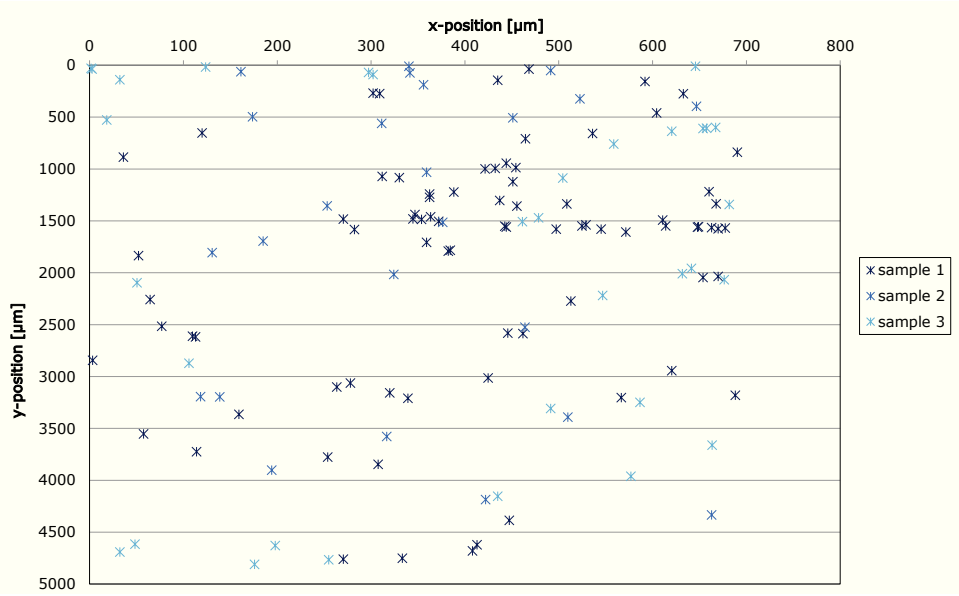

Figure 5.30: Positions of detected pores in Y dry-bag moulded, sintered

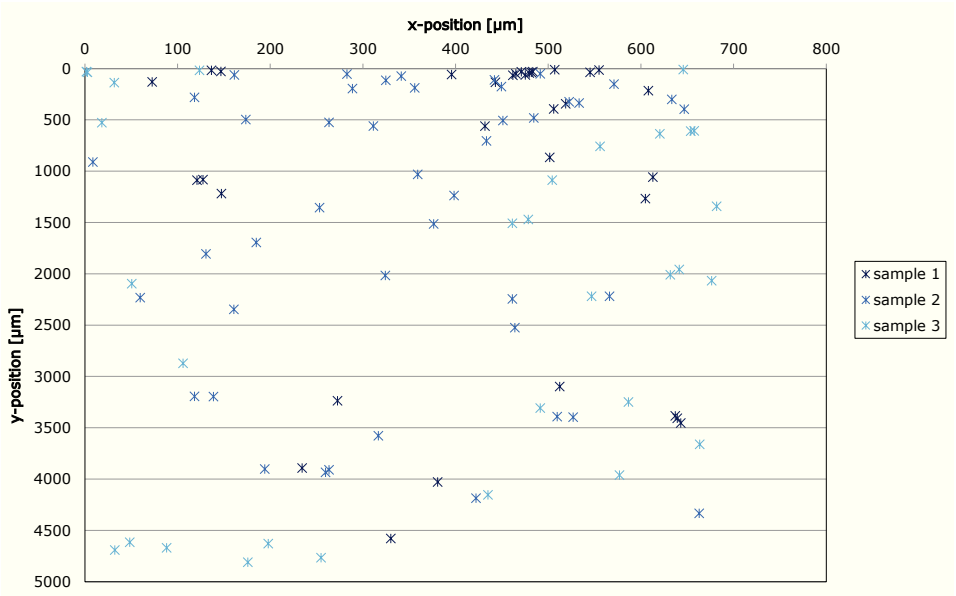

Figure 5.31: Positions of detected pores in Y dry-bag moulded sHIP

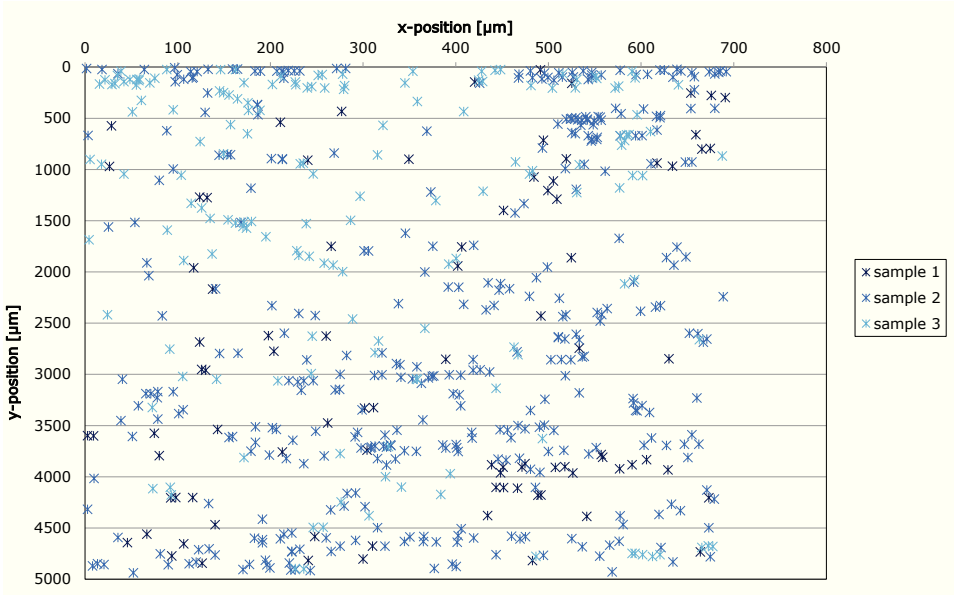

Figure 5.32: Positions of detected pores in Y dry-bag moulded HIP

Figures 5.33, 5.34 and 5.35 indicate the number of pores on the surface of Y dry-bag moulded samples. Figure 5.36 shows the average number of pores, occurring after each processing step, classified by pore area in Y dry-bag moulded samples.

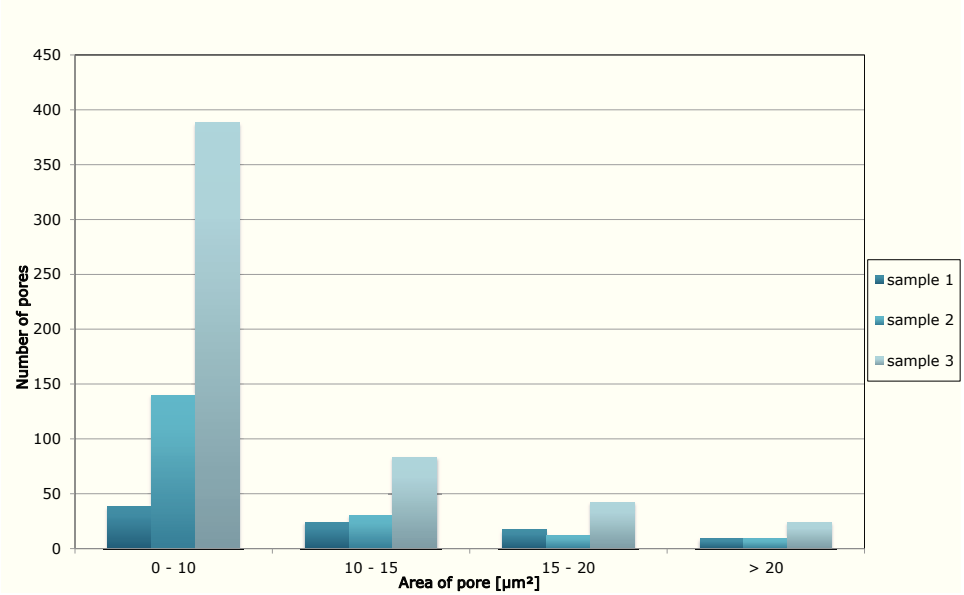

Figure 5.33: Number of pores in samples Y dry-bag moulded, sintered

Figures 5.37, 5.38 and 5.39 display the distribution of the pores on the surface of X direct moulded samples.
Figures 5.40, 5.41 and 5.42 display the number of pores on the surface of X direct moulded samples. Figure 5.43 displays the average number of pores, occurring after each processing step, classified by pore area in X direct moulded samples.
Figures 5.44, 5.45 and 5.46 display the distribution of the pores on the surface of Y direct moulded samples.

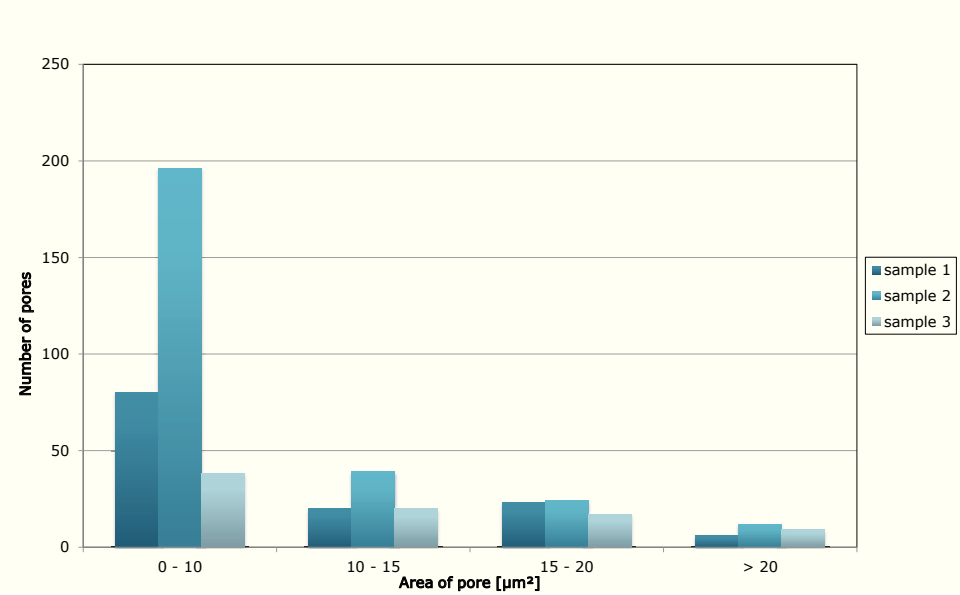

Figure 5.34: Number of pores in samples Y dry-bag moulded sHIP

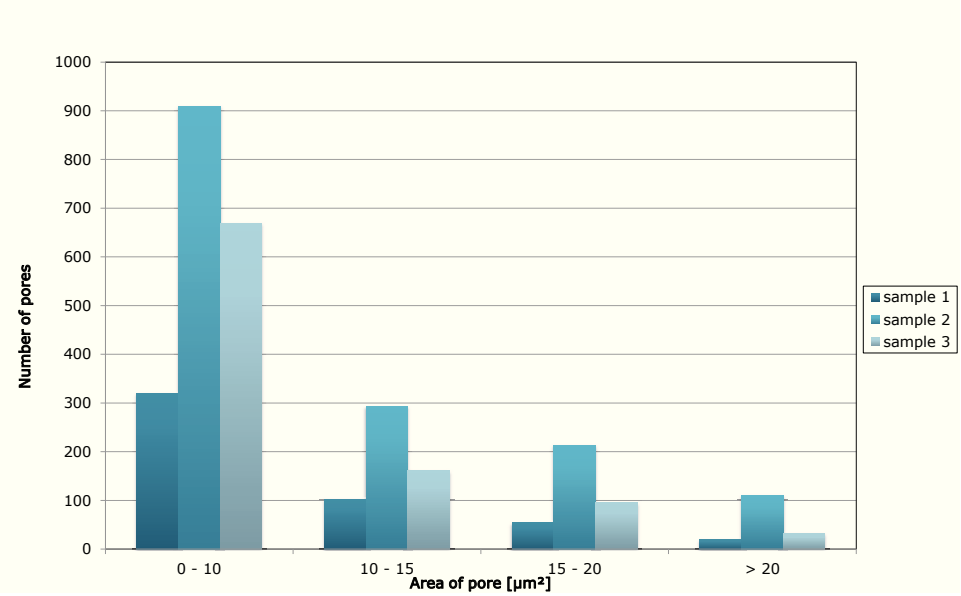

Figure 5.35: Number of pores in samples Y dry-bag moulded HIP

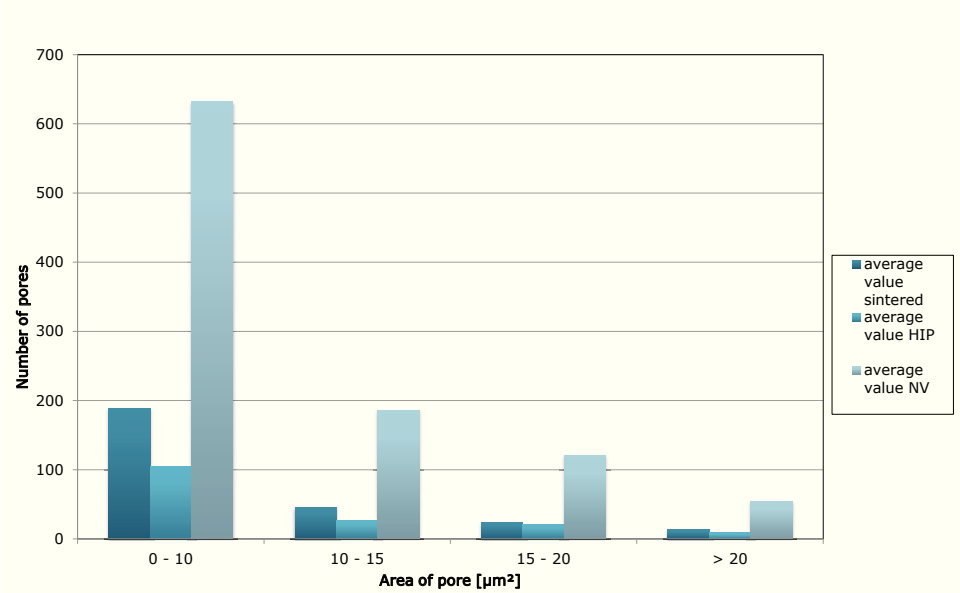

Figure 5.36: Number of pores in samples Y dry-bag moulded dependent on the manufacturing method

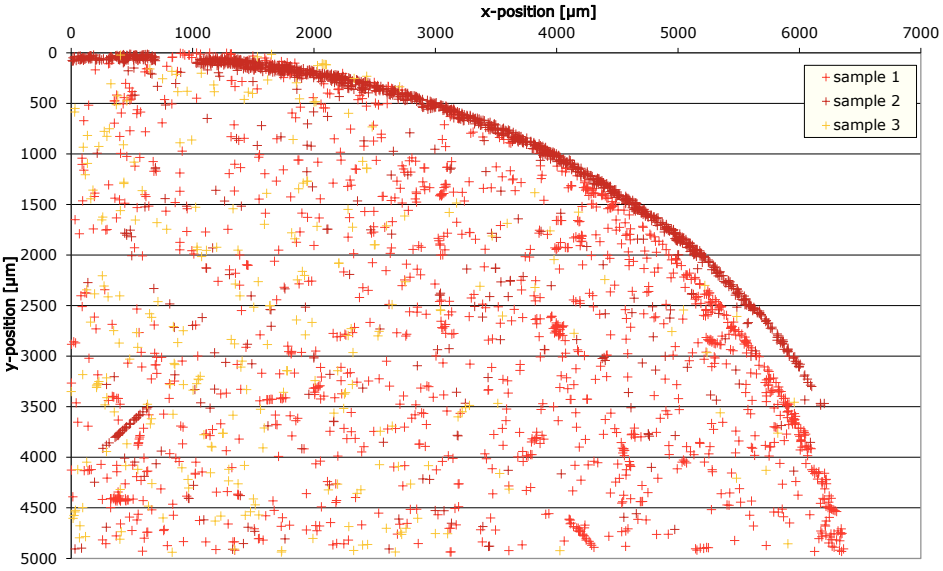

Figure 5.37: Positions of detected pores in X direct moulded, sintered

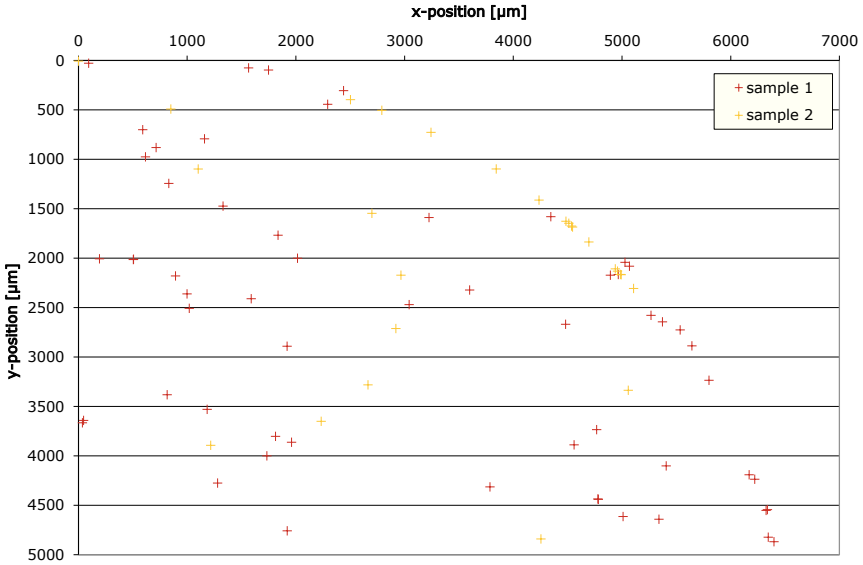

Figure 5.38: Positions of detected pores in X direct moulded sHIP

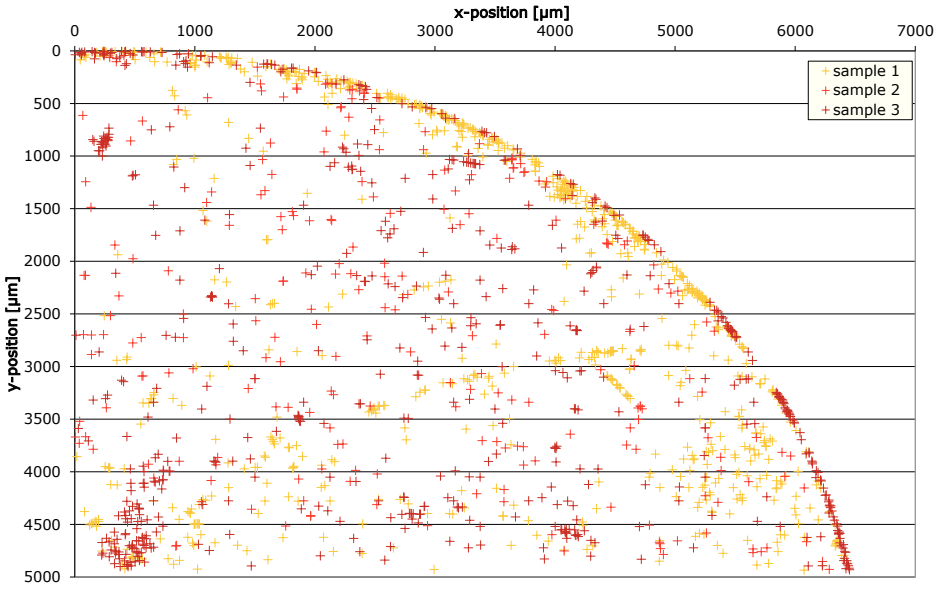

Figure 5.39: Positions of detected pores in X direct moulded HIP

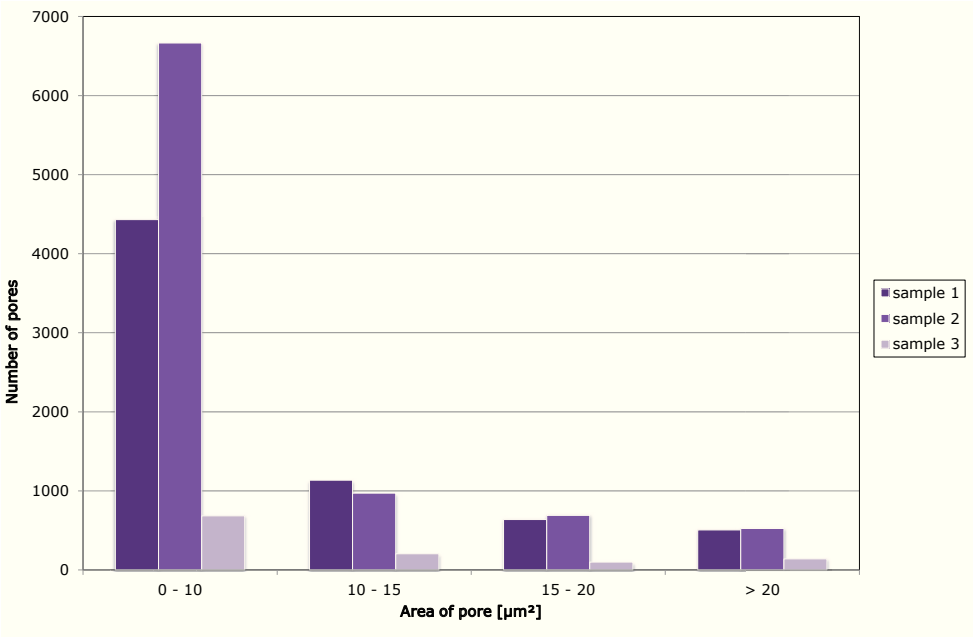

Figure 5.40: Number of pores in samples X direct moulded, sintered

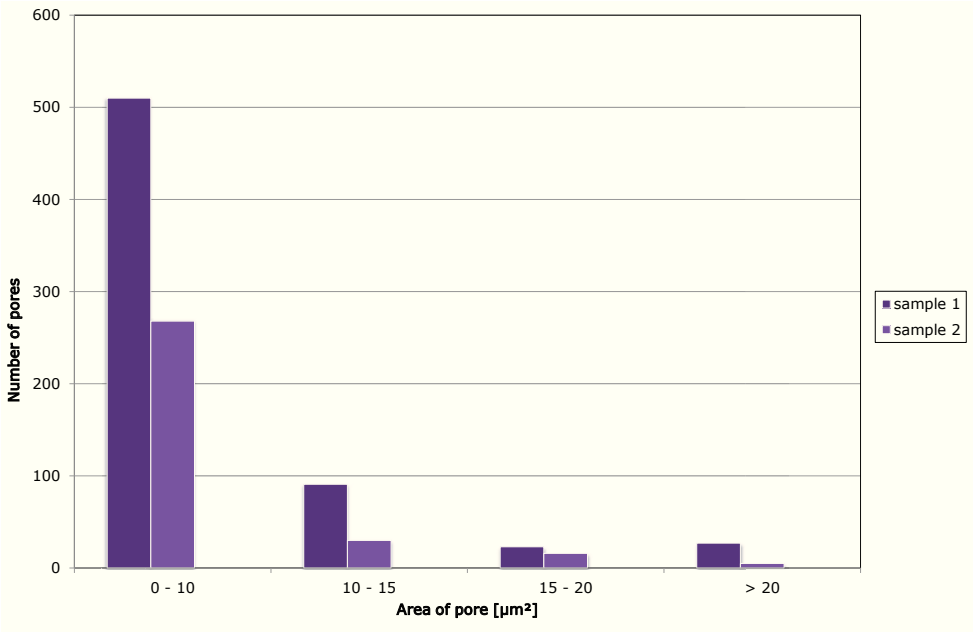

Figure 5.41: Number of pores in samples X direct moulded sHIP

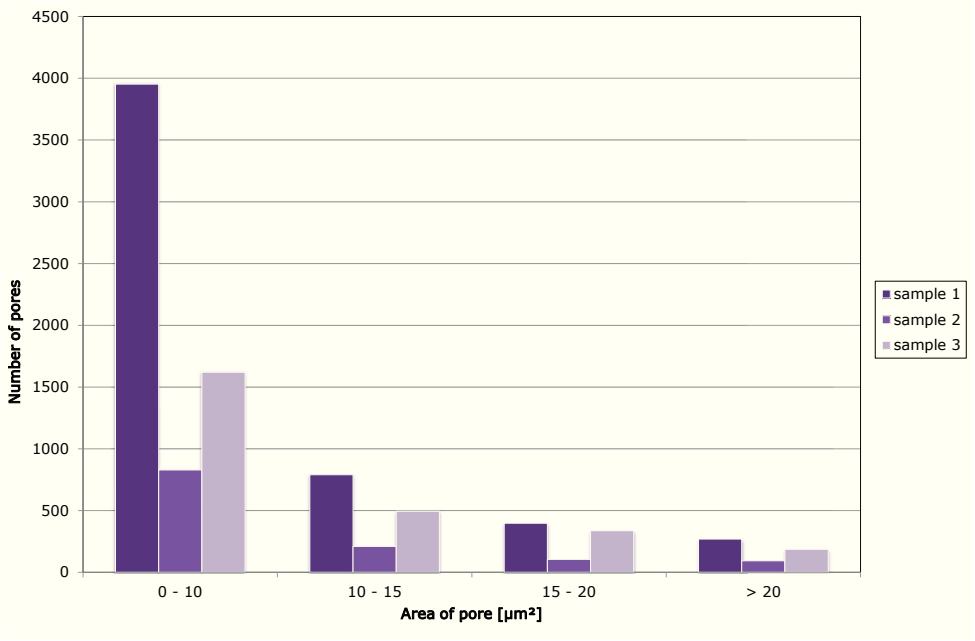

Figure 5.42: Number of pores in samples X direct moulded HIP

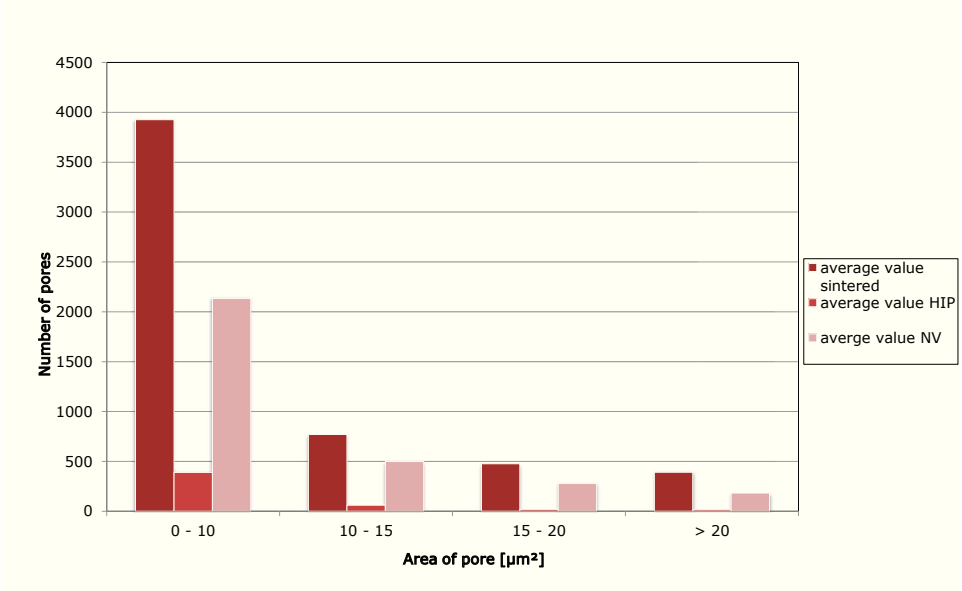

Figure 5.43: Number of pores in samples X direct moulded dependent on the manufacturing method

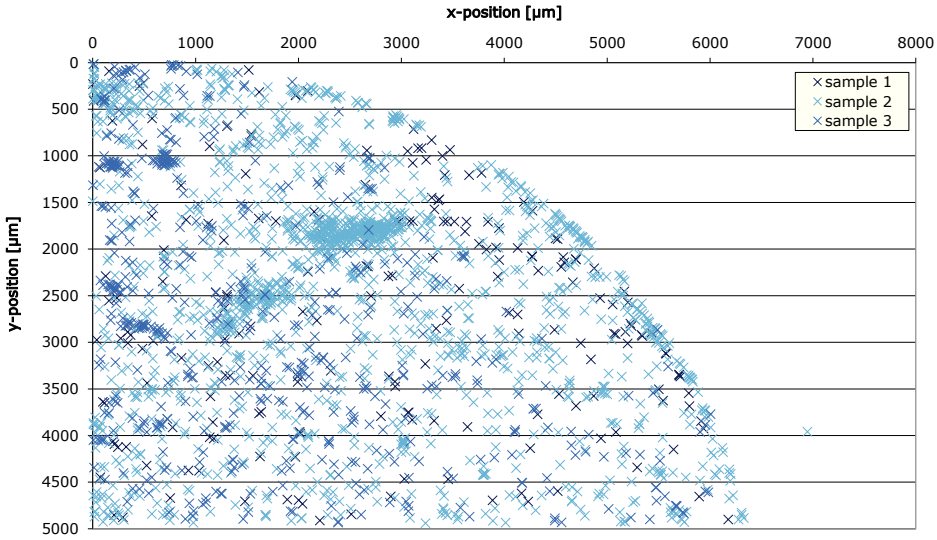

Figure 5.44: Positions of detected pores in Y direct moulded, sintered

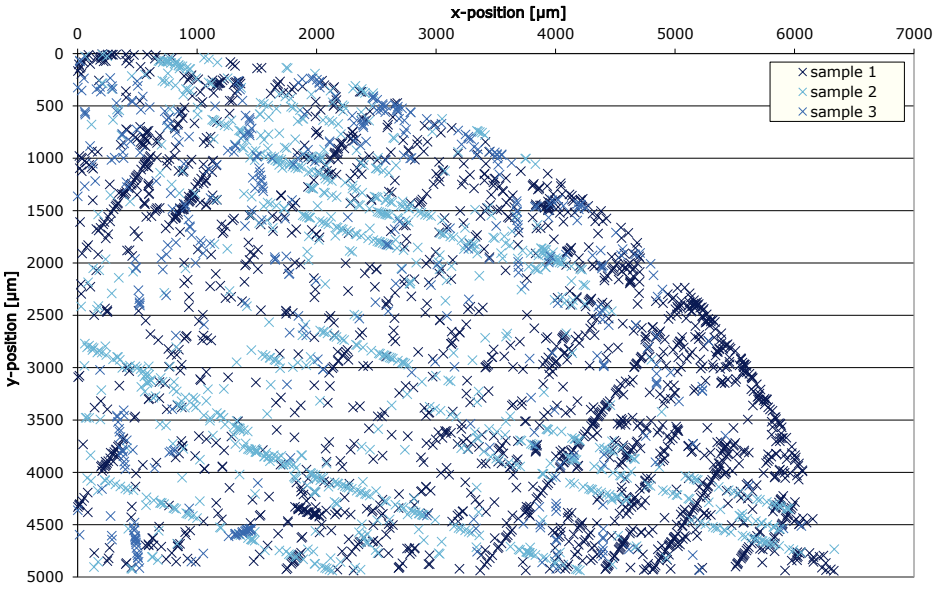

Figure 5.45: Positions of detected pores in Y direct moulded sHIP

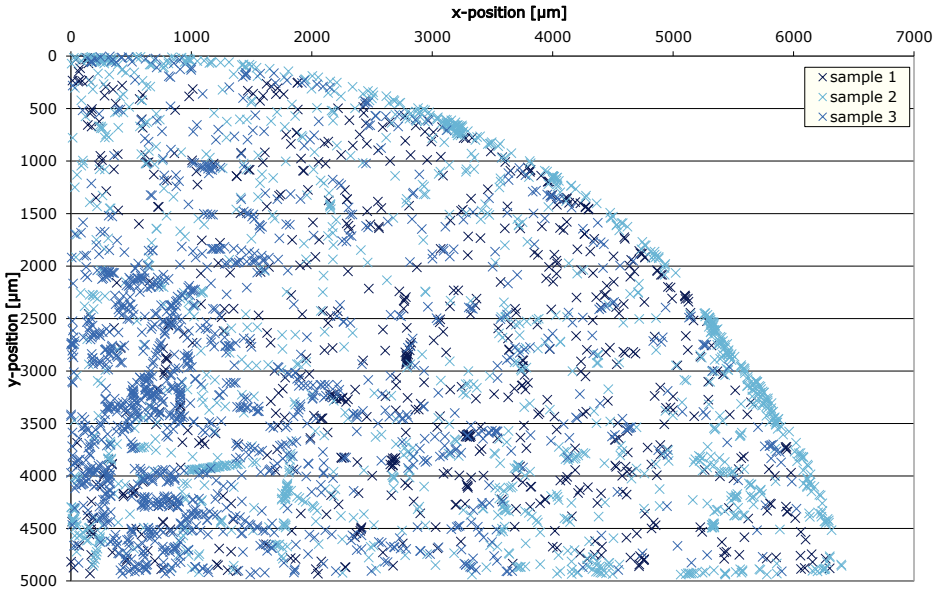

Figure 5.46: Positions of detected pores in Y direct moulded HIP

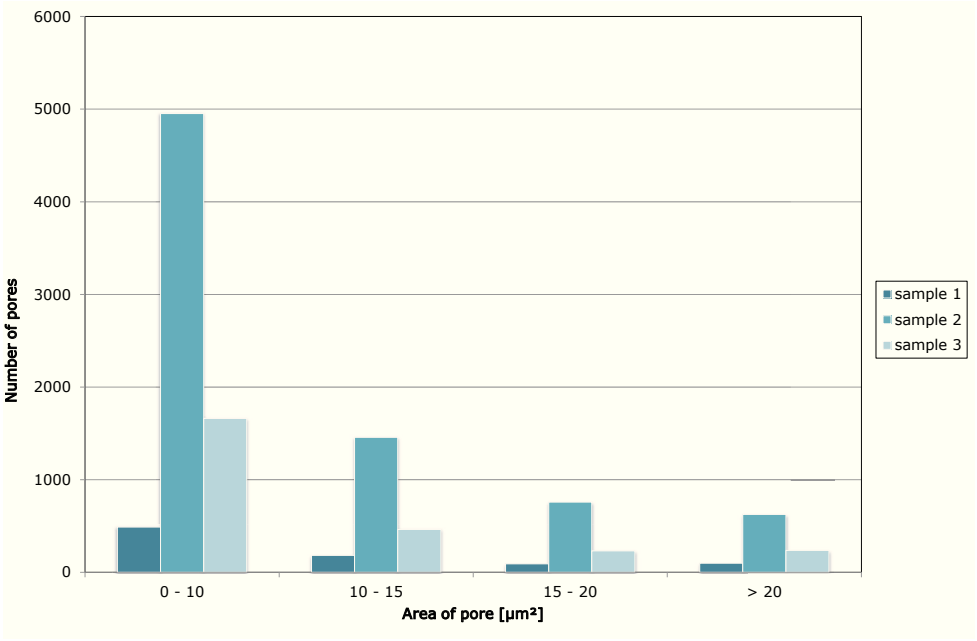

Figure 5.47: Number of pores in samples Y direct moulded, sintered

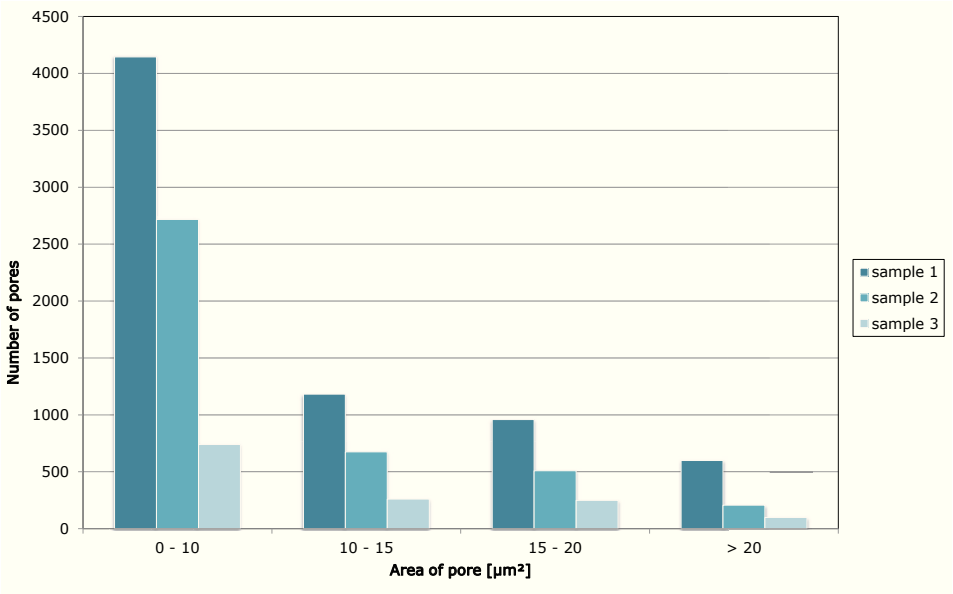

Figure 5.48: Number of pores in samples Y direct moulded sHIP

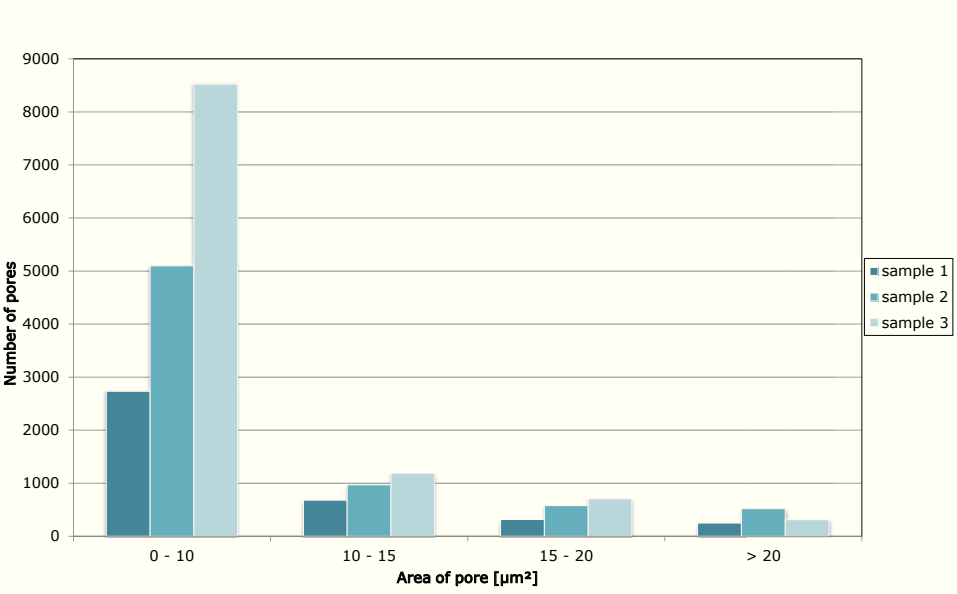

Figure 5.49: Number of pores in samples Y direct moulded HIP

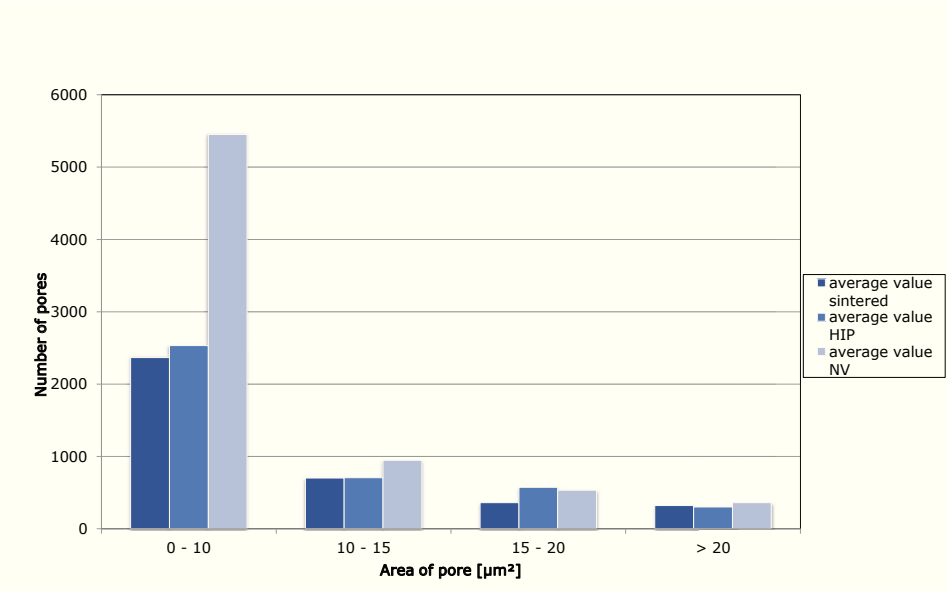

Figure 5.50: Number of pores in samples Y direct moulded dependent on the manufacturing method

SEM and SEM-EDX investigation

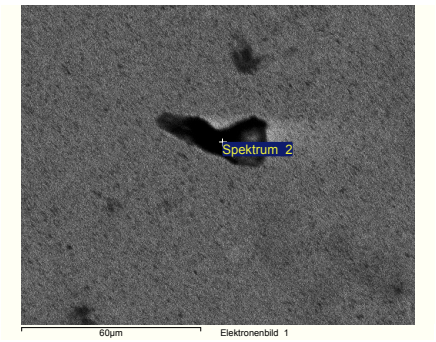

Spektrumverarbeitung :
Keine Peaks weggelassen

Verarbeitungsoption : Kohlenstoff nach Stöchiometrie (Norı
Anzahl Iterationen = 2

Standard :
O SiO2 1-Jun-1999 12:00 AM
Na Albite 1-Jun-1999 12:00 AM
Cl KCl 1-Jun-1999 12:00 AM
K MAD-10 Feldspar 1-Jun-1999 12:00 AM
W W 1-Jun-1999 12:00 AM

Ele...	Mas...	Atom%	Kom...	Formel
O K	16.44	45.98	0.00	
Na K	3.86	7.51	4.36	Na4C
Cl K	7.70	9.72	0.00	
K K	2.39	2.73	2.57	K4C
W M	64.70	15.75	68.93	WC
C	4.91	18.31		
Ins...	100.00			

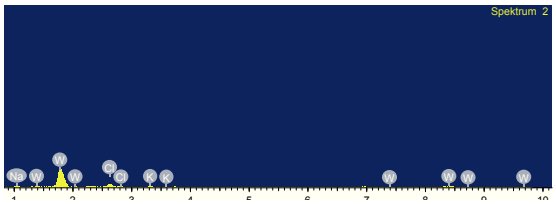

Figure 5.51: REM-EDX analysis of sample TSM 33 S SH 1

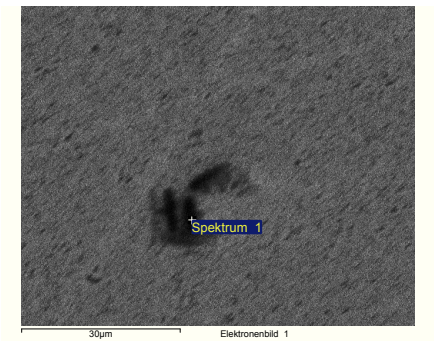

Spektrumverarbeitung :
Keine Peaks weggelassen

Verarbeitungsoption : Kohlenstoff nach Stöchiometrie (Norı
Anzahl Iterationen = 2

Standard :
O SiO2 1-Jun-1999 12:00 AM
Na Albite 1-Jun-1999 12:00 AM
Cl KCl 1-Jun-1999 12:00 AM
K MAD-10 Feldspar 1-Jun-1999 12:00 AM
Co Co 1-Jun-1999 12:00 AM
W W 1-Jun-1999 12:00 AM

Ele...	Mas...	Atom%	Kom...	Formel
O K	10.59	29.59	0.00	
Na K	6.20	12.06	7.01	Na4C
Cl K	11.08	13.97	0.00	
K K	5.94	6.79	6.40	K4C
Co K	10.65	8.08	10.65	CoC
W M	50.95	12.39	54.27	WC
C	4.59	17.11		
Ins...	100.00			

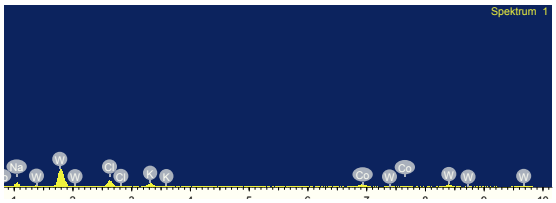

Figure 5.52: REM-EDX analysis of sample TSM 33 S SH 1

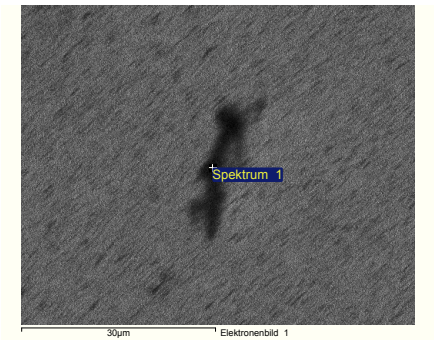

Spektrumverarbeitung :
Keine Peaks weggelassen

Verarbeitungsoption : Kohlenstoff nach Stöchiometrie (Norı
Anzahl Iterationen = 2

Standard :
O SiO2 1-Jun-1999 12:00 AM
Na Albite 1-Jun-1999 12:00 AM
Cl KCl 1-Jun-1999 12:00 AM
K MAD-10 Feldspar 1-Jun-1999 12:00 AM
Co Co 1-Jun-1999 12:00 AM
W W 1-Jun-1999 12:00 AM

Ele...	Mas...	Atom%	Kom...	Formel
O K	9.42	29.23	0.00	
Na K	5.89	12.72	6.66	Na4C
Cl K	8.85	12.39	0.00	
K K	1.69	2.14	1.82	K4C
Co K	8.01	6.74	8.01	CoC
W M	61.25	16.54	65.25	WC
C	4.90	20.25		
Ins...	100.00			

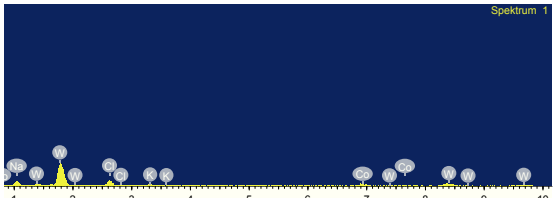

Figure 5.53: REM-EDX analysis of sample TSM 33 S NV 1

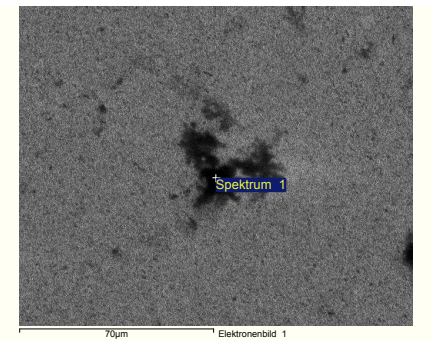

Spektrumverarbeitung :
Keine Peaks weggelassen

Verarbeitungsoption : Kohlenstoff nach Stöchiometrie (Norı
Anzahl Iterationen = 3

Standard :
O SiO2 1-Jun-1999 12:00 AM
Na Albite 1-Jun-1999 12:00 AM
Cl KCl 1-Jun-1999 12:00 AM
K MAD-10 Feldspar 1-Jun-1999 12:00 AM
Co Co 1-Jun-1999 12:00 AM
W W 1-Jun-1999 12:00 AM

Ele...	Mas...	Atom%	Kom...	Formel
O K	11.89	26.48	0.00	
Na K	12.24	18.96	13.83	Na4C
Cl K	23.42	23.53	0.00	
K K	9.22	8.40	9.93	K4C
Co K	3.71	2.24	3.71	CoC
W M	34.93	6.77	37.21	WC
C	4.59	13.61		
Ins...	100.00			

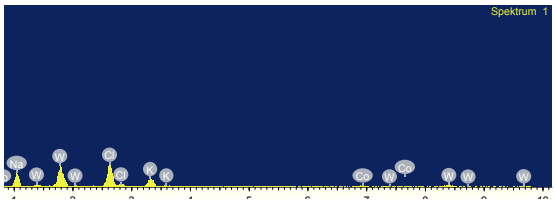

Figure 5.54: REM-EDX analysis of sample TSM 33 S NV 1

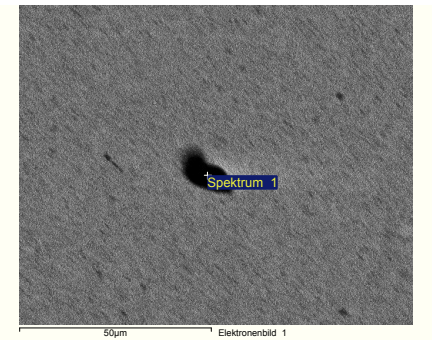

Spektrumverarbeitung :
Keine Peaks weggelassen

Verarbeitungsoption : Kohlenstoff nach Stöchiometrie (Norı
Anzahl Iterationen = 4

Standard :
O SiO2 1-Jun-1999 12:00 AM
Al Al2O3 1-Jun-1999 12:00 AM
W W 1-Jun-1999 12:00 AM

Ele...	Mas...	Atom%	Kom...	Formel
O K	53.64	61.16	0.00	
Al K	32.31	21.85	43.10	Al4C3
W M	3.06	0.30	3.26	WC
C	10.99	16.69		
Ins...	100.00			

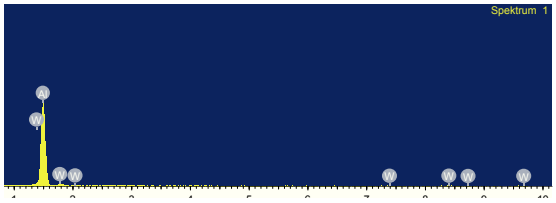

Figure 5.55: REM-EDX analysis of sample TSM 33 S NV 1

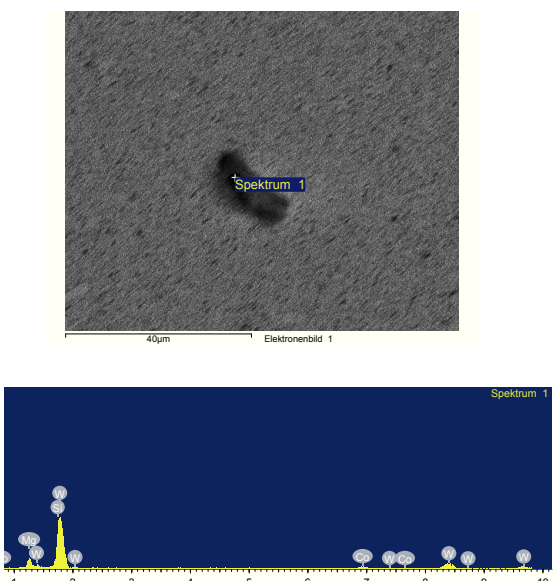

Spektrumverarbeitung :
Keine Peaks weggelassen

Verarbeitungsoption : Kohlenstoff nach Stöchiometrie (Norı
Anzahl Iterationen = 2

Standard :
O SiO2 1-Jun-1999 12:00 AM
Mg MgO 1-Jun-1999 12:00 AM
Si SiO2 1-Jun-1999 12:00 AM
Co Co 1-Jun-1999 12:00 AM
W W 1-Jun-1999 12:00 AM

Ele...	Mas...	Atom%	Kom...	Formel
O K	27.12	59.61	0.00	
Mg K	4.02	5.81	5.01	Mg2C
Si K	3.19	4.00	4.56	SiC
Co K	3.95	2.36	3.95	CoC
W M	55.72	10.66	59.36	WC
C	6.00	17.56		
Ins...	100.00			

Figure 5.56: REM-EDX analysis of sample TSM 33 S NV 1

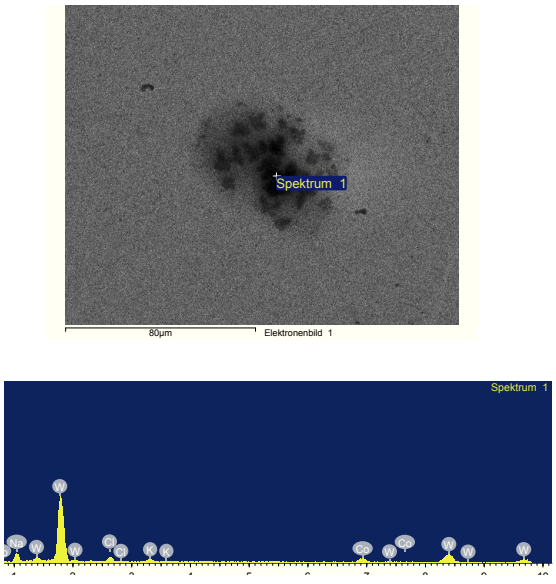

Spektrumverarbeitung :
Möglicherweise Peak weggelassen : 5.405 keV

Verarbeitungsoption : Kohlenstoff nach Stöchiometrie (Norı
Anzahl Iterationen = 3

Standard :
O SiO2 1-Jun-1999 12:00 AM
Na Albite 1-Jun-1999 12:00 AM
Cl KCl 1-Jun-1999 12:00 AM
K MAD-10 Feldspar 1-Jun-1999 12:00 AM
Co Co 1-Jun-1999 12:00 AM
W W 1-Jun-1999 12:00 AM

Ele...	Mas...	Atom%	Kom...	Formel
O K	18.11	49.34	0.00	
Na K	4.73	8.96	5.34	Na4C
Cl K	3.09	3.79	0.00	
K K	1.38	1.53	1.48	K4C
Co K	5.78	4.27	5.78	CoC
W M	62.14	14.73	66.20	WC
C	4.78	17.36		
Ins...	100.00			

Figure 5.57: REM-EDX analysis of sample TSF 22 S NV 2

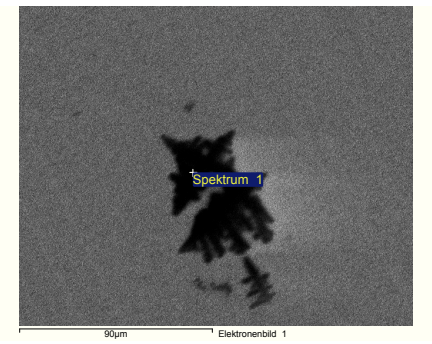

Spektrumverarbeitung :
Keine Peaks weggelassen

Verarbeitungsoption : Kohlenstoff nach Stöchiometrie (Norı
Anzahl Iterationen = 3

Standard :
O SiO2 1-Jun-1999 12:00 AM
Na Albite 1-Jun-1999 12:00 AM
Cl KCl 1-Jun-1999 12:00 AM
K MAD-10 Feldspar 1-Jun-1999 12:00 AM
Co Co 1-Jun-1999 12:00 AM
W W 1-Jun-1999 12:00 AM

Ele...	Mas...	Atom%	Kom...	Formel
O K	10.53	24.46	0.00	
Na K	12.56	20.30	14.20	Na4C
Cl K	21.69	22.73	0.00	
K K	8.13	7.72	8.75	K4C
Co K	3.14	1.98	3.14	CoC
W M	39.13	7.91	41.69	WC
C	4.82	14.91		
Ins...	100.00			

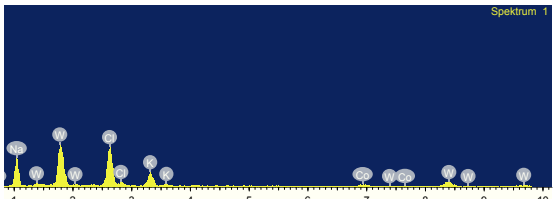

Figure 5.58: REM-EDX analysis of sample TSF 22 S NV 2

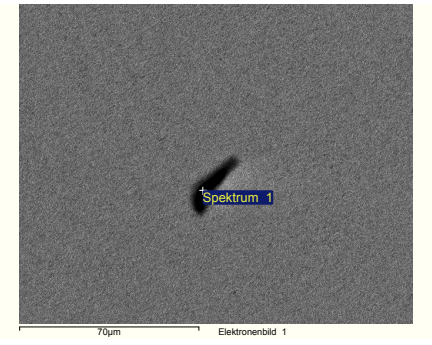

Spektrumverarbeitung :
Keine Peaks weggelassen

Verarbeitungsoption : Kohlenstoff nach Stöchiometrie (Norı
Anzahl Iterationen = 3

Standard :
O SiO2 1-Jun-1999 12:00 AM
Co Co 1-Jun-1999 12:00 AM
W W 1-Jun-1999 12:00 AM

Ele...	Mas...	Atom%	Kom...	Formel
O K	17.49	54.56	0.00	
Co K	10.07	8.53	10.07	CoC
W M	68.00	18.46	72.44	WC
C	4.44	18.46		
Ins...	100.00			

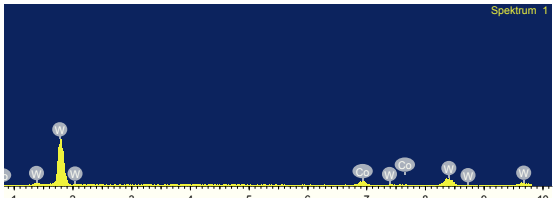

Figure 5.59: REM-EDX analysis of sample TSF 22 S NV 3

BET analysis

Quantachrome NovaWin - Data Acquisition and Reduction
for NOVA instruments
©1994-2010, Quantachrome Instruments
version 11.0

Quantachrome INSTRUMENTS
Optimizing particle performance

Analysis			**Report**		
Operator: Gerni	**Date:** 2012/05/04		**Operator:** Gerni	**Date:** 5/4/2012	
Sample ID: WC	**Filename:**		C:\QCdata\Physisorb\2012_05_03_B_01.qps		
Sample Desc:	Plansee_2_ohne_Kugel	**Comment:**	Ausheizen ca. 3 h		
Sample weight:	1.1558 g	**Sample Volume:**	0 cc		
Outgas Time:	3.0 hrs	**OutgasTemp:**	150.0 C		
Analysis gas:	Nitrogen	**Bath Temp:**	77.3 K		
Press. Tolerance:	0.100/0.100 (ads/des)	**Equil time:**	120/120 sec (ads/des)	**Equil timeout:**	1000/1000 sec (ads/de
Analysis Time:	866.8 min	**End of run:**	2012/05/04 3:03:35	**Instrument:**	Nova Station B
Cell ID:	0			**F/W version:**	0.00

Data Reduction Parameters

	Po override: 760.00 mmHg				
t-Method	**Calc. method:** de Boer				
BJH/DH method	**Moving pt. avg.:** off	**Ignoring P-tags below 0.35 P/Po**			
Adsorbate	Nitrogen	**Temperature**	77.350K		
	Molec. Wt.: 28.013 g	**Cross Section:**	16.200 Å²	**Liquid Density:**	0.806 g/cc
	Contact Angle: 0.0 degrees	**Surf. Tension:**	8.850 erg/cm²		

Isotherm * Linear

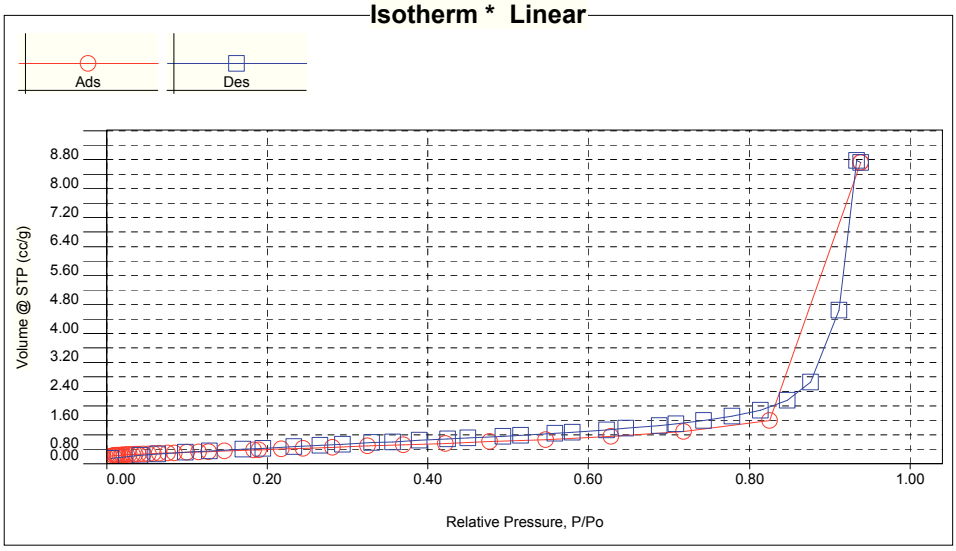

Figure 5.60: BET analysis TSM 33 S VS sample 1

Quantachrome NovaWin - Data Acquisition and Reduction
for NOVA instruments
©1994-2010, Quantachrome Instruments
version 11.0

Quantachrome INSTRUMENTS
Optimizing particle performance

Analysis
Operator: Gerni
Sample ID: WC
Date:2012/05/04
Filename:

Report
Operator: Gerni
Date:5/4/2012
C:\QCdata\Physisorb\2012_05_03_B_01.qps

MBET summary

Slope =	2296.157
Intercept =	4.905e+01
Correlation coefficient, r =	0.999619
C constant=	47.810
Surface Area =	1.485 m²/g

Multi-Point BET Plot

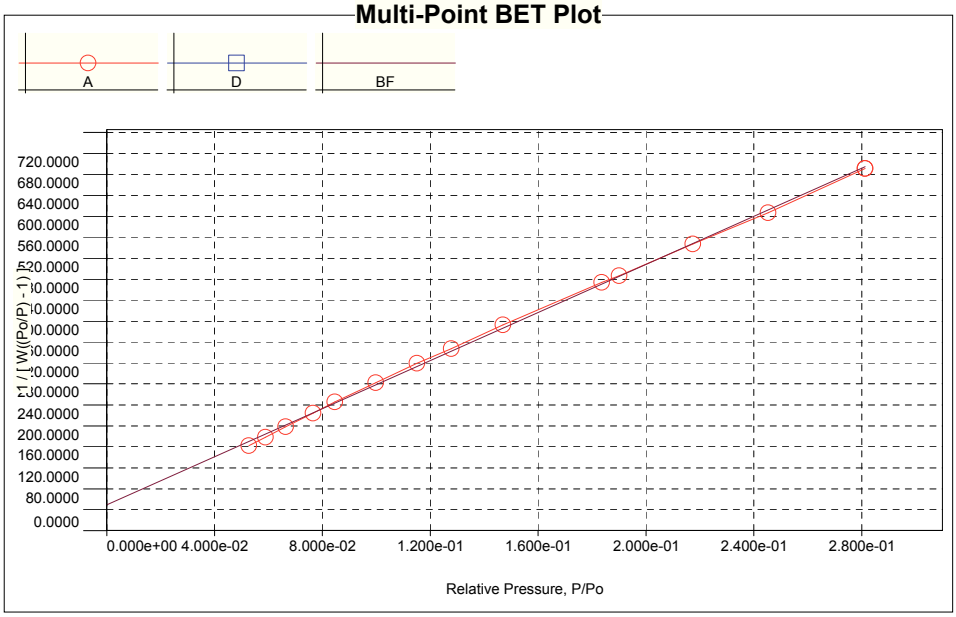

Multi-Point BET

Relative Pressure [P/Po]	Volume @ STP [cc/g]	1 / [W((Po/P) - 1)]	Relative Pressure [P/Po]	Volume @ STP [cc/g]	1 / [W((Po/P) - 1)]
5.28339e-02	0.2750	1.6227e+02	1.27852e-01	0.3370	3.4802e+02
5.89765e-02	0.2806	1.7870e+02	1.47081e-01	0.3513	3.9278e+02
6.64146e-02	0.2869	1.9840e+02	1.83638e-01	0.3798	4.7393e+02
7.66332e-02	0.2955	2.2469e+02	1.90068e-01	0.3859	4.8656e+02
8.48356e-02	0.3017	2.4581e+02	2.17429e-01	0.4059	5.4761e+02
1.00054e-01	0.3148	2.8258e+02	2.45254e-01	0.4282	6.0713e+02
1.15086e-01	0.3260	3.1923e+02	2.81404e-01	0.4535	6.9093e+02

Figure 5.61: BET analysis TSM 33 S VS sample 1

Quantachrome NovaWin - Data Acquisition and Reduction for NOVA instruments ©1994-2010, Quantachrome Instruments version 11.0

Quantachrome INSTRUMENTS Optimizing particle performance

Analysis
Operator: Gerni **Date:**2012/05/04
Sample ID: WC **Filename:**

Report
Operator: Gerni **Date:**5/4/2012
C:\QCdata\Physisorb\2012_05_03_B_01.qps

BJH desorption summary

Surface Area =	2.481 m²/g
Pore Volume =	0.013 cc/g
Pore Diameter Dv(d) =	27.078 nm

BJH method Desorption dV()

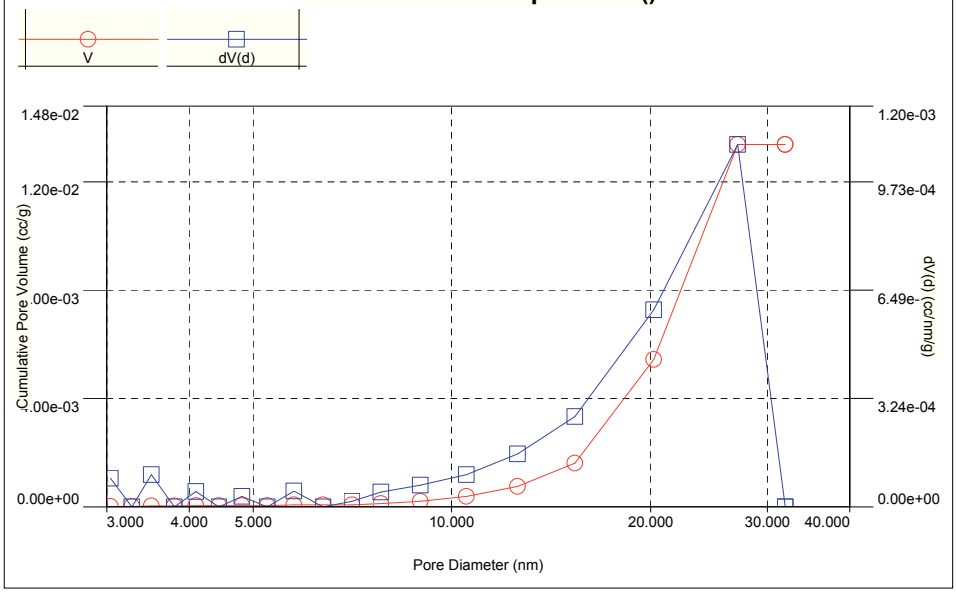

BJH Pore Size Distribution Desorption

Diameter [nm]	Pore Volume [cc/g]	Pore Surf Area [m²/g]	dV(d) [cc/nm/g]	dS(d) [m²/nm/g]	dV(logd) [cc/g]	dS(logd) [cc/g]
3.0421	1.9192e-05	2.5236e-02	8.5756e-05	1.1276e-01	6.0042e-04	7.8949e-01
3.2830	1.9192e-05	2.5236e-02	0.0000e+00	0.0000e+00	0.0000e+00	0.0000e+00
3.5104	3.8231e-05	4.6929e-02	9.6656e-05	1.1014e-01	7.8108e-04	8.9001e-01
3.7984	3.8231e-05	4.6929e-02	0.0000e+00	0.0000e+00	0.0000e+00	0.0000e+00
4.0942	4.7945e-05	5.6420e-02	4.5683e-05	4.4633e-02	4.3057e-04	4.2067e-01
4.4372	4.7945e-05	5.6420e-02	0.0000e+00	0.0000e+00	0.0000e+00	0.0000e+00
4.8081	5.6459e-05	6.3503e-02	3.1710e-05	2.6380e-02	3.5097e-04	2.9198e-01
5.2531	5.6459e-05	6.3503e-02	0.0000e+00	0.0000e+00	0.0000e+00	0.0000e+00
5.7640	7.5458e-05	7.6688e-02	4.7482e-05	3.2951e-02	6.2992e-04	4.3715e-01
6.3804	7.5458e-05	7.6688e-02	0.0000e+00	0.0000e+00	0.0000e+00	0.0000e+00
7.0569	8.4461e-05	8.1791e-02	1.7302e-05	9.8072e-03	2.8102e-04	1.5929e-01
7.8120	1.2903e-04	1.0461e-01	4.5020e-05	2.3052e-02	8.0873e-04	4.1410e-01
8.9689	2.1492e-04	1.4292e-01	6.4886e-05	2.8938e-02	1.3376e-03	5.9654e-01
10.5178	3.8525e-04	2.0770e-01	9.6010e-05	3.6513e-02	2.3197e-03	8.8218e-01
12.5928	7.6317e-04	3.2774e-01	1.5906e-04	5.0526e-02	4.5985e-03	1.4607e+00
15.3622	1.6209e-03	5.5106e-01	2.7118e-04	7.0609e-02	9.5583e-03	2.4888e+00
20.1810	5.4416e-03	1.3084e+00	5.9009e-04	1.1696e-01	2.7184e-02	5.3880e+00

Continued on next page

Figure 5.62: BET analysis TSM 33 S VS sample 1

Quantachrome NovaWin - Data Acquisition and Reduction
for NOVA instruments
©1994-2010, Quantachrome Instruments
version 11.0

Quantachrome INSTRUMENTS
Optimizing particle performance

Analysis
Operator: Gerni **Date:**2012/05/04
Sample ID: WC **Filename:**

Report
Operator: Gerni **Date:**5/4/2012
C:\QCdata\Physisorb\2012_05_03_B_01.qps

BJH Pore Size Distribution Desorption continued

Diameter [nm]	Pore Volume [cc/g]	Pore Surf Area [m²/g]	dV(d) [cc/nm/g]	dS(d) [m²/nm/g]	dV(logd) [cc/g]	dS(logd) [cc/g]
27.0778	1.3378e-02	2.4807e+00	1.0844e-03	1.6019e-01	6.7197e-02	9.9265e+00
31.9974	1.3378e-02	2.4807e+00	0.0000e+00	0.0000e+00	0.0000e+00	0.0000e+00

Figure 5.63: BET analysis TSM 33 S VS sample 1

Quantachrome NovaWin - Data Acquisition and Reduction
for NOVA instruments
©1994-2010, Quantachrome Instruments
version 11.0

Quantachrome INSTRUMENTS
Optimizing particle performance

Analysis				Report			
Operator:	Gerni	**Date:**	2012/05/04	**Operator:**	Gerni	**Date:**	5/4/2012
Sample ID:	WC	**Filename:**		C:\QCdata\Physisorb\2012_05_03_A_01.qps			
Sample Desc:	Plansee_1_mit_Kugel	**Comment:**		Ausheizen ca. 3 h			
Sample weight:	3.0007 g	**Sample Volume:**		0 cc			
Outgas Time:	3.0 hrs	**OutgasTemp:**		150.0 C			
Analysis gas:	Nitrogen	**Bath Temp:**		77.3 K			
Press. Tolerance:	0.100/0.100 (ads/des)	**Equil time:**		120/120 sec (ads/des)	**Equil timeout:**		1000/1000 sec (ads/de
Analysis Time:	863.5 min	**End of run:**		2012/05/04 3:00:16	**Instrument:**		Nova Station A
Cell ID:	0				**F/W version:**		0.00

Data Reduction Parameters

	Po override: 760.00 mmHg				
t-Method	**Calc. method:** de Boer				
BJH/DH method	**Moving pt. avg.:** off	**Ignoring P-tags below 0.35 P/Po**			
Adsorbate	**Nitrogen**	**Temperature**	77.350k		
	Molec. Wt.: 28.013 g	**Cross Section:**	16.200 Å²	**Liquid Density:**	0.806 g/cc
	Contact Angle: 0.0 degrees	**Surf. Tension:**	8.850 erg/cm²		

Isotherm * Linear

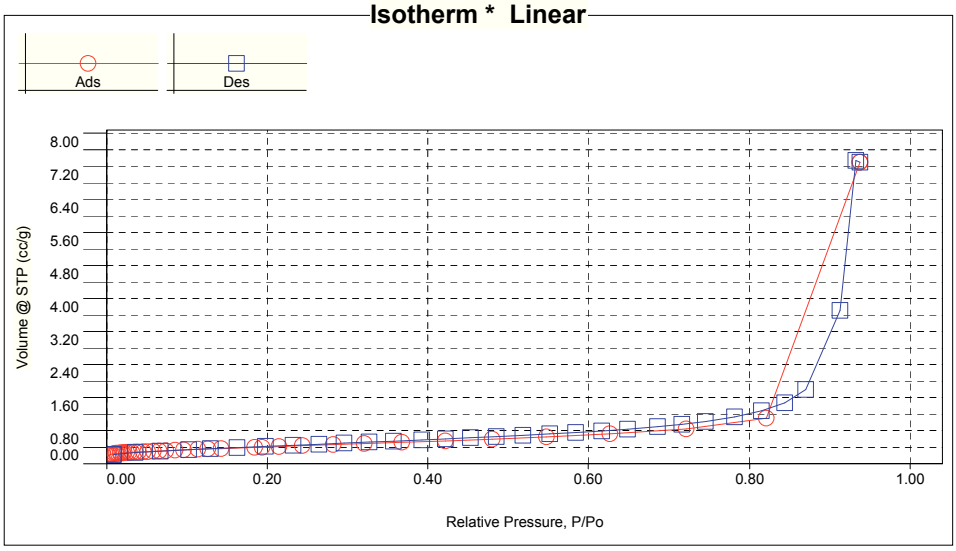

Figure 5.64: BET analysis TSM 33 S VS sample 2

Quantachrome NovaWin - Data Acquisition and Reduction
for NOVA instruments
©1994-2010, Quantachrome Instruments
version 11.0

Quantachrome INSTRUMENTS
Optimizing particle performance

Analysis
Operator: Gerni **Date:**2012/05/04
Sample ID: WC **Filename:**

Report
Operator: Gerni **Date:**5/4/2012
C:\QCdata\Physisorb\2012_05_03_A_01.qps

MBET summary

Slope =	2300.762
Intercept =	3.059e+01
Correlation coefficient, r =	0.999935
C constant=	76.211
Surface Area =	1.494 m²/g

Multi-Point BET Plot

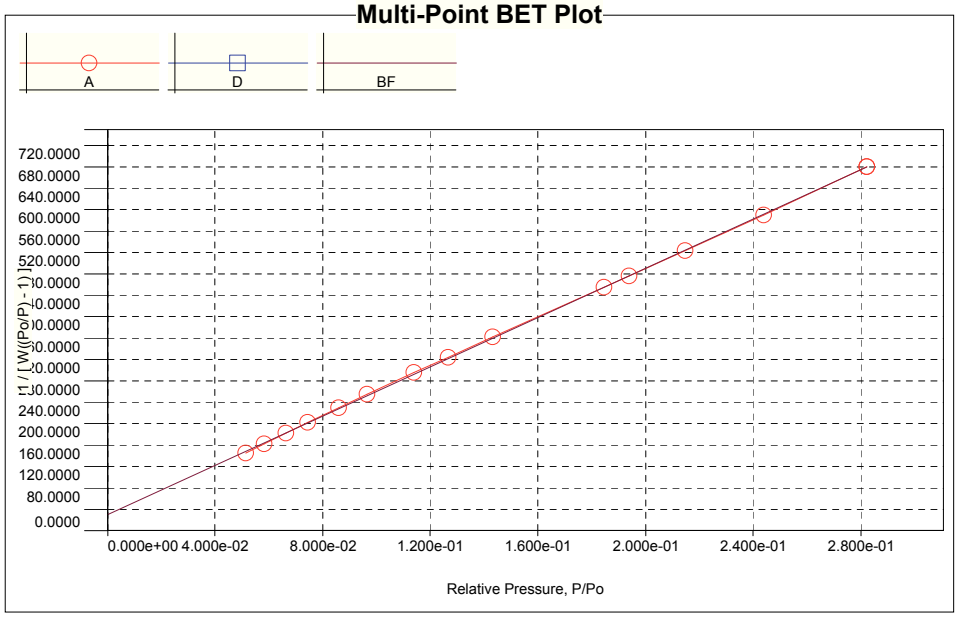

Multi-Point BET

Relative Pressure [P/Po]	Volume @ STP [cc/g]	1 / [W((Po/P) - 1)]	Relative Pressure [P/Po]	Volume @ STP [cc/g]	1 / [W((Po/P) - 1)]
5.14825e-02	0.2989	1.4530e+02	1.26593e-01	0.3578	3.2413e+02
5.82548e-02	0.3050	1.6230e+02	1.43098e-01	0.3693	3.6182e+02
6.64496e-02	0.3121	1.8250e+02	1.84518e-01	0.3978	4.5507e+02
7.46170e-02	0.3184	2.0265e+02	1.93758e-01	0.4038	4.7620e+02
8.58727e-02	0.3275	2.2950e+02	2.14818e-01	0.4184	5.2320e+02
9.65288e-02	0.3355	2.5481e+02	2.43831e-01	0.4376	5.8959e+02
1.13977e-01	0.3484	2.9541e+02	2.82219e-01	0.4626	6.8012e+02

Figure 5.65: BET analysis TSM 33 S VS sample 2

Quantachrome NovaWin - Data Acquisition and Reduction
for NOVA instruments
©1994-2010, Quantachrome Instruments
version 11.0

Quantachrome INSTRUMENTS
Optimizing particle performance

Analysis
Operator: Gerni
Sample ID: WC
Date:2012/05/04
Filename:

Report
Operator: Gerni
Date:5/4/2012
C:\QCdata\Physisorb\2012_05_03_A_01.qps

BJH desorption summary

Surface Area =	2.100 m²/g
Pore Volume =	0.012 cc/g
Pore Diameter Dv(d) =	27.052 nm

BJH method Desorption dV()

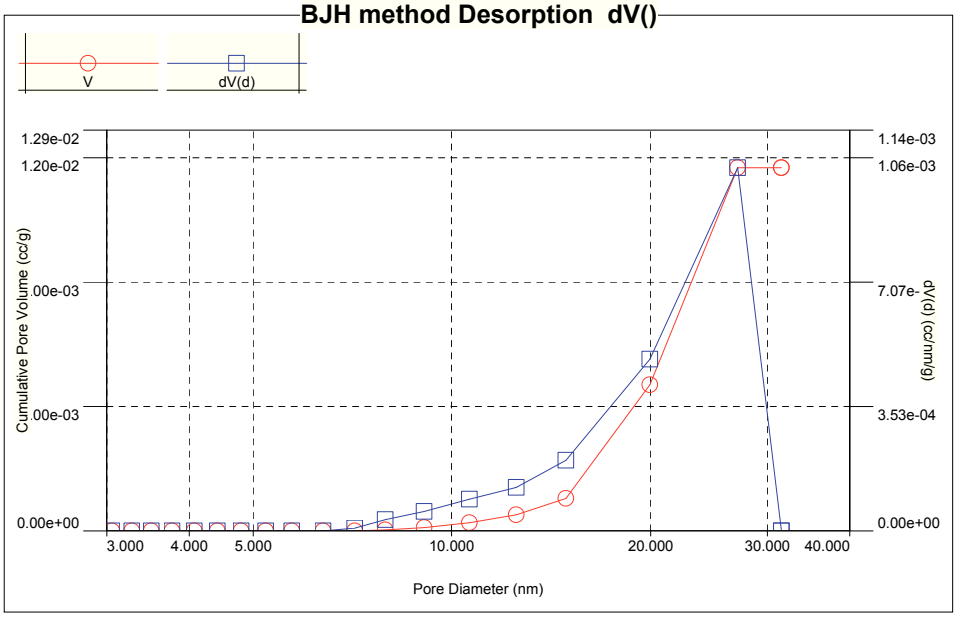

BJH Pore Size Distribution Desorption

Diameter [nm]	Pore Volume [cc/g]	Pore Surf Area [m²/g]	dV(d) [cc/nm/g]	dS(d) [m²/nm/g]	dV(logd) [cc/g]	dS(logd) [cc/g]
3.0564	0.0000e+00	0.0000e+00	0.0000e+00	0.0000e+00	0.0000e+00	0.0000e+00
3.2814	0.0000e+00	0.0000e+00	0.0000e+00	0.0000e+00	0.0000e+00	0.0000e+00
3.5098	0.0000e+00	0.0000e+00	0.0000e+00	0.0000e+00	0.0000e+00	0.0000e+00
3.7753	0.0000e+00	0.0000e+00	0.0000e+00	0.0000e+00	0.0000e+00	0.0000e+00
4.0745	0.0000e+00	0.0000e+00	0.0000e+00	0.0000e+00	0.0000e+00	0.0000e+00
4.4141	0.0000e+00	0.0000e+00	0.0000e+00	0.0000e+00	0.0000e+00	0.0000e+00
4.7967	0.0000e+00	0.0000e+00	0.0000e+00	0.0000e+00	0.0000e+00	0.0000e+00
5.2289	0.0000e+00	0.0000e+00	0.0000e+00	0.0000e+00	0.0000e+00	0.0000e+00
5.7293	0.0000e+00	0.0000e+00	0.0000e+00	0.0000e+00	0.0000e+00	0.0000e+00
6.3793	7.1801e-08	4.5021e-05	9.3994e-08	5.8937e-05	1.3790e-06	8.6468e-04
7.1309	6.2591e-06	3.5157e-03	8.3689e-06	4.6944e-03	1.3729e-04	7.7011e-02
7.9369	3.5062e-05	1.8032e-02	3.3007e-05	1.6635e-02	6.0260e-04	3.0370e-01
9.0689	1.1275e-04	5.2296e-02	5.5831e-05	2.4625e-02	1.1636e-03	5.1321e-01
10.6175	2.6777e-04	1.1070e-01	9.0884e-05	3.4239e-02	2.2171e-03	8.3527e-01
12.5111	5.2421e-04	1.9269e-01	1.2319e-04	3.9387e-02	3.5408e-03	1.1320e+00
14.8736	1.0549e-03	3.3541e-01	2.0076e-04	5.3990e-02	6.8574e-03	1.8442e+00
19.9345	4.7079e-03	1.0684e+00	4.8848e-04	9.8018e-02	2.2156e-02	4.4458e+00

Continued on next page

Figure 5.66: BET analysis TSM 33 S VS sample 2

Quantachrome NovaWin - Data Acquisition and Reduction
for NOVA instruments
©1994-2010, Quantachrome Instruments
version 11.0

Quantachrome INSTRUMENTS
Optimizing particle performance

Analysis
Operator: Gerni **Date:**2012/05/04
Sample ID: WC **Filename:**

Report
Operator: Gerni **Date:**5/4/2012
C:\QCdata\Physisorb\2012_05_03_A_01.qps

BJH Pore Size Distribution Desorption continued

Diameter [nm]	Pore Volume [cc/g]	Pore Surf Area [m²/g]	dV(d) [cc/nm/g]	dS(d) [m²/nm/g]	dV(logd) [cc/g]	dS(logd) [cc/g]
27.0518	1.1683e-02	2.0998e+00	1.0324e-03	1.5265e-01	6.3971e-02	9.4590e+00
31.5891	1.1683e-02	2.0998e+00	0.0000e+00	0.0000e+00	0.0000e+00	0.0000e+00

Figure 5.67: BET analysis TSM 33 S VS sample 2